

Long-range Interactions in the Calcium Dimer
Studied by Molecular Spectroscopy

Vom Fachbereich Physik der Universität Hannover
und von der Université Paris-Sud (U.F.R. Scientifique d'Orsay)

zur Erlangung des gemeinsamen Grades

Doktor der Naturwissenschaften Dr. rer. nat. (deutscher Titel)
Docteur en science (titre français)

genehmigte Dissertation
von

Olivier Allard

geboren am 23.10.1972 in Clichy-la-Garenne (Frankreich)

2004



Long-range Interactions in the Calcium Dimer
Studied by Molecular Spectroscopy

Vom Fachbereich Physik der Universität Hannover
und von der Université Paris-Sud (U.F.R. Scientifique d'Orsay)

zur Erlangung des gemeinsamen Grades

Doktor der Naturwissenschaften Dr. rer. nat. (deutscher Titel)
Docteur en science (titre français)

genehmigte Dissertation
von

Olivier Allard

geboren am 23.10.1972 in Clichy-la-Garenne (Frankreich)

2004

Referent: Prof. Dr. E. Tiemann
Korreferent: (DR) Dr. J.M. Hartmann
Tag des Promotion: 25 November 2004

Zusammenfassung Olivier Allard

Neueste Fortschritte im Zuge der Entwicklung eines optischen Frequenzstandards mit der Interkombinationslinie $(4p4s)^3P_1 (m_j=0) \leftarrow (4s4s)^1S_0$ des Calciums war Motivation zur systematischen Untersuchung der langreichweitigen Wechselwirkung zweier Calcium Atome. Die Potentialkurve eines Calciumdimers muss genau bekannt sein um, den Einfluss von Zweikörperstößen während des Abfragens mit Licht zu untersuchen. Wir haben die Form der Potentialkurve analysiert, die die Wechselwirkung zweier 1S Ca Atome beschreibt, indem wir die Position der Vibrations-Rotationsniveaus des $X^1\Sigma_g^+$ Grundzustand des Ca_2 gemessen haben.

Mittels hochauflösende Fourier transform Spektroskopie konnten wir mehr als 99.8 % des $X^1\Sigma_g^+$ Grundzustands bestimmen. Um die Position der am schwächsten gebundenen Niveaus des Grundzustands zu bestimmen, haben wir die Methode der Laseranregung mit gefilterter Fluoreszenz angewendet. Die Übergangsfrequenzen des Ca_2 B-X Systems von asymptotischen Niveaus des $X^1\Sigma_g^+$ Grundzustands bis $v'' = 38$ wurden gemessen. Das höchste vermessene Niveau ist nur 0.2 cm^{-1} unter der Molekülasymptote $^1S+^1S$ und hat einen klassischen äußeren Umkehrpunkt von etwa 20 \AA . Eine Potentialkurve, die Dispersionsterme für den langreichweitigen Teil enthält, wurde bestimmt. Ein wichtiger Punkt ist die Genauigkeit von Aussagen, die man von diesem Potential ableiten kann. Die Genauigkeit der abgeleiteten Dispersionskoeffizienten C_6, C_8, C_{10} sowie der Dissociationsenergie wurden durch eine Monte-Carlo-Simulation abgeschätzt. Ebenso wurde ein Intervall für die s-Wellen Streulänge bestimmt. Zur Beschreibung von Atomstößen während der Laserabfragung der Interkombinationslinie wird zudem eine genaue Beschreibung des $c^3\Pi_u$ Molekülzustands benötigt, der zu der $^3P + ^1S_0$ Asymptote korreliert. Dieser Zustand kann nicht über einen dipolerlaubten Übergang vom Grundzustand erreicht werden, ist aber an den $A^1\Sigma_u^+$ Zustand via Spinbahnwechselwirkung gekoppelt. Ein-Laser-Spektroskopie des A Zustands mit stossinduzierten Satelitten wurde durchgeführt. Störungen durch den $c^3\Pi_u$ Zustand wurden vermessen und mit einer Arbeit von Hofmann and Harris von 1986 verglichen. Eine Entstöranalyse der beobachteten Werte wurde mittels der Fourier-Grid-Hamiltonian-Methode begonnen. Unsere Experimente bereiten zudem auf dopplerfreie Spektroskopie der $c^3\Pi_u$ Asymptote in einem Molekülstrahl vor und ermöglichen schon jetzt das Erreichen des Triplettsystems des Calciumdimers.

Schlüsselworte: Ca_2 , Molekülspektroskopie, Potentialkurven, kalte Stöße, Monte-Carlo Simulation, Entstörung.

Abstract Olivier Allard

Recent progress in the development of a calcium optical frequency standard using the $(4p4s)^3P_1 (m_j=0) \leftarrow (4s4s)^1S_0$ intercombination line has motivated us to perform a systematic study of the long range interactions between two calcium atoms. To investigate the influence of the binary collision during the laser interrogation of the clock transition, a precise knowledge of the potential energy curves of the calcium dimer is necessary. We investigated the shape of the potential energy curve describing the interaction between two 1S Ca atoms by measuring the positions of rovibrational levels of the $X^1\Sigma_g^+$ ground state in the Ca_2 molecule.

A high resolution Fourier transform spectroscopy allowed us to accurately describe more than 99.8 % of the $X^1\Sigma_g^+$ state potential well. In order to collect information about the position of the last bound levels of the ground state we have applied laser excitations with filtered detection. Transition frequencies of the Ca_2 B-X system from asymptotic levels of the $X^1\Sigma_g^+$ ground state reaching $v'' = 38$ were measured. This highest observed level is only 0.2 cm^{-1} below the molecular $^1S+^1S$ asymptote and has an outer classical turning point of about 20 \AA . A potential energy curve which includes dispersion terms for the description of its long-range part has been achieved.

One important issue is the accuracy of the predictions one may draw using the derived potential. The precision of the determined dispersion coefficients C_6 , C_8 , C_{10} and the dissociation energy have been estimated by implementing a Monte Carlo simulation. A range for the s-wave scattering length has been derived as well.

The description of the atom-collisions involved during the laser interrogation of the intercombination transition necessitates also a precise knowledge on the $c^3\Pi_u$ molecular state correlated to the $^3P + ^1S_0$ asymptote. This state has no dipole allowed transition to the ground state but is coupled to the $A^1\Sigma_u^+$ by the spin-orbit interaction. A single laser spectroscopy of the A state extended by the observation of induced collision satellites has been realized and new perturbations due to the $c^3\Pi_u$ have been observed compared to the previous study by Hofmann and Harris in 1986. A deperturbation analysis on the observed data has been engaged using the Fourier grid Hamiltonian method. Potential energy curves of both states and the spin-orbit coupling have been derived. This study will allow an investigation of the $c^3\Pi_u$ asymptote by Doppler free spectroscopy in a molecular beam of Ca_2 and provides already access to the triplet manifold in calcium dimer.

Key words: Ca_2 , molecular spectroscopy, potential energy curves, cold collisions, Monte-Carlo simulation, deperturbation.

Résumé Olivier Allard

Les progrès récents dans le développement d'un standard de fréquence optique sur la transition $(4p4s)^3P_1 (m_j=0) \leftarrow (4s4s)^1S_0$ du calcium nous ont motivés à entreprendre une étude systématique des interactions à longue portée entre deux atomes de calcium. Afin de comprendre l'influence des collisions binaires pendant l'interrogation laser de la transition d'horloge, une connaissance précise des courbes d'énergie potentielle est nécessaire. Nous avons étudié la forme de la courbe décrivant l'interaction entre deux atomes dans l'état 1S par la mesure de la position en énergie des niveaux rovibrationnels de l'état fondamental $X^1\Sigma_g^+$ de la molécule de calcium Ca_2 . Par spectroscopie à transformée de Fourier nous avons caractérisé plus de 99.8% du puits de potentiel. Afin d'obtenir plus d'informations sur la position des derniers niveaux liés nous avons employé une technique d'excitation laser combinée avec une détection filtrée en fréquence. Plusieurs niveaux rotationnels des niveaux vibrationnels allant de $v'' = 34$ jusque $v'' = 38$ ont été observés. Le niveau observé se trouvant le plus proche de l'asymptote $^1S+^1S$ est lié seulement par 0.2 cm^{-1} et possède un point tournant classique proche de 20 \AA . De ces données spectroscopiques nous avons établi une courbe de potentiel qui inclut les termes des forces de dispersion pour la description de la partie à longue portée.

Une question importante concerne la précision des prédictions que l'on peut effectuer en utilisant le potentiel que l'on a déterminé. C'est pourquoi, en adaptant la méthode de Monte-Carlo nous avons déterminé la précision des coefficients de van der Waals C_6 , C_8 , C_{10} et de l'énergie de dissociation. Un intervalle pour la longueur de diffusion a été obtenu.

La description des collisions binaires entre atomes durant l'interrogation laser de la transition dipolaire interdite nécessite une connaissance précise de l'état moléculaire $c^3\Pi_u$ corrélé à l'asymptote $^3P + ^1S_0$. Cet état ne possède pas de transition dipolaire permise avec l'état fondamental, mais est couplé à l'état $A^1\Sigma_u^+$ par l'interaction spin-orbite. Une spectroscopie laser de l'état A étendue par l'observation de raies satellites induites par collisions a été réalisée et de nouvelles perturbations, comparés à l'étude d'Hofmann et Harris de 1986, ont été observées. Une analyse de déperturbation utilisant la méthode de l'Hamiltonien de grille de Fourier a été engagée. Des courbes de potentiel pour les deux états et le couplage spin-orbite ont été obtenus. Cette analyse permettra une étude précise de l'asymptote de l'état $c^3\Pi_u$ par une spectroscopie à haute résolution dans un jet moléculaire de Ca_2 , mais donne déjà accès aux états triplets du dimère de calcium.

mots-clefs: Ca_2 , spectroscopie moléculaire, courbe de potentiel, collisions froides, simulation Monte-Carlo, déperturbation.

Contents

	Zusammenfassung	3
	Abstract	4
	Résumé	5
1	Introduction	11
2	The calcium dimer ground state	17
2.1	What do we know about the ground state?	17
2.2	Laser induced fluorescence experiment	19
2.2.1	LIF Setup	19
	The heat pipe oven	20
2.2.2	Transitions	22
2.2.3	Observed spectra	24
2.2.4	Experimental uncertainty	29
	Doppler broadening	29
	Instrumental broadening	30
	Aperture	31
	Summery	31
	Signal-to-Noise ratio	32
2.3	Determination of the interaction potential	32
2.3.1	Construction of the potential energy curve	33
	The analytical representation	35
	Numerical IPA potential	37
2.4	Long-range analysis on the ground state	38
2.5	Predictions	43
2.6	Achievements	45
2.7	Filtered Laser Excitation	47
	LIF complementary data	51
	Summary of observations	52
2.8	The interaction potential	53
2.8.1	Improvement of the potential	53

3	Precision of the long-range parameters	57
3.1	Introduction	57
3.1.1	Motivations	57
3.1.2	How to determine the confidence interval?	58
3.2	Parameter distribution	58
3.2.1	The general case	58
3.2.2	The Monte Carlo simulation	59
3.2.3	Implementation of the Monte Carlo simulation	61
3.3	Results	62
3.3.1	From the distribution to the confidence limits	62
3.3.2	Meaning of the confidence limits	63
3.3.3	Precision of the C_6, C_8, C_{10} and D_0 values	64
3.3.4	The exchange contribution	67
3.3.5	Comparison with other published values of the C_n coefficients	69
3.4	Critical analysis	70
3.5	Predictions	74
3.5.1	The s-wave scattering length	74
3.5.2	The last bound level	75
3.5.3	Analytic dependence	76
3.6	Continuation of the study	76
4	The calcium dimer B state	85
4.1	Introduction	85
4.2	Potential energy curve	86
4.3	Analysis	87
5	The A–c coupled electronic states . . .	91
5.1	Spectroscopic measurements	92
5.1.1	Background	92
5.1.2	Spectroscopy	93
5.1.3	Revision of the vibrational assignments	101
5.2	Theory	105
5.2.1	Basis functions	106
5.2.2	Matrix elements	108
	Selection rules	108
	Diagonal matrix elements	108
	Off-diagonal matrix elements	109
5.2.3	Fourier grid Hamiltonian method	112
5.3	Deperturbation analysis	115
5.3.1	Two-states model	115

	Initial potential guesses	115
	Constructed potential curves	117
	Spin-orbit coupling	118
	Result of the fit	119
5.3.2	Three-surfaces model	120
	Potentials and couplings	120
	Result of the fit	121
5.3.3	Four-surface model	122
5.3.4	Variations of the spin-orbit coupling	125
5.4	Discussion	126
5.4.1	Verification of approximations in the model	126
5.4.2	Comparison with the previous study	128
5.4.3	Predictions	128
5.5	Conclusion	131
6	Conclusion	135
A	Tables of parameters...	139
B	Distributions of the C_6, C_8, C_{10} coefficients	147
C	Concentration of Ca and Ca₂ in the oven.	149

Chapter 1

Introduction

Twenty years ago the demonstration that light could be used to cool and confine atoms to the sub-millikelvin range has opened many fascinating new chapters in atomic, molecular, and optical physics [Phillips W.D et al., 1985, Dalibard J. and Cohen-Tannoudji., 1985]. A considerable development of the cooling and trapping techniques followed and led to the observation of exciting phenomena where the wave character of matter plays a fundamental role. The realization of the Bose-Einstein condensation (BEC), the progress on the atomic Cs clock, and the very recent investigations of quantum degeneracy with fermionic atom pairs [Regal C.A. et al., 2004, Bartenstein M. et al., 2004], exemplify the achievements in the domain.

The alkaline atoms are the widely used elements in all these developments. Since few years, the scientific community turns its efforts towards the alkaline-earth elements. The reason is that the group-IIa atoms offer in the same time a strong dipole transition from the ground state 1S_0 to the 1P_1 state suitable for efficient trapping and cooling to the millikelvin range and a forbidden transition from the ground state 1S_0 to the $^3P_{0,1,2}$ state presenting interesting conditions for the development of frequency standards. Both transitions are found in the optical domain for Ca and Sr providing favorable frequency ranges for the use of laser radiations. The most abundant isotopes of the alkaline-earth atoms have no nuclear spin except for Beryllium, and in consequence present no hyperfine structure. Thus, the mechanisms developed with the alkalis to reach ultra-low temperature using the multiplicity of sub-levels of their atomic states cannot be applied. Therefore, new strategies, like additional cooling on the ultra-narrow lines employing the quench-cooling technique, which enhance the cooling force, have been proposed. The possibility to reach ultra-cold temperatures (micro Kelvin regime) using this technique has been demonstrated with Ca atoms [Binnewies T. et al., 2001]. The figure 1.1, sketches the energy levels of the alkaline-earth elements and

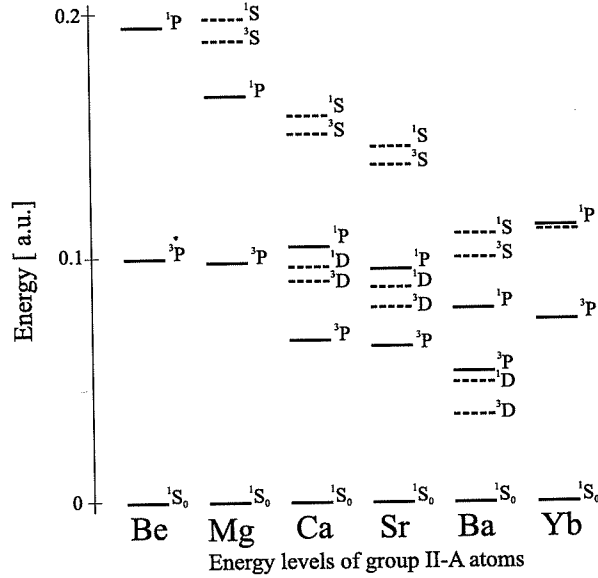


Figure 1.1: Lower levels structure of Group-II atoms.

of the Ytterbium atoms, which presents a similar structure. The group-IIa elements have two valence electrons filling entirely the ns orbital above the closed core $[1s, \dots np^6]$. The $1,3D$ states and the $1,3S$ shift downwards in energy as the atomic mass increases. For all the alkaline-earth elements the $1,3S$ levels are located above the $1,3P$ states. For Be and Mg the $1,3D$ states are above the $1,3P$ states but lie between the $1P$ and the $3P$ states for Ca and Sr, and are below the $1,3P$ states for Ba. The relativistic interactions increase with the atomic mass. Therefore, the mixing of the $3P_J$ states with other states, which have an allowed dipole transition to the ground state, raises. In consequence, the lifetime of the intercombination line for the heavier Sr and Yb atoms is sufficiently low to use this transition without the quench-cooling technique to cool further these two atoms to the micro Kelvin range. Temperature of 400 nK was achieved with the Sr atom [Katori H. et al., 1999] and around $20\mu\text{K}$ with the Yb atom [Kuwamoto T. et al., 1999]. Quantum degeneracy has been recently obtained with Yb atoms using a far-off resonant trap (FORT) by the same group [Takasu Y. et al., 2003].

The cold and ultra-cold binary collisions occupy a strategic position in the physics of dilute, weakly interacting atoms. The understanding and the quantitative description of the collisional processes allow precise determinations of atomic and molecular properties and open new possibilities to control with the help of light or magnetic fields the atomic pair interactions [Cornish S. L. et al., 2000]. We understand thus the necessity of an accurate

knowledge of the dimer interaction potentials. For instance one can quote the precise modeling of trap-loss photoassociative spectra in alkali systems for large detuning achieved thanks to the well-known alkali dimer potential energy curves [Williams C.J. et al., 1999].

The recent progress in the realization of an optical frequency standard using the calcium intercombination line $^3P_1(m_j = 0) \leftarrow ^1S_0$ [Wilpers G. et al., 2002] and the attempts by different groups to reach quantum degeneracy with ^{40}Ca atoms [Hansen D.P. et al., 2003] show the necessity of a comprehensive study of the collisions between two calcium atoms. Recent results on binary collisions between two calcium atoms, one in the ground state 1S_0 and one in the excited state 1P_1 have been obtained by photoassociation spectroscopy [Degenhardt C. et al., 2003]. To describe the intensity pattern of the photoassociative spectra, an accurate knowledge of the Ca_2 ground state is required. At short range the collision partners, under the photoassociative radiation, can encounter change of state leading to trap losses. To describe these phenomena we need to know precisely the involved molecular potentials dissociating to different asymptotes and their couplings. Therefore we have engaged a systematic study of the calcium dimer states and in particular those correlating to the $^1S_0 + ^1S_0$ and the $^3P_1 + ^1S_0$ asymptotes.

The alkaline-earth homonuclear dimers have a shallow ground state and a total electronic spin equal to zero. The closed s-shell of the atoms gives a main van der Waals character to the binding interaction. Such behavior is also known for the group-VIII, the rare gases, and for the group-IIb, (Zn, Cd, Hg). It is characteristic of the van der Waals diatomic molecules that the lower state is only weakly bound with a large equilibrium distance, whereas the excited states are strongly bound with their minimum positions at relatively shorter internuclear distances. Additionally, the most abundant atomic isotopes have no nuclear spin, and have a single ground state $^1\Sigma_g$ (except Beryllium).

Little is known so far about the shape of the potentials of the diatomic alkaline-earth molecules. For the calcium dimer, few spectroscopic studies and ab-initio calculations were realized on the molecular structures. The theoretical study of the bond nature of the calcium dimer started with the work of R. O. Jones in 1979 [Jones R., 1979] followed by the study of metal-cluster bindings by [Pacchioni G. and Koutecky, 1982] and [Ortiz G. and Ballone P., 1991]. The first determination of potential energy curve was achieved for the ground state by [Dyall K.G. and Mclean A.D., 1992]. Recent calculations of the complete structure concerning the lower states were published by [Czuchaj E. et al., 2003] and concerning only the ($^1P+^1S$) and ($^3P+^1S$) asymptote in [NIST-databases, 2004]. Several states calculated in the two last mentioned investigations, are differing significantly, in particular

the states correlated to the ($^3P+^1S$) asymptote. To obtain accurate ab-initio potential energy curves is very difficult due to the complexity of the calculations. The obtained potential curves are often not sufficiently precise for the description of the observed spectra and the cold collision phenomena but provide important information for the assignment of spectra and give useful onsets for accurate determinations of PEC from experimental studies.

The experimental study of the calcium dimer started in the middle of the

Simplified level scheme for Ca_2

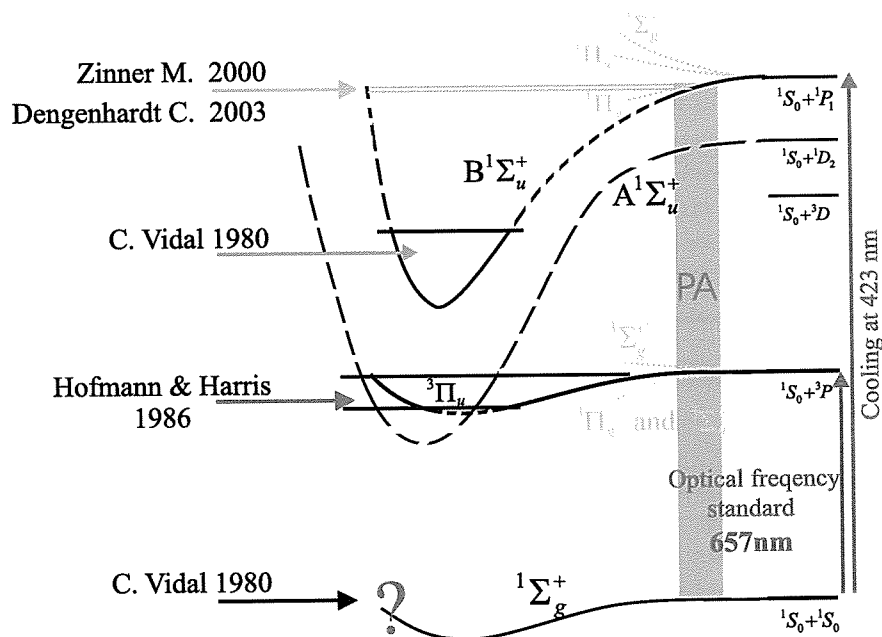


Figure 1.2: Simplified level scheme and studied region of the calcium dimer. The full lines indicate studied part of potentials, and the dashed lines represent regions, which were not investigated up to now. The question mark indicates that the repulsive branch of the ground state potential presents a non-physical shape. PA: Photoassociation.

seventies by the observations of molecular transitions obtained by absorption spectroscopy which was achieved by [Balfour W.J. and Whitlock R.F., 1975]. Investigations on the $A^1\Sigma_u^+$ state correlated to the $^1D_2 + ^1S_0$ coupled to the $c^3\Pi_u$ dissociating to $^3P + ^1S_0$ were realized by LIF spectroscopy and molecular constants have been derived by [Bondybey V. E. and English J.H., 1984] and [Hofmann R. T. and Harris D. O., 1986]. The long-range region of the $B^1\Sigma_u^+$ has been studied by photoassociation spectroscopy in the group

of F. Riehle with the collaboration of E. Tiemann and reported in [Zinner G. et al., 2000] and [Degenhardt C. et al., 2003]. The only determinations of potential energy curves concern the ground state $X^1\Sigma_g^+$ ($^1S_1 + ^1S_0$) and the $B^1\Sigma_u^+$ ($^1P_1 + ^1S_0$) state for the short internuclear distances and have been achieved by W.J. Balfour and R.F. Whitlock [Balfour W.J. and Whitlock R.F., 1975] and later by C. Vidal in 1980 [Vidal C. R., 1980]. The figure 1.2 presents the studied region of the potentials. The published potential energy curve for the ground state presents a non-physical behavior at its repulsive part. The lack of explanations in the article concerning this fact led us to ask for having the original spectroscopic data. Unfortunately, these data have been lost! Consequently, a complete re-investigation of the ground state of the calcium dimer becomes necessary.

This thesis work is devoted to the study of the ground state potential energy curve up to large internuclear separations and the prediction of cold collision properties between two Ca atoms in their 1S_0 ground state. Potential energy curves corresponding to molecular states $B^1\Sigma_u^+$, $c^3\Pi_u$ and $A^1\Sigma_u^+$ correlating respectively to the asymptotes $^1P_1 + ^1S_0$, $^3P + ^1S_0$, and $^1D_2 + ^1S_0$ will be investigated.

The Hamiltonian describing a colliding pair of atoms and the Hamiltonian of two bound atoms forming a diatomic molecule are the same. Therefore, the knowledge of the molecular potentials up to large interatomic separations allows to describe and to make reliable predictions on the collision processes. By the knowledge of the positions of the bound levels of the potential wells from the deeply bound region to the asymptotic limit, one can construct the corresponding potential curves up to large internuclear separations by a procedure of inversion involving full quantal methods. This approach is well developed, and one can quote, for instance, two experimental works: in [Seto J.Y. et al., 2000] the observation of the energy ladder of the ground state of Rb_2 allowed a full determination of its potential energy curve and in [Jones K.M. et al., 1996] the combination of conventional molecular spectroscopy and photoassociative spectroscopy of ultra cold atoms permitted a direct measurement of the ground state dissociation energy of Na_2 .

The chapter II, is devoted to the determination of the ground state $X^1\Sigma_g^+$ of Ca_2 . The spectroscopic study is presented and followed by an explanation of how potential energy curve can be extracted directly from the observed molecular bound levels. In the following, we will address and answer the question of the reliability of the derived potential energy curve. It is an important issue that the derived potential provides an accurate description of all the observations. But we ask more, we want to use this potential to predict binary collision properties observable in ultra-cold dilute Ca gases. In the chapter III we are proposing a simple and precise method to transfer

the knowledge of the precision of positions of observed levels, to the precision of predictions determined with the derived potential. The chapter IV deals with the determination of the potential energy curve of the $B^1\Sigma_u^+$ state. The last chapter exposes the measurements and the analysis on the $A^1\Sigma_u^+ - c^3\Pi_u$ coupled states.

Chapter 2

The calcium dimer ground state

In the following section, I will present what is known about the ground state and explain in more detail the problem appearing on the repulsive part of the potential curve, which has been derived by C. Vidal [Vidal C. R., 1980]. Then the experimental study to obtain the position of bound level of the ground state in the relatively deep bound region will be presented and followed by an analysis of the reliability of the long-range part of the potential when a limited set of data near the asymptote has been collected. In the next section, I will describe the measurements to obtain more levels near the dissociation limit. With this enriched data set an accurate potential curve will be derived up to very large internuclear separations. The reliability of the predictions derived from the potential curve is an important issue. We will show that it is possible to transfer the knowledge of the accuracy of the spectroscopic data to the precision of quantities related to cold atomic collisions.

2.1 What do we know about the ground state?

The study realized by C. Vidal concerns the $B^1\Sigma_u^+ \leftarrow X^1\Sigma_g^+$ system. Transitions between both states have been observed by laser induced fluorescence (LIF) spectroscopy by excitation of the B state with the visible lines of an Ar⁺ laser and a Kr⁺ laser. The induced fluorescence was recorded through a 2m grating spectrometer with an accuracy of 0.02 cm⁻¹. The vibrational quantum numbers ranged from $v' = 0$ to 33 and the rotational quantum numbers ranged from $J' = 11$ to 161 for the B state and from $v'' = 0$ to 34 and $J'' = 10$ to 162 for the ground state. A set of Dunham¹ coefficients from the spectroscopic data has been obtained. The Dunham coefficients are a set

¹see equation 2.4 in section 2.3 page 33 or for more details see [Herzberg G.,] or the original paper by Dunham [Dunham J. L., 1932].

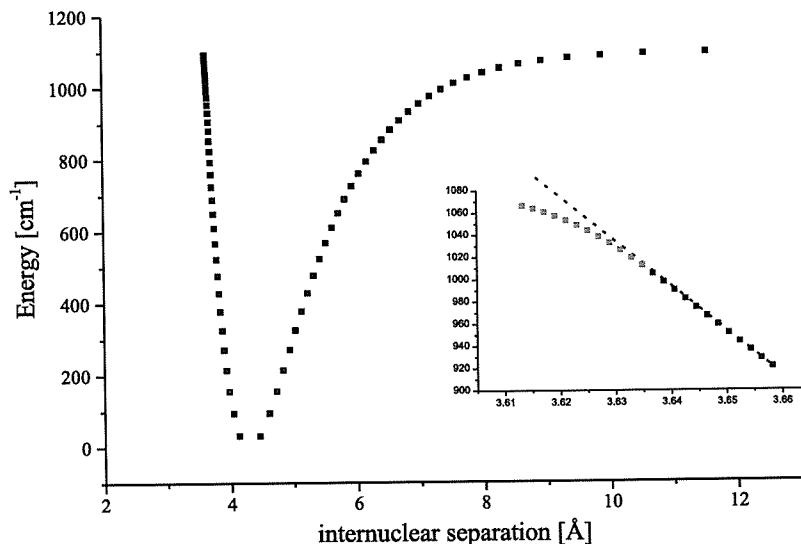


Figure 2.1: IPA potential published in [Vidal C. R., 1980]. A zoom of the repulsive branch near the asymptote is inserted. The dashed line shows a regular shape of the repulsion branch.

of parameters representing the energy positions of the bound rovibrational levels. Considering the shape of the potential to be almost harmonic and treating the non-harmonic correction by the quantum theory of perturbation one can derive this set of parameters. A Rydberg-Klein-Rees (RKR) potential has been derived using the set of Dunham coefficients. The RKR method allows to calculate the classical turning points of the vibrational level ladder of the potential using a set of Dunham coefficients (an explanation can be found in the text book [Lefebvre-Brion H. and Field R.W., 1986]). Employing the inverted perturbation approach IPA (a description of the method can be found in [Vidal C. R. and Scheingraber H., 1977]), the author improved the potentials for the B and X states, and claimed that they can represent the observed data with the standard deviations of respectively 0.025 cm^{-1} and 0.031 cm^{-1} . The IPA potential of the ground state is plotted in figure 2.1. In the inset, an enlargement of the repulsive part of the potential shows a significant deviation from a regular behavior. The RKR potential presents the same irregularity. Such inflection is not expected for a ground state potential. The states, which can couple with the ground state and produce an avoiding crossing, are lying several thousands of wave numbers higher in

energy. Their weak influence cannot produce such inflection. This kind of irregular behavior comes usually from the set of Dunham coefficients from which the RKR potential is derived. Close to the asymptote the Dunham coefficients fail to represent correctly the energy positions of the observed levels due to the strong anharmonicity of the potential. One can compensate the resulting deviation by imposing, for instance, strong constraints to the repulsive branch. The IPA method which is used to correct the shape of the potential using directly the observed data should permit to remove such unphysical behavior. Due to the loss of the original data it is not possible to understand why the IPA conserves this inflection. A complete experimental reinvestigation of the level structure of the ground state is a necessity and will be achieved mainly by laser induced fluorescence spectroscopy.

2.2 Laser induced fluorescence experiment

2.2.1 LIF Setup

A scheme of the apparatus is presented on the figure 2.2. The set up is composed of three main parts. We have a cell to obtain a vapor of calcium dimer, a system of lasers to irradiate the vapor, and a Fourier transform interferometer to spectrally resolve their induced fluorescence emission. The Fourier transform interferometer is a Bruker IFS 120HR and it can work in a spectral range from 63200 cm^{-1} in the ultra violet region to 450 cm^{-1} in the infrared region.

One difficulty of this experiment comes from the high temperature (more than 1200 K) necessary to obtain a sufficiently dense vapor of calcium atoms which collide to form Ca dimers (see the appendix C). A special cell has been constructed following the model of a heat pipe oven [Vidal C. R., 1980] and this cell is described in the next section. Inside the heat pipe oven the calcium vapor is irradiated by the lines of a multimode argon ion laser (Coherent CR-2000K) with an output power of 1 to 1.5 W. These lines are known to excite several transitions of the $B^1\Sigma_u^+ \rightarrow X^1\Sigma_g^+$ [Balfour W.J. and Whitlock R.F., 1975] and [Vidal C. R., 1980]. The fluorescence light emitted in the backward direction is reflected by a mirror pierced by a horizontal slit. This slit lets pass the incoming laser beam without reducing too much the reflection surface of the mirror. A set of two lenses (lens 1 and 2, see the picture 2.2) collects the fluorescence light. The first lens of 60 cm focal length converts the fluorescence beam, coming from the center of the pipe, to a parallel beam. The second lens of 20 cm focal length focuses it onto the aperture of the Fourier interferometer. Between the two lenses, color glass

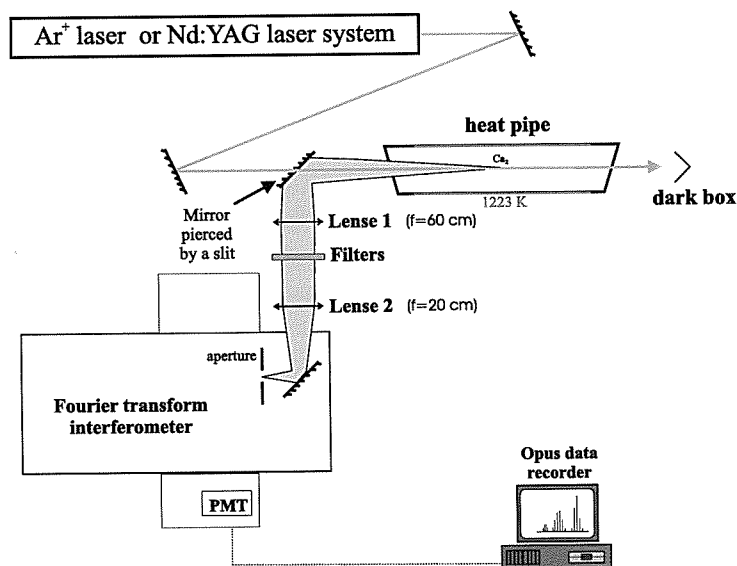


Figure 2.2: schematic of the experimental setup for the LIF experiment where the fluorescence is treated via a Fourier transform interferometer.

filters are placed to cut the unwanted light coming from the oven in order to reduce the noise and the background light of the recorded spectra. Additional interference filters with their band pass centered at 550 nm and 546 nm were used for the observation of transitions to the last bound levels of the ground state. A photomultiplier tube (Hamamatsu R928) detects the light at the output of the interferometer. The interferometer is controlled via a computer interface equipped with the OPUS software system. This system calculates Fourier transformation of recorded interferograms and allows processing the spectra.

The heat pipe oven

The heat pipe cell is made of a stainless steel tube heated around 1220K. The oven used to heat the cell is a commercial one from the Kanthal firm. It allows to reach temperatures closed to 1500K and can be used to heat any tube having a diameter smaller than 60 mm. The pipe has a length of 960 mm, a diameter of 34 mm, and a wall thickness of 2 mm. A schematic of the heat pipe oven is presented in the figure 2.3. It is filled with approximately 5 g of calcium granule composed of 99.5% of calcium. The natural isotopic abundance of ^{40}Ca is 96.94%. Each end of the tube is closed by an anti-reflection coated glass window allowing an optical access for the laser and the emitted fluorescence. The windows are mounted on coolers whose purpose

is to remove the heat radiated and conducted through the metal pipe by the very hot central part. A flow of 1 liter per minute is sufficient to keep the windows cold. A ceramic insulating tube surrounds the pipe to provide a better homogeneity of the heat. At both ends a metal ring closes the gap

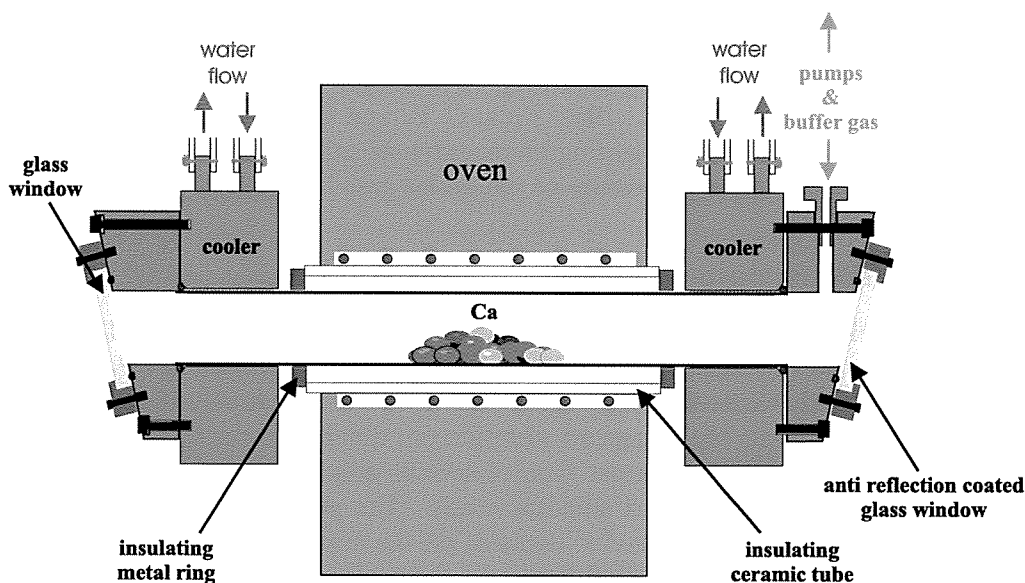


Figure 2.3: section of the heat pipe oven

between the pipe and this tube, reducing strongly the flux of air and thus the loss of heat. On the window holders an access for vacuum pumping and buffer gas filling is provided. A buffer gas, which accumulates in the cold region of the pipe, prevents the calcium vapor to reach the windows. Argon gas is used at a pressure between 10 and 40 mbar (measured at room temperature). We tried helium gas also but it requires a higher pressure to work efficiently as buffer. Some heat is removed by the buffer gas from the calcium vapor causing the condensation to the liquid phase and partly to the solid phase of calcium. The liquid part runs to the center by capillary. In contrast to the alkalis, a metal mesh covering the inner part of the pipe, which is often used to increase the capillary effect, does not offer the same advantage with calcium, and so was not used. The liquid returning in the center of the pipe evaporates again. In this way a continuous cycle of vapor \leftrightarrow liquid \leftrightarrow vapor is created along the heat pipe. This is called the heat pipe regime, and it allows working with one filling during weeks. The formation of solid calcium at the end of the pipe reduces the efficiency of this cycle, emptying the center of the pipe of calcium. After typically 8 hours of operation (using argon) the amount of solid calcium accumulated at both ends blocks the optical path

for the fluorescence. A thin layer is firstly formed and then several dendrites grow across the laser axis stopping the experiment. By heating more the zone where the solid calcium grows we can melt these calcium depots. The liquid calcium runs then to the center again. In this way we can have several runs with only one filling of calcium of the heat pipe. This provided us enough time of operation. It was not necessary to investigate whether an efficient heat pipe regime [Vidal C. R., 1996, Vidal C. R. and Cooper J., 1969] could be reachable or not by investigating more systematically the influence of the oven temperature and the pressure of the buffer gas.

2.2.2 Transitions

The transitions excited during this study with the 514 nm, 496 nm and 476 nm lines of the Ar⁺ laser have been previously observed by Vidal [Vidal C. R., 1980]. Each excited rovibrational level (v' , J') radiatively decays to the vibrational levels of the ground state for two different rotation quantum numbers J'' . The spectra consist then of several progressions of doublets if several transitions are excited simultaneously. The probability of decay to each individual vibrational level v'' depends on the overlap of the wave functions of the excited rovibrational level and the rovibrational level it decays to. One doublet consists of a P ($J'' = J' + 1$) and a R ($J'' = J' - 1$) line as expected from the selection rules for a ${}^1\Sigma_u^+ \rightarrow {}^1\Sigma_g^+$ type system (described in Hund's case (a)) for homonuclear diatomic molecules. In the general form of Hund's case (a) we get,

$$\Omega = \Sigma + \Lambda \quad \Delta\Omega = 0, \pm 1 \quad \text{and} \quad \Delta J = 0, \pm 1$$

Ω is the projection of the total electronic momentum of the considered state along the internuclear axis, in which Λ is the projection of the electronic angular momentum and Σ is the projection of the spin momentum onto the same axis. We have $\Delta J = J' - J''$. For the two states $\Lambda = 0$ and $\Sigma = 0$, $\Delta J = 0$ is forbidden and so only $\Delta J = \pm 1$ holds. In addition, for bosonic atoms in diatomic molecule, only odd values of J exist for the electronic states with u symmetry, and only even values of J for the electronic states with g symmetry, for Σ states. Therefore, the ground state $X^1\Sigma_g^+$ has only even J -values.

The Dunham coefficients determined for the ground state in Vidal's paper were used to assign the observed spectra. Since these Dunham coefficients represent the levels with relatively low quantum numbers of vibration and rotation within an error of 0.046 cm^{-1} it allowed us to assign the observed progressions without ambiguity.

v'	J'		v''	J''	$\nu[cm^{-1}]$
0	97	\leftarrow	7	96	18787.6738(56)
0	101	\leftarrow	7	102	18788.3028(60)
1	111	\leftarrow	13	110	18787.3804(66)
2	21	\leftarrow	9	20	18788.3639(60)
2	25	\leftarrow	9	26	18788.2842(61)
2	69	\leftarrow	11	70	18787.6237(68)
2	77	\leftarrow	12	76	18788.3853(60)
2	99	\leftarrow	15	100	18788.3088(61)
3	57	\leftarrow	14	56	18788.3059(62)
3	85	\leftarrow	18	84	18788.3471(61)
4	27	\leftarrow	16	28	18787.4502(105)

Table 2.1: Transitions of the $B^1\Sigma_u^+ \leftarrow X^1\Sigma_g^+$ excited with a single mode frequency doubled cw Nd:YAG tunable laser.

A previously unassigned transition at 514.5 nm reported by Vidal has been observed and identified to be $v' = 9, J' = 83 \leftarrow v'' = 24, J'' = 84$.

From the calculation of Franck Condon factors² (FCF) between the B and X states, and for the range of excitation energy reachable by the laser sources available at that time in our group, we found that levels with $v' = 2$ are the most favorable to induce fluorescence to the last bound levels of the ground state (figure 2.4 a). We then chose the single mode frequency doubled cw Nd:YAG laser (neodyme yttrium aluminum garnet) radiating around 532.4 nm since the $(2, 21) \leftarrow (9, 20)$ and $(2, 25) \leftarrow (9, 26)$ transitions fall conveniently into its 90 GHz tunable range. The laser line width was less than 10 kHz and the output power was typically 150 mW.

The FCF between $v' = 2$ and the last bound levels are indeed favorable but they are anyway weak and decrease very fast as v'' increases (figure 2.4 b). Another cw frequency doubled Nd:YAG laser (Coherent Verdi-10) was used because it delivers high power (up to 10 W) and has its frequency (the laser was not tunable) which coincides with the $(2, 21) \leftarrow (9, 20)$ transition within the Doppler width. The power applied during our experiment was between 1 W and 3 W. Comparing the width of the transition lines excited by this laser at different laser intensities, no detectable broadening within the experimental resolution have been observed.

The transitions of the B-X system excited by both Nd:YAG lasers are presented in the table 2.1. These transitions have not been observed by

²The RKR potentials of the B and X state published in Vidal's paper were used to calculate the FCF.

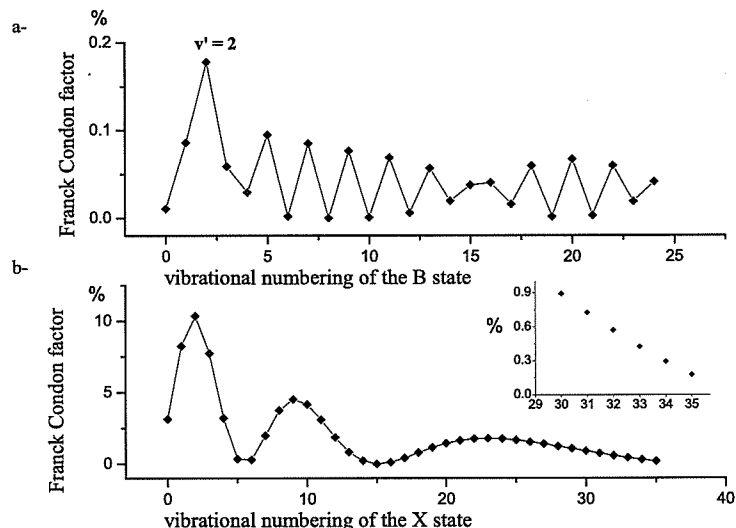


Figure 2.4: a- Franck Condon factors from $v'' = 35$, $J'' = 20$ to the vibrational levels of the B state for $J' = 21$. b- Franck Condon factors from $v' = 2$, $J' = 21$ to the vibrational levels of the X state for $J'' = 20$

Vidal.

2.2.3 Observed spectra

An example of spectrum obtained by excitation with the 496 nm argon ion laser line is presented on figure 2.5. It shows several progressions of P and R doublets. By tuning the Nd:YAG laser and using the powerful Verdi laser we were able to obtain information on the position of levels near the dissociation limit. Using laser radiation with relatively high power increases proportionally the scattered light and thus the noise in the recorded spectra. A band pass filter with a width of ≈ 8 nm centered around 546 nm, where the transitions from $v' = 2$ to the rovibrational levels converging to the dissociation limit with $J'' = 22, 24$ and 26 are expected, was used to compensate for reduction of the signal-to-noise ratio (SNR), since the SNR varies as $1/(BW)^{1/2}$, where BW is the optical bandwidth.

The excitation of the $(2, 25) \leftarrow (9, 26)$ and the $(2, 21) \leftarrow (9, 20)$ transitions resulted in the observation of vibrational progressions reaching respectively $v'' = 34$ for $J'' = 24$ and 26 and $v'' = 35$ for $J'' = 20$ and 22 (see figure 2.6). I should mention that the frequency of the frequency fixed Verdi laser was

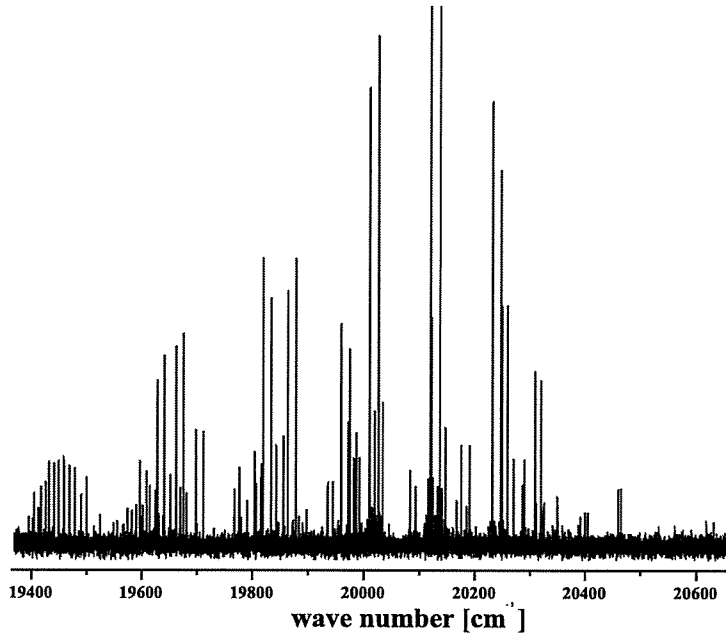


Figure 2.5: Bound-bound spectrum obtain with the 496 nm line of an Ar^+ laser.

slightly dependent of the laser power anyway (the change was smaller than 0.1 cm^{-1}). We used this to excite the two mentioned transitions, which are in fact separated in frequency by more than the Doppler width (0.053 cm^{-1}) just by changing the power of the laser. It should be noted also that each Doppler profiles of the transitions $(2, 25) \leftarrow (9, 26)$ and $(2, 21) \leftarrow (9, 20)$ overlaps with the $(0, 101) \leftarrow (7, 102)$ transition. The spectra of these two transitions are accompanied by the strong bound-continuum fluorescence induced by the excitation of the $(v' = 0, J' = 101)$ level. Progressions from the excited levels $(2, 21)$ and $(2, 25)$ to the energy region close to the dissociation limit are thus recorded on a relatively high background, affecting the signal-to-noise ratio.

In addition to the excited transitions, several collisionally induced transitions have been observed. The population of a laser excited rovibrational level (v', J') is partly transferred to the surrounding rotational levels $J' \pm 2$, $J' \pm 4$, $J' \pm 6 \dots$ due to collisions with the buffer gas atoms. The collisions with calcium atoms lead mainly to molecular quenching. The probability of molecule-molecule collisions is much weaker than for molecule-atom collisions due to the relatively weak density of Ca_2 in the heat pipe. Then, the populated levels radiatively decay to the ground state leading to neighboring

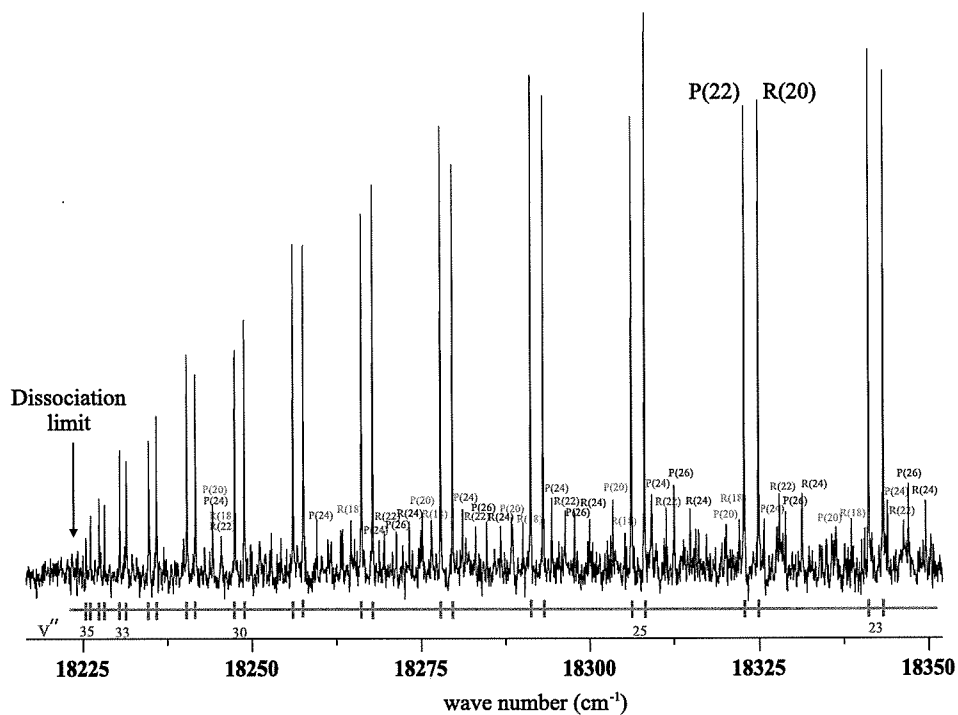


Figure 2.6: Vibrational progression from the excitation of the (2, 21) level of the B state leading to the observation of the highest observed levels ($v''=35$) by the LIF spectroscopy. Rotational satellites lines of the populated (2, 19), (2, 23) and (2, 25) levels, labeled as $P(J''\pm 2)$, $R(J''\pm 2)$, $P(J''+4)$ and $R(J''+4)$, are present as weak lines around each main doublets.

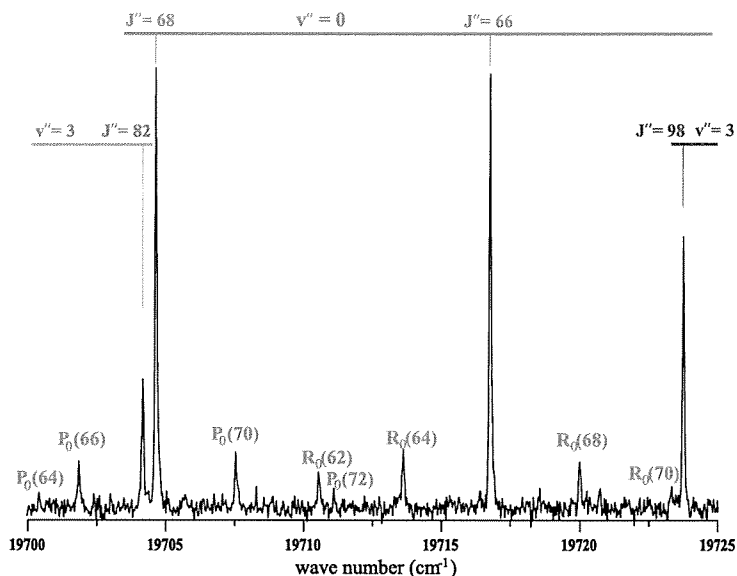


Figure 2.7: Collisionally induced lines are labeled with $P_{v''}(J'')$ and $R_{v''}(J'')$.

doublets around the main doublets induced directly by the laser. In figure 2.7, a portion of the fluorescence spectra obtained with the 514.5 nm line of the Ar^+ laser shows several collisionally induced satellites from the population of rotational levels around the excited (5, 67) level decaying to $v'' = 0$. In figure 2.6 satellites are present and can be followed up to $v'' = 31$.

Additionally, we have observed several shape resonances corresponding to the fluorescence decays $(0, 101) \rightarrow (19, 102)$, $(0, 121) \rightarrow (17, 122)$ and $(0, 161) \rightarrow (9, 160)$. One of them is presented in figure 2.8 where we can see that the fluorescence line corresponding to the transition $(0, 161) \leftarrow (9, 160)$ shows a broadening in the order of 0.5 cm^{-1} .

We have found a few weak progressions that belong to the calcium isotopomer $^{44}\text{Ca}^{40}\text{Ca}$. The excitation transitions by the Nd:YAG laser were assigned to $(0, 42) \leftarrow (4, 43)$ and $(0, 72) \leftarrow (5, 73)$ at 18788.36 cm^{-1} and $(0, 111) \leftarrow (8, 112)$ at 18787.36 cm^{-1} . I would like to mention that the widths of the observed shape resonances and the isotopomer progressions will not be included in the data set that will be used to fit the potential energy curve of the ground state. They can serve as a check of consistency for the determination of the potential.

A total of 2872 transitions have been observed from the $B^1\Sigma_u^+ - X^1\Sigma_g^+$ system involving 730 ground state energy levels. The field of v'' and J'' quantum numbers is given in figure 2.9. It covers rotational quantum numbers from

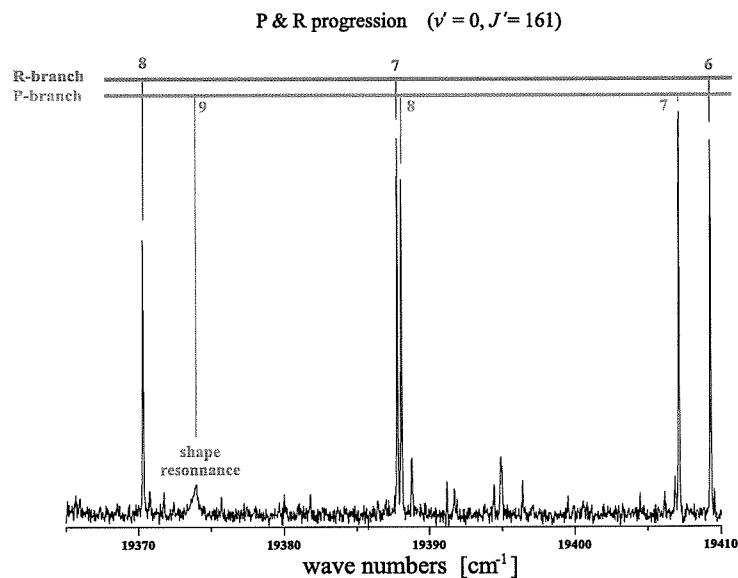


Figure 2.8: Vibrational progression from the $(2, 161)$ B state level presenting a shape resonance for the $v'' = 9, J'' = 160$ ground state level.

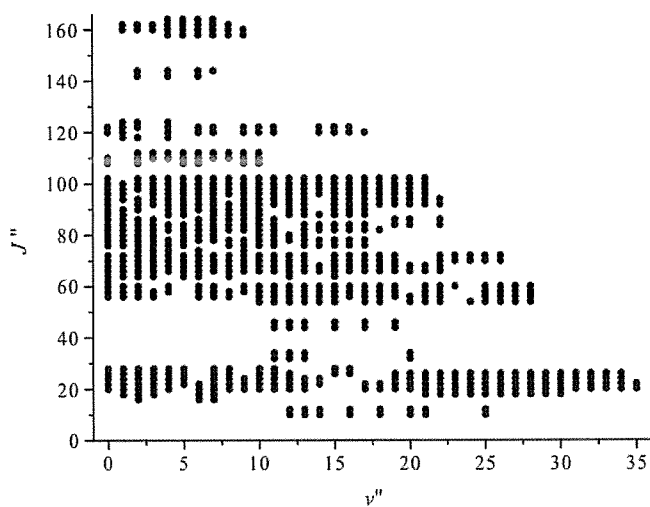


Figure 2.9: Data field of the observed levels of the $X^1\Sigma_g^+$ state.

$J'' = 10$ to 164 and vibrational quantum numbers from $v'' = 0$ to 35. The same range of J'' has been covered by C.R. Vidal in 1980 but more levels with higher vibrational quantum number were observed during our experiment, that is to say, four rotational levels for $v'' = 34$ and two with $v'' = 35$. The observation of $v'' = 34$ clearly indicates the necessity of a revision of the asymptotic behavior of the previously reported ground state potential [Vidal C. R., 1980]. Indeed, the energy position of $v'' = 34$ ($J'' = 0$) is $0.155(7) \text{ cm}^{-1}$ above the predicted asymptote of the IPA potential and even $3.018(7) \text{ cm}^{-1}$ above for $v'' = 35$ ($J'' = 0$). The incorrect behavior of the potential starts already much deeper into the potential. For $v'' = 21$ the difference between our observation and the prediction with the IPA potential already reached 0.1 cm^{-1} which is 2 times the stated accuracy of 0.046 cm^{-1} of the IPA. This confirms that not only the long range behavior of the potential needs to be analyzed again but a rather complete reinvestigation of the ground state potential is necessary.

The observation field consists of a large and dense data set that will allow a precise determination of the potential energy curve. We can already mention that a careful analysis should be made about the extrapolation to the long range region of the potential since the very last bound levels are not observed. But, before describing the procedure to determining the potential energy curve (PEC) I will present in detail the estimation of the experimental uncertainties of the positions of our observed lines obtained by the Fourier transform spectroscopy.

2.2.4 Experimental uncertainty

A special care should be exercised on the determination of the experimental uncertainties. As we will see later, the determination of the reliability of quantities of interest, like the van der Waals coefficients or the s-wave scattering length is based on the data accuracy. We will determine the different contributions which lead to the profile of the observed lines. Then a determination of the experimental uncertainty will be given.

Doppler broadening The main contribution to the experimental uncertainty comes from the Doppler broadening of the molecular lines when exciting with a laser running in multi-mode. The Doppler width is given by the following relation, see for example the Demtröder's text book [Demtröder W.,].

$$\delta\omega_D = (2\omega_0/c)\sqrt{2RT \ln 2/M} \quad (2.1)$$

R is the gas constant, T the temperature of the gas, M the molar mass of the molecule under study, c the velocity of light in vacuum and ω_0 the central frequency of the molecular emission line. The temperature of the Ca₂ sample being 1223 K and for a typical line frequency³ of 21000 cm⁻¹, the Doppler width is then 0.059 cm⁻¹. The mass of ⁴⁰Ca₂ is two times the mass of Ca and $m_{40Ca} = 39.9625912 m_{12C}$ ($m_{12C} = 1.66053886 \times 10^{-27}$ kg from [NIST1,] and [NIST2,]).

Instrumental broadening The Fourier interferometer uses a frequency stabilized Helium Neon laser to set the stepping motion of the scanning mirror. It gives a relative accuracy better than $0.5 \times 10^{-7}\sigma$ and an absolute accuracy better than $5 \times 10^{-7}\sigma$, where σ is the frequency in wave number⁴. The interferogram of a monochromatic line is a sine function of the optical path difference which extends to infinity. Practically, the path of the scanning mirror is limited. One can only record a fraction of length L of the sine function. This limitation introduces a broadening of the observed lines. The shape of a recorded line is obtained by the convolution product of the real profile with the instrumental line shape function. This function is simply the Fourier transform of the rectangular function of length L. The instrumental function in the Fourier space is equal to:

$$I_f(\sigma) = 2L \operatorname{sinc}(2\pi(\sigma_0 - \sigma)L), \quad (2.2)$$

where σ_0 is the central frequency of the line and L the optical path difference used in the recording. The full-width at half-maximum is, in terms of wave number, $\delta\sigma \approx 1.21/2L$

Another inconvenience of a finite path difference comes from the fact that this instrumental function has side lobes or "feet" which could be mistaken with lines of nearby wavelengths. To avoid such confusion the size of the "feet" are reduced by the process called "apodization". The idea is simply to replace the rectangular function by another function whose Fourier transformation leads to a line shape with smaller side lobes. Depending on the choice of the apodization, the full-width at half-maximum can change significantly. We have chosen to use a triangular function giving an instrumental line width equal to $\delta\sigma \approx 0.9/L$ for some of our spectra. But most of the time we used the rectangular function also called Boxcar for apodization. Following the Rayleigh criterion, two lines are resolved if the maximum of one line falls at the first zero of the other line. This criterion leads to the following

³For reference the frequency of the 476 nm Argon line is 20981.12 cm⁻¹.

⁴At $\sigma = 21000\text{cm}^{-1}$ the absolute accuracy is 0.01 cm⁻¹ and the relative accuracy is 0.001 cm⁻¹.

relations between the optical path difference and the resolution (RES) for an unapodized interferogram (1) and for a triangularly apodized interferogram (2):

$$(1) \quad \text{RES} = 1/2L \qquad (2) \quad \text{RES} = 1/L$$

We can now relate the instrumental line width (ILW) to the desired resolution: $\delta\sigma_{ILW} \approx 0.9/\text{RES}$ for triangular apodization.

The IFS-120 Bruker interferometer has a slightly different definition of the optical path difference (OPD) $\text{OPD} = 0.9 L$. This leads to a line width which is $\delta\sigma \approx 0.68 \times \text{RES}$ for the Boxcar apodization and equal to the resolution in the case of a triangular apodization $\delta\sigma \approx \text{RES}$. We selected a resolution of $\text{RES} = 0.05 - 0.06 \text{cm}^{-1}$ to record the spectra of Ca_2 . This choice was also made as a compromise between the expected Doppler line width and a reasonable time of recording.

Aperture For the experimental uncertainty one should not forget to take into account an additional broadening of the line and a shift in frequency introduced by the extended light source or, equivalently, introduced by the finite optical aperture of the interferometer. Because the source is not a point source a part of the rays inside the arms of the interferometer are slightly oblique. The calculation of the consequent shift and broadening are clearly presented in the reference [Bell R. J., 1974] and only the resulting formulas will be mentioned here. The wave number spread $\delta\sigma_{\text{Apt}}$ and the shift in the wave number scale $\Delta\sigma_{\text{Apt}}$ are given by

$$\delta\sigma_{\text{Apt}}/\sigma_0 = d_{\text{Apt}}^2/8f_{\text{col}}^2 \qquad \Delta\sigma_{\text{Apt}}/\sigma_0 = -d_{\text{Apt}}^2/16f_{\text{col}}^2$$

where $f_{\text{col}}=41.8 \text{ cm}$ is the focal length of the curved mirror at the entrance of the instrument collecting the light from the aperture of finite size d_{Apt} . The typical diameter used to get enough light and a not too large broadening and shift was equal to 1.3 mm . We have then a broadening of the lines of the order of 0.025 cm^{-1} and a wave number scale shifted by -0.013 cm^{-1} at $\sigma_0 = 21000 \text{ cm}^{-1}$. The OPUS software provided to control the interferometer corrects automatically the shift in the frequency scale.

Summery Finally the resulting line profile is the convolution of the Doppler profile and the instrumental profile. The line width can be obtained in good approximation by the following relation with the considering that the instrumental profile which is a sinc function does not differ significantly from a Gaussian profile:

$$\delta\sigma \approx [(\delta\sigma_{\text{Doppler}})^2 + (\delta\sigma_{\text{ILW}})^2 + (\delta\sigma_{\text{Apt}})^2]^{1/2} \qquad (2.3)$$

The lifetime of the B state is in the order of 22 ns (width $\approx 0.0015 \text{ cm}^{-1}$) [Bondybey V. E. and English J.H., 1984] which is negligible compared to the other contributions.

Using this relation, one obtains a line width equal to 0.071 cm^{-1} around 21000 cm^{-1} , which corresponds effectively to the typically observed line width at a temperature around 1220 K. Some of the spectra were recorded at higher temperature and/or at different buffer gas pressure. We have seen some dependence of the line profile under these different conditions. The reduction of the lifetime of the excited levels by collisions with calcium atoms can explain the broadening of the transition lines we observed. The level positions, mainly of the excited state, are expected to be also shifted by the collision process. This affects of course our accuracy. So most of the spectra were recorded using lower temperatures than 1250 K and buffer gas pressure lower than 40 mbar (at room temperature) since under these conditions no significant broadening was observed within our resolution.

Signal-to-Noise ratio The determination of the position of the center of a line depends on the width of the line, the signal-to-noise ratio and the number of points falling along its profile from the digital recording. For lines with a signal-to-noise as low as $1 \sim 2$ an uncertainty of 0.03 cm^{-1} was estimated. The uncertainty was taken to 0.01 cm^{-1} for a line with a SNR higher than 5. In order to improve the accuracy of our measurements, the same LIF spectra were recorded several times. Some transitions were observed up to 15 times. By averaging these transitions weighted by their SNR we could reduce the uncertainty on the value of the transitions. In fact, as it will be mentioned in the next section, differences between transitions have been constructed. So it is these differences which were averaged.

2.3 Determination of the interaction potential

Before explaining the procedure of construction of the potential, I will explain how we extracted, in a simple way, information only about the ground state from our observations. By LIF experiment we normally collect less data on the excited state than on the lower state. Therefore, the determination of the two involved electronic states using the observed transitions does not seem justified. The procedure would need to overcome the problem of the existing strong correlations between the two states by the limited data set.

Predictions using only one of the states would then become questionable. The way to extract from the observed spectra information concerning the ground state is to calculate differences between transitions which originate from a common upper level. The main advantage of this method is to suppress the influence of the excited state. This is quite important since, in our case, the $B^1\Sigma_u^+$ state is expected to be perturbed [Vidal C. R., 1980]. In addition, the collisional shift of the spectral lines, we have discussed previously, might be of the same order of magnitude than the experimental accuracy. Since in most cases, the influence of the collisions is larger for the excited state levels than for the ground state levels, building differences will permit to decrease the influence of this effect.

Several spectra were recorded with a single mode laser. If the laser is not tuned exactly to the maximum of the Doppler profile, a significant shift of the fluorescence frequency is induced. Calculating the differences will allow reducing the influence of this Doppler shift below the experimental uncertainty. Since this shift is frequency dependent it will not be the same for the different transitions of a fluorescence progression and cannot be completely eliminated. The residual shift is expected to be reduced to $\approx 0.003 \text{ cm}^{-1}$.

We have restricted the possible combinations of differences between transitions in a progression to crossed differences. That is to say, for each P line (similarly for R line) of one progression (of doublets) we calculated the differences between all the R lines of the same progression (similarly for all P lines). So we have ignored the differences within P lines and within R lines. We have mentioned earlier that some progressions have been observed several times. In this case the differences between transitions have been formed within each progression and then statistically averaged weighted by the accuracy of the considered line center of the transition lines. We have obtained in this way a set of more than 6500 differences from the 2872 observed transitions, which will compose our data basis to determine the $X^1\Sigma_g^+$ state potential energy curve.

2.3.1 Construction of the potential energy curve

When a large set of observed energy levels has been collected, one usually desires to find a reduced set of parameters of an appropriate function of the vibrational and rotational quantum numbers v and J which provides an accurate description of the data ensemble in a compact form. For example, the Dunham expansion is widely used [Dunham J. L., 1932] and [Herzberg G.,],

$$E_{v,J}^\alpha = \sum_{l,m} Y_{l,m}^\alpha (v + \frac{1}{2})^l [J(J+1) - \Omega^2]^m \quad (2.4)$$

where the $Y_{l,m}^\alpha$ are the so-called Dunham coefficients. This representation works for many states but fails to describe states which present a shelf shape or a double well structure.

Although the Dunham representation is very useful for regular potentials, our interest is to go beyond the simple data regression. We want to describe the interaction between two colliding calcium atoms in their ground state. To fulfill this goal we need to determine the potential of interaction represented by the potential energy curve (PEC).

The description of the interaction between two ground state Ca atoms relies on the following assumption: The Hamiltonian is treated in the Born-Oppenheimer approximation. We describe the interaction in the single $^1\Sigma^+$ ($^1S_0 + ^1S_0$) channel. The energy separation between the next excited states and the ground state is large (in the order of 10000 cm^{-1}) so the adiabatic picture is applicable⁵.

The Hamiltonian operator for two interacting atoms separated by a distance R is written following the notation of [Lefebvre-Brion H. and Field R.W., 1986] as:

$$\hat{H} = \hat{H}^{\text{el}} + \hat{T}^{\text{N}} + \hat{H}^{\text{ROT}} + \hat{H}^{\text{rel}} \quad (2.5)$$

where H^{el} includes the electron kinetic energy and the electrostatic potential energy for the nuclei and the electrons, T^{N} is the vibrational nuclear kinetic energy, H^{ROT} is the rotational nuclear energy and \hat{H}^{rel} describes all relativistic effects. In the case of the ground state of Ca_2 we have the total electronic spin $S = 0$, $\Lambda = 0$ and $\Sigma = 0$. The Hamiltonian reduces in this case to the simple form in the Born-Oppenheimer approximation:

$$\hat{H} = \hat{T}^{\text{N}}(R) + \frac{\hbar^2}{2\mu R^2} J(J+1) + V_{\text{BO}}^{\text{el}}(R) \quad (2.6)$$

where J is the total angular momentum without the nuclear spin and μ is the reduced mass of the molecule. $V_{\text{BO}}^{\text{el}}(R)$ is the interaction potential which depends only on the internuclear separation in the BO approximation being the eigenenergies of \hat{H}^{el} . The eigenvalues of the total Hamiltonian are the rovibrational energies $E_{v,J}$ and the eigenvectors are the rovibrational wave functions $|\chi_{v,J}\rangle$.

$$\hat{H} |\chi_{v,J}\rangle = E_{v,J} |\chi_{v,J}\rangle \quad (2.7)$$

⁵The adiabatic picture holds when $(\frac{m_e}{\mu}) \frac{E_{\text{kin}}}{\Delta E^{\text{el}}} \ll 1$. Assuming E_{kin} at its maximum value, namely the dissociation energy of the X state $D_e \approx 1000 \text{ cm}^{-1}$ and the separation with the lower excited state $\Delta E^{\text{el}} \approx 10000 \text{ cm}^{-1}$ we have the ratio $0.1 \times (\frac{m_e}{\mu})$ which is very small compared to 1. (m_e and μ are the mass of the electron and of the reduced mass of the molecule)

The problem is to determine the potential energy curve. Once the potential $V_{\text{BO}}^{\text{el}}(\text{R})$ is known the Schrödinger equation 2.7 can be solved, using one's favourite numerical method, to predict interesting properties of the system. In principle the potentials can be found by ab-initio calculations, but obtaining precise potentials is a great challenge for the theoreticians due to the many body nature of the problem.

Another approach is to construct the PEC from the measured transition energies, or, in our case for a single channel analysis, from the differences between energy levels of the considered state. The basic idea is to fit parameters of a potential function such that the eigenenergies obtained by solving the Schrödinger equation with this potential match the observed spectroscopic data. Several methods or approaches have been developed in this scope, using either analytical [Seto J.Y. et al., 2000] and [Samuelis C. et al., 2000] or point-wise representations [Pashov A. et al., 2000b] for the potential function and different strategies to find the parameters either by linear or non-linear fitting procedures. This full quantal method offers the possibility to adjust the potential form directly to the observations without intermediate steps.

In this thesis two approaches have been employed for the determination of the potential of the ground state. The first one uses an expansion over analytic functions to represent the potential. The parameters of the expansion are found by a non-linear fitting procedure. The second representation uses a set of points, treated as parameters, connected by cubic spline functions. Corrections of the positions of the potential points are found by an iterative linear fitting procedure. Both methods have been proven to give potentials which can describe observed data within their experimental uncertainty. Examples are the determination of the Na_2 $\text{B}^1\Pi_u$ state using the analytical representation [Richter H. et al., 1991] and the determination of the double well NaK $6^1\Sigma^+$ state [Pashov A. et al., 2000a] for the point-wise representation.

In the next paragraph I will describe both methods.

The analytical representation The potential energy is represented by a truncated expansion⁶:

$$V(\text{R}) = \sum_{i=0}^n a_i \xi(\text{R})^i \quad (2.8)$$

⁶One can find, for instance, descriptions and comparisons of different choices of representations for the analytical functions in the thesis of Y. Huang [Huang Y., 2001].

over the following analytic functions

$$\xi(R) = \left(\frac{R - R_m}{R + b R_m} \right) \quad (2.9)$$

and $\{a_i\}$, b , and R_m are parameters (R_m is close to the value of the equilibrium distance). At short internuclear distances, the expansion is continuously extended by

$$V(R) = A + B/R^{12} \quad \text{for } R \leq R_{inn} \quad (2.10)$$

and at long internuclear distances by

$$V(R) = D_e^X - C_6/R^6 - C_8/R^8 - C_{10}/R^{10} \quad \text{for } R \geq R_{out} \quad (2.11)$$

Equation 2.10 ensures the steep slope of the repulsive branch and R_{inn} lies usually within the range of inner turning points of the observed levels. The extension at large R , equation 2.11, is used only to fulfill the required boundary conditions for the calculation of the eigenenergies and wavefunctions at this point of the determination of the potential. R_{out} is chosen to lie out of the range of outer turning points of the observed data. We will come back later to these considerations when we will focus our attention to the reliability of the long range extension of the potential.

The $\{a_i\}$ coefficients are determined by a non-linear fitting procedure using the well-known MINUIT program library [MINUIT web page,]. This program is used to fit the potential on the constructed set of energy differences. It minimizes the mean standard deviation $\bar{\sigma}$ defined as

$$\bar{\sigma}^2 = \frac{1}{N - N_p} \sum_i^N \left(\frac{E_i^{\text{obs}} - E_i^{\text{calc}}}{\sigma_i^{\text{exp}}} \right)^2 \quad (2.12)$$

σ_i^{exp} is the experimental uncertainty of the i^{th} energy difference E_i^{obs} and E_i^{calc} is the corresponding calculated energy difference. N is the number of differences and N_p is the number of parameters describing the potential.

In order to speed up the convergence, it is better to start the fitting routine by using already a reasonable guess for the initial set of parameters. For this purpose the RKR potential curve determined in [Vidal C. R., 1980] has been taken to fit a first set of parameters including b and R_m . Then, b and R_m remain fixed during the fitting procedure.

Several analytical potentials have been then adjusted on the observed differences. They were constructed with different sets of a_i parameters composed of 21, 23, and 39 values. The position of the inner connection R_{inn} was varied between 3.5 Å and 3.7 Å and, the outer one R_{out} between 12 Å and 13

Å. These potentials will be used for checking the range of reliability of the final potential. They reproduce the observed differences with a normalized standard deviation of close to $\bar{\sigma} = 0.40$ and an absolute standard deviation of 0.0065 cm^{-1} .

Numerical IPA potential The construction of the potential is based on the Inverted perturbation approach developed by C. Vidal and H. Scheingraber presented in [Vidal C. R. and Scheingraber H., 1977]. The principle is to start by an approximate potential $V_0(R)$, for example an RKR potential, and to seek for corrections $\delta V(R)$ to it, that the set of differences between the eigenvalues obtained by solving the Schödinger equation with $V_0(R) + \delta V(R)$ agree with the differences from observed levels within their experimental uncertainties in the least squares approximation sense. Assuming that the correction should be small compared to the energy difference (if the starting potential is already representing the observed levels sufficiently well) one can find the correction using the first order perturbation approach.

$$\delta E_{v,J} = \langle \chi_{v,J}^0 | \delta V(R) | \chi_{v,J}^0 \rangle \quad (2.13)$$

$$E_{v,J}^0 + \delta E_{v,J} = E_{v,J}^{\text{exp}} \quad (2.14)$$

The correction of the potential is developed over functions as:

$$\delta V(R) = \sum_{i=0}^n c_i f_i(R) \quad (2.15)$$

Replacing $\delta V(R)$ into the equations (2.13) and (2.14) we obtained a system of linear equations where the unknowns are the correction parameters c_i .

$$\delta E_{v,J} = \sum_{i=0}^n c_i \langle \chi_{v,J}^0 | f_i(R) | \chi_{v,J}^0 \rangle = E_{v,J}^{\text{exp}} - E_{v,J}^0 \quad (2.16)$$

Initially Vidal and Scheingraber used an analytical function for $f_i(R)$. The choice of $f_i(R)$ is critical. It is not obvious, in general, which shape the correction must have and if the chosen function will be able to reproduce it. This means that the expansion should be flexible enough to avoid a representation with a too large number of parameters $\{c_i\}$. Pashov proposed an alternative to the analytical expansion. The correction to the potential curve is expressed as a set of n points at equidistant internuclear distances $\{R_i, \delta V_i\}$, connected with a modified cubic spline function [Pashov A., 2000]. This representation of $\delta V(R)$ is very flexible and can handle relatively fast varying corrections with R without a too high number of points. Another

advantage is that the correlations between neighboring points decrease exponentially due to the modified cubic spline functions. The corrections are local.

The system of equation 2.16 is over determined since there are more equations than parameters. It can happen that the data are not significant for a parameter or a particular linear combination of parameters. In this case the value of the parameter combination can tend to get very small values and one would like to eliminate it from the fit and reduce the number of free parameters. By using the Singular Value Decomposition (SVD) technique one can find the fitting parameters, on which the fit depends only weakly. The system of equations is solved numerically using this method.

In the present case of the determination of the ground state of Ca_2 the potential curve is initially defined in the interval 2.7 Å - 13.1 Å using a grid having between 50 and 118 points. As previously the curve is extended at long range by an expansion of the form given in equation 2.11. The coefficients of the expansion are determined by fitting the shape of the potential between 12 Å and 13.1 Å. The connecting point R_{out} is chosen in a way to ensure a smooth connection with the point-wise potential.

A potential in point-wise representation has been determined in this way which can reproduce the set of observed differences with a standard deviation of 0.0068 cm^{-1} and a normalized standard deviation of $\bar{\sigma} = 0.41$.

2.4 Long-range analysis on the ground state

Since our interest is to describe the cold collision phenomena and in particular to make predictions concerning the interaction between two largely separated calcium atoms we need to investigate the reliability of the determined potential curve.

In the previous section we have derived several PECs by two different methods. On the graph 2.10 differences are plotted between the analytic potential with 21 a_i parameters and three other potentials, one analytic with 39 a_i parameters and two point-wise potentials, respectively with 50 and 73 points. As mentioned before, these potentials were smoothly extended from R_{out} close to 13 Å, which corresponds to the largest turning point of the observed levels. These differences will help us to determine whether the extension at 13 Å is reliable.

Because these different potentials reproduce the experimental data with similar accuracy, we can conclude that the fast oscillations, we see on the figure 2.10 for the intermediate range ($R < 10 \text{ Å}$), are within the fluctuations

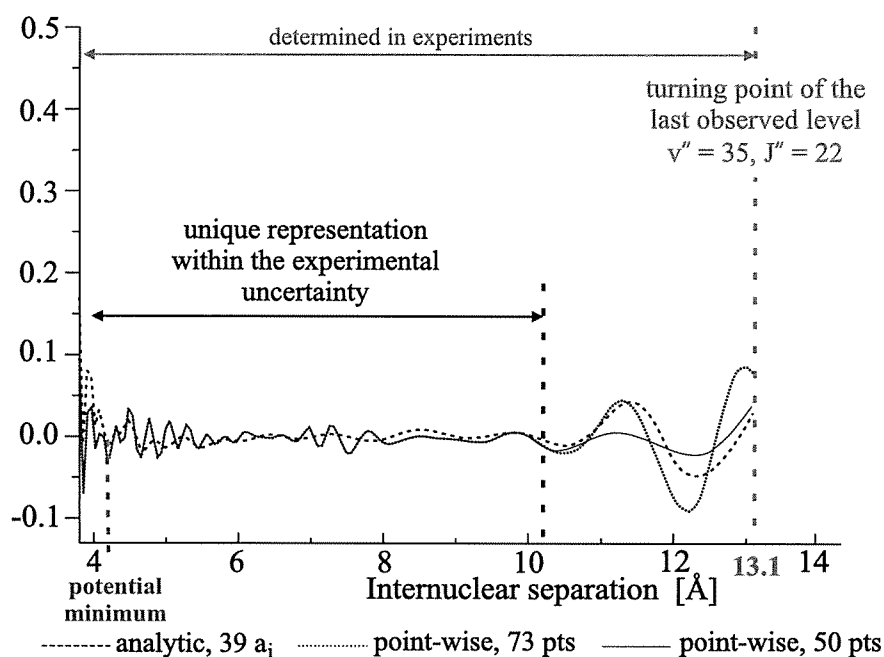


Figure 2.10: Differences between the potentials of the X state obtained using the two representations. The differences exhibit the region where we can consider that the shape of the potential is unique and does not depend on the type of representation.

”tolerated” by the experimental uncertainties. I mean that the difference between the position of a level calculated with a potential presenting this fast oscillations and the position calculated with a potential much smoother is smaller than the experimental uncertainty of the corresponding level. We can understand that solving the Schrödinger equation will integrate over these oscillation structures and thus some averaging occurs. Therefore, improving the experimental accuracy will reduce the differences between the potentials. On the other hand, the amplitude of the oscillations is largely increasing for internuclear separations beyond 10 Å. The range of classical outer turning points from observed levels extend to 13.1 Å but the number of observed levels having an outer turning point beyond 9.5 Å is only 18. This should be compared to the 712 observed levels of which the turning points lie in the region $4.5 \text{ \AA} < R < 9.5 \text{ \AA}$. Obviously the small amount of data beyond 9.5 Å does not allow to determine the shape of the potential without ambiguity. In contrary, for the intermediate region, the large number of observed levels imposes strong constraints on the possible fluctuations of the potentials. The different representations allowed us to determine the range where the

shape of the potential is unique within the experimental uncertainty and reliable. This range is significantly smaller than the range of turning points of observed levels. Moreover, we cannot rely on the position of the outer turning point at 13.1 Å of the highest observed level to extend the potential curve to very large internuclear separations.

This means also that we cannot reliably extend the potential at large separations ($R > 13$ Å) using the physical analytical form (see equation 2.11) valid at large distances.

We have to remind ourselves that the interaction between two calcium atoms is relatively weak due to the two closed atomic s-shells. So, the binding energy should exhibit, in this case, mainly van der Waals character. It is worth then to examine whether it is possible to describe the experimental data by smoothly extend the PEC starting from a connecting point lying at shorter distance. More importantly we need to see if this point can already lie in the region where the potential is uniquely and reliably determined ($R < 10$ Å).

Before making such changes we should estimate the contribution of the exchange energy.

For that, we apply the expression from [Radzig A.A. and Smirnov P.M., 1985] and [Kleinekathofer U. et al., 1995]:

$$V_{\text{exch}}(R) = BR^\alpha \exp(-\beta R), \quad (2.17)$$

where for the Ca_2 ground state $B = 0.067$ a.u., $\alpha = 4.16$ a.u., and $\beta = 1.356$ a.u. A calculation at 9.5 Å gives an energy which is only 0.07 cm^{-1} . This should be compared with the magnitude of the contribution of the smallest discussed dispersion term (i.e C_{10}) which is $\sim 1.5 \text{ cm}^{-1}$. Therefore, we will examine whether the experimental data can be described by a pure long range expansion eq. 2.11 starting from 9.5 Å allowing a physical extension of the potential while keeping the long range model as simple as possible.

Several potentials using the analytic representation has been obtained where the LR C_n dispersion coefficients were directly fitted to the experimental data. All found potentials have similar accuracy ($\bar{\sigma} \leq 0.45$). This means that the data can be correctly represented by potentials having a pure LR form after 9.5 Å. No additional damping (or cut off) functions for the dispersion coefficients should be introduced. A check of consistency was performed by verifying that the quality of fit of the differences did not depend on the choice of representation of the potential. All fitted potential have virtually identical shape for intermediate internuclear distances but have different long-range extension. All of them reproduce, in particular, the levels of which turning points lie between 9.5 Å and 13.1 Å within their experimental uncertainty. Since the LR dispersion can reproduce the experimental data starting in

the region where the PEC is well characterized we can say that the long range representation is reliable. I mean by reliable, that among the obtained long-range extension coefficients we can find with high probability the true parameters of the LR model known by Mother Nature! Following this definition we can say that an extension performed at $R_{out} > 10 \text{ \AA}$ would not be reliable. Unfortunately, the existing experimental data (the 18 levels) are not enough in order to allow a precise determination of the contributions of each dispersion forces. For instance, the value of C_6 varies from $0.7 \times 10^7 \text{ cm}^{-1} \text{ \AA}^6$ to $2.01 \times 10^7 \text{ cm}^{-1} \text{ \AA}^6$. Nevertheless the variation of the value of the dissociation energy D_e^X is quite constraint to an interval of 0.7 cm^{-1} , i.e between 1101.9 cm^{-1} and 1102.6 cm^{-1} .

It is clear that we cannot determine accurately the dispersion coefficients uniquely from the experimental observations. In order to improve our precision and get, as well, a better estimate of the dissociation energy, we can restrict the variation of the leading term in the long-range extension, C_6 , to within a defined interval around the most reliable theoretical prediction of its value.

Among the available calculations of C_6 we can find in the literature, the recent prediction published by S.G. Porsev and A. Derevianko [Porsev S. G. and Derevianko A., 2002], is given together with an estimate of uncertainty. Their value of C_6 was adjusted on experimental data for the electric-dipole matrix element [Zinner G. et al., 2000] and the energy of the principal transition $4p4s \ ^1P_1^o - 4s^2 \ ^1S_0$. The semi-empirical value is $1.070(7) \times 10^{+7} \text{ cm}^{-1} \text{ \AA}^6$ thus only 0.7% uncertainty. We restricted the variation of the value of C_6 to within 5% around the theoretical value which can be understood as a relatively loose constraint.

The sequel analysis was performed and is summarized on the graph 2.11. We have calculated all possible potentials which fulfill the three following requirements.

- (i) All potentials parameters were varied within ranges that allowed an accurate description of the experimental differences especially the ones involving $v'' = 35$. A deviation from the observed positions of two times the experimental uncertainty was allowed.
- (ii) The long-range expansion is smoothly connected to the intermediate expansion eq 2.9 using D_e and C_{10} .
- (iii) The value of the C_6 coefficient was restricted to vary within an interval of $\pm 5\%$ around the theoretical value.

In this way we have obtained a family of potentials "allowed" by the experimental data within the constraint of the value of the leading van der Waals coefficient C_6 . The value of the dissociation energy is now restricted

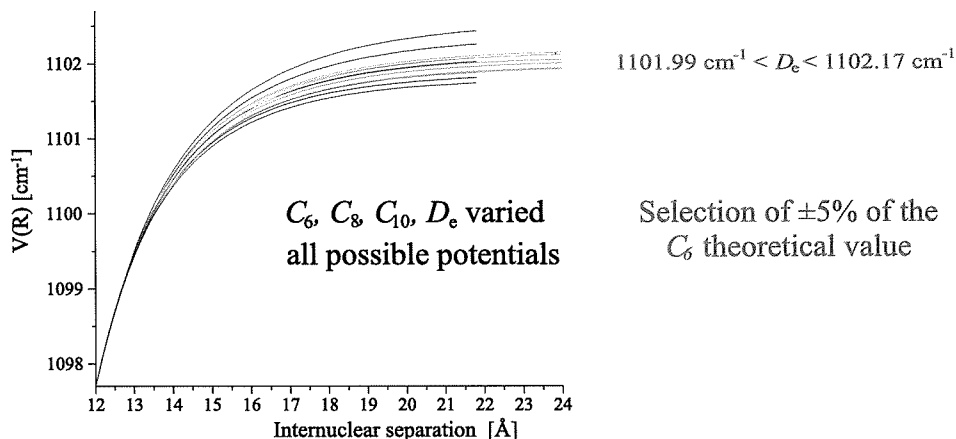


Figure 2.11: Long-range analysis relying on the theoretical value of C_6 leading to a smaller interval for the dissociation energy.

to a much smaller interval $1101.99 \text{ cm}^{-1} - 1102.17 \text{ cm}^{-1}$. This is mainly the position of the highest observed levels, namely ($v'' = 35, J'' = 22$) which gives the lower limit of the interval of the dissociation energy. The calculated position of this level deviates from the observed position by two times the experimental uncertainty (0.017 cm^{-1}) at the lower boundary of D_e^X . The interval obtained for C_8 and C_{10} are presented in the table 2.2. In this table the value of the dissociation energy D_0^X is given with respect to the $v'' = 0, J'' = 0$ level which is observable and which does not depend on the chosen representation of the potential unlike D_e^X .

Table 2.2: Parameters of the long range expansion for the $X^1\Sigma_g^+$ state in $^{40}\text{Ca}_2$ applied in this study and compared with the most recent data from the literature.

$D_e^X, \text{ cm}^{-1}$	1102.08(9)
$D_0^X, \text{ cm}^{-1}$	1069.88(9)
$C_6 \times 10^{-7}, \text{ cm}^{-1}\text{\AA}^6$ selected interval	1.02 – 1.12
$C_8 \times 10^{-8}, \text{ cm}^{-1}\text{\AA}^8$	1.1 – 3.8
$C_{10} \times 10^{-9}, \text{ cm}^{-1}\text{\AA}^{10}$	3.7 – 17.0

A comparison of the present dissociation energy, taking $D_e^X = 1102.08 \pm 0.009 \text{ cm}^{-1}$ as a mean estimate, with the dissociation of the IPA potential determined by [Vidal C. R., 1980] $D_e^X = 1095.5 \pm 0.5 \text{ cm}^{-1}$ shows a deviation

by 7 cm^{-1} (see figure 2.12). We have also recalculated the level positions

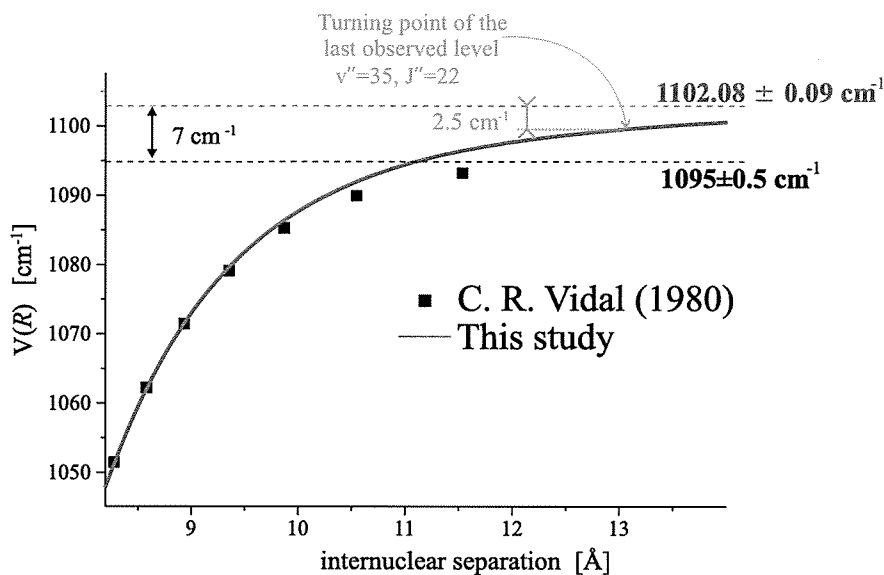


Figure 2.12: Comparison between the $^{40}\text{Ca}_2$ ground state potentials determined by C. Vidal (squares) and derived in this study (solid line) near the dissociation limit. The lower dashed line indicates the value of the dissociation limit determined by C. Vidal. The upper one indicates the dissociation limit derived in this study.

predicted by this IPA potential (a natural cubic spline was used to interpolate the points of this potential) for levels below $v'' = 29$ (classical outer turning point $\sim 8.6 \text{ \AA}$). We found that it can, in fact, reproduced the experimental data with a standard deviation of 0.1 cm^{-1} (to be compared to the stated standard deviation of 0.031 cm^{-1}).

2.5 Predictions

This analysis allows us to make reliable prediction about collision phenomena. The precision of the possible predictions relies on the accurately calculated value of the C_6 van der Waals coefficient and on our choice for its uncertainty. We have shown that such considerations lead to a relatively small interval (0.09 cm^{-1}) for the prediction of the dissociation energy from 1101.99 cm^{-1} to 1102.17 cm^{-1} .

In order to show the consistency of the entire PEC it is interesting to compare the observations - not used in the procedure to determine the potential -

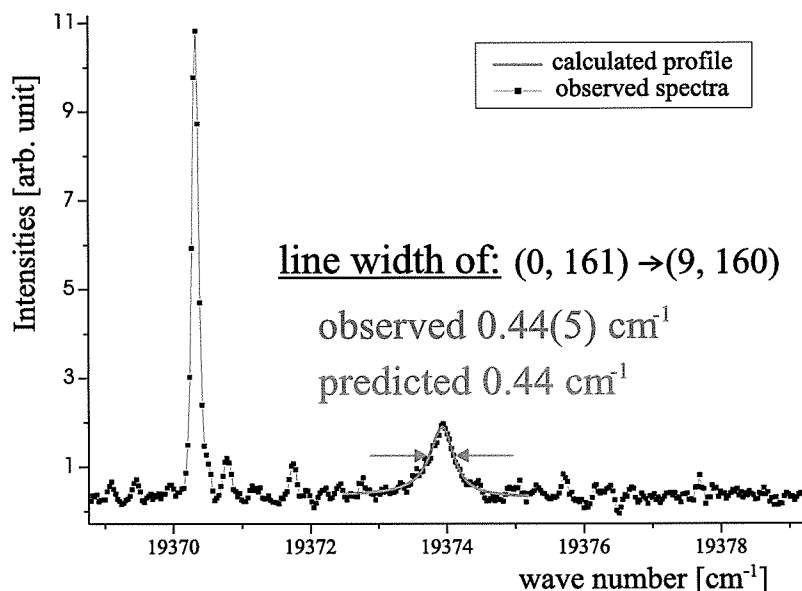


Figure 2.13: Shape resonance observed for the transition involving the ground state ($v''=9, J''=160$) level. In blue is presented the calculated profile.

to their predictions. For this purpose, we can check if agreements, for example, between calculated and observed profiles of shape resonances are found. The profiles can be calculated by different methods. We choose simply to calculate the overlap between the wave functions of the excited level of the B state⁷ and the wave function of the dissociating ground state level of the considered broadened transition line. The dipole interaction was supposed to be constant. Inhomogeneous broadening from Doppler effect was neglected due to its much smaller magnitude compared to the dissociation broadening of the observed resonances and also because it is of the same order of magnitude as the experimental uncertainty of the width of the resonances. We can see on the figure 2.13 the observed shape resonance concerning the transition $(0, 161) \rightarrow (9, 160)$ together with the calculated profile. Both profiles agree very well, see in Fig. 2.13. Such agreement has been obtained, as well, for two other observed resonances. The calculated and observed widths are given in table 2.5. It is interesting to mention that, due to the shallow potential, the nine levels of the potential well with rotation $J''=160$ lie above the dissociation threshold. All these levels present then a broadening due to their non-zero probability to dissociate. Of course, only the ones close to the top of the centrifugal barrier have a significant broadening and only $v''=9$

⁷The RKR potential of the B state from Vidal has been used for these calculations

transitions	observed line widths [cm ⁻¹]	calculated line widths [cm ⁻¹]
(0, 161) → (9, 160)	0.44(5)	0.440
(0, 101) → (21, 102)	0.18(2)	0.185
(16, 121) → (17, 122)	0.25(9)	0.301

Table 2.3: Observed and calculated line width of shape resonances.

have a large enough line width to be observed in our LIF experiment.

Another prediction that can be made is the determination of the s-wave scattering length a . For all constructed potentials, we have calculated the corresponding value of the scattering length. We have used a program developed in our group which calculates the phase shift $\delta(k)$ induced to the wave function by the interaction of the two colliding atoms. The phase shift is related to the scattering length by the relation:

$$a = \lim_{k \rightarrow 0} \left[-\frac{1}{k} \tan(\delta(k)) \right] \quad (2.18)$$

where $E = \hbar^2 k^2 / 2\mu$ is the relative kinetic energy of the colliding atoms.

The value of the calculated scattering length ranges from 112 a_0 to 850 a_0 . The highest limit happens for the lowest values of the dissociation energy $D_e^X = 1101.99 \text{cm}^{-1}$. Decreasing the value of the dissociation energy will result in a fast raising of the value of a which can then pass the infinity⁸ and become negative. As we have discussed previously, the lower boundary for $D_e^X = 1101.99 \text{cm}^{-1}$ is a limitation coming from the experimental data. Decreasing further the value of D_e^X beyond this limit would lead to unacceptable contradiction with the observation. Therefore we believe that if the deviation of C_6 from the theoretical prediction does not exceed the selected 5%, the given interval for the scattering length is reliable.

2.6 Achievements

We employed the laser-induced fluorescence spectroscopy combined with a high resolution Fourier transform interferometry to observe transitions from the B state to the ground state. We collected a large amount of information about the position of rovibrational levels of the ground state. This

⁸When the scattering length becomes infinite from the positive side the potential well loses one bound level.

field of data allowed us to determine potential energy curves of the ground state, from the smallest "observed" turning point ($\sim 3.63 \text{ \AA}$) to the largest "observed" one ($\sim 13.1 \text{ \AA}$), using two different representations. These potentials describe the experimental data within the experimental uncertainty. The standard deviation of the differences between levels calculated by both representations equals 0.0023 cm^{-1} , which is much smaller than the experimental uncertainty.

Then, the reliability of the potentials was discussed. We have seen that, despite the fact we have experimental data up to 13.1 \AA , the potentials from both representations are identical and unique only up to 10 \AA . It was explained by the decreasing number of observed data whose turning points lie beyond 10 \AA (18 levels). We have seen that it generates ambiguities for extending the potential curve to larger internuclear distances.

Two important facts were found during our analysis which permitted us to remove this problem. First, we discovered that the highest observed levels can be described accurately by a pure long-range model, containing the van der Waal terms (C_6, C_8, C_{10}) and the dissociation energy D_e . Second, this physical model can be connected to the part of the potential curve which is reliably determined keeping a correct representation of the observed levels. Consequently, we obtained a unique potential curve which represents accurately the observations and is reliable for the whole range of internuclear separations from short internuclear separations to infinite separations.

Having ensured the potential energy curve to be reliable we analyzed how precise the long range coefficient could be determined. An accurate determination of the contributions of each dispersion term was not possible due to the limited set of near asymptote levels. Therefore we relied on the theoretical prediction of the leading term C_6 to fix the possible variation of the other long-range coefficients. To achieve that, we have adjusted all parameters of the potential in order to construct all possible potentials which represent equally well our observations, which have smooth connections between the intermediate and the long part, and which have a value of C_6 within $\pm 5\%$ around its theoretical value taken from [Porsev S. G. and Derevianko A., 2002]. This procedure gave a family of reliable potentials and a well determined dissociation energy: $D_e = 1102.08 \pm 0.09 \text{ cm}^{-1}$. From each potential belonging to the so defined family we have calculated the scattering length leading to an interval of positive values ranging from $112 a_0$ to $850 a_0$ indicating that a Bose-Einstein condensate with calcium atoms would be stable. To improve the determination of the long-range coefficients and base the analysis solely on experimental data, we need to observe more high lying levels. The observation of higher levels would require longer time of observation and thus higher stability for the recording by Fourier transform spectroscopy.

The desired stability was not achievable with the heat pipe oven apparatus so we decided to perform another spectroscopy. We used the technique called the filtered laser excitation (FLE). I will explain in the next section this method and the results we achieved.

2.7 Filtered Laser Excitation

In the precedent section, I showed that vibrational progressions up to $v''=35$ have been observed for $J''=20$ and 22 using LIF technique where the fluorescence was recorded with a Fourier transform interferometer. To observe these levels a powerful laser and a narrow interference filter were used in order to achieve a sufficient signal-to-noise ratio. Nevertheless, we reached somehow the limits of what we could detect and we have not observed higher lying rovibrational levels. The limit can be understood by calling upon the following reasons. The noise amplitude at a given wave length is proportional to the total light power falling into the detected spectral window. We understand that all the light reaching the detector will contribute to the amplitude of the noise. The narrower the filter centered at the interesting frequency, the better the signal-to-noise ratio. The availability of central positions and band pass widths of the filters are rather restricted, leading to a first limitation of the Fourier transform interferometry. The other well know technique to improve the signal to noise ratio is to average several spectra since the SNR depends on the number of scans N as $(N)^{1/2}$. The typical number of scans we used is 20, each lasting approximately 1 minute. To improve the signal-to-noise ratio by a factor of two only, one hour and 20 minutes of time of recording is necessary. Furthermore, this assumption relies on the achievable improvement of the long term stability of the conditions in the heat pipe oven. Improving significantly the signal-to-noise ratio (more than 2 times) would demand long term stability which was not achievable with the present apparatus.

Thus, the observation of the levels closer to the asymptotic limit requires another spectroscopic technique involving other means of detection. We chose to perform a selective detection on laser fluorescence excitation. This technique is called the Filtered Laser Excitation [Linton C., 1978]. I will explain how we have adapted this methods.

The most favorable Franck-Condon factors to observe the transitions to the levels near asymptote of the $X^1\Sigma_g^+$ are with the vibrational level $v'=2$ of the B state (see graph 2.4 page 24). At the temperatures of the oven, all vibration levels of the ground state are thermally populated. It is then possible to observe absorption spectra directly from these high lying lev-

els of the ground state. Each resonance encountered by scanning the laser around these transitions will result in a fluorescence progression along the ground state levels. The detection of the total fluorescence as function of the laser frequency will lead to a very congested excitation spectrum, because the density of levels is high approaching the asymptotic limit. Nevertheless, the position of the fluorescence transitions towards the lower vibration levels within each progression is different and well separated from each other. By centering a very narrow filter on one line of a selected progression we can greatly simplify the excitation spectra since only encountered resonances which have a fluorescence transition that lies in the chosen window will be detected while scanning the laser.

A 1 m monochromator (GCA/McPherson Instruments) is employed as the narrow band pass filter. The typically used window width was 2 cm^{-1} , sufficient to have good resolution. The window of the monochromator is set on the strongest fluorescence line ($v''=2, J''=J'-1$) of a selected progression ($v'=2, J'$) when exciting one transition of this progression. Then the laser, a Coherent CR 699-21 frequency stabilized single mode ring dye laser operated with Coumarin 6 pumped by the blue line of an argon ion laser ($\approx 7\text{W}$) which (the dye laser) have a short term stability better than 1 MHz, scans the frequencies around 550 nm of the transitions from the near asymptote levels to the selected $v'=2$ level. A broad band photomultiplier (Hamamatsu R928) detects the fluorescence transmitted through the selected band of the monochromator. Although many other transitions of the B-X system contribute to the absorption spectrum of the calcium dimer in the scanned spectral region, only excitations, which decay into the selected frequency window, are detected. Thus, this selective technique provides greatly simplified excitation spectra in a region where the weak transitions from asymptotic levels are completely overlapped by much stronger transitions and leads also to a significant improvement of the signal-to-noise ratio due to the important reduction of the band width of detection.

A drawing of the experimental setup is presented in figure 2.14. While scanning the laser, the spectra are recorded together with the frequency comb of a temperature stabilized Fabry-Perot cavity of free spectral range $149.75(1)$ MHz to have a relative calibration of the FLE line positions. The absolute line position is obtained using a laser normalized absorption spectrum of iodine vapor at room temperature. The calibration of the I_2 spectra is realized using the IodineSpec calculating software developed in our group [IodineSpec,] which can predict the position of the lines better than 3 MHz in the considered spectral region. The laser power is recorded for normalizing the calcium fluorescence to minimize the influence of laser power fluctuations. To improve further the SNR the FLE spectra of selected J' were recorded several

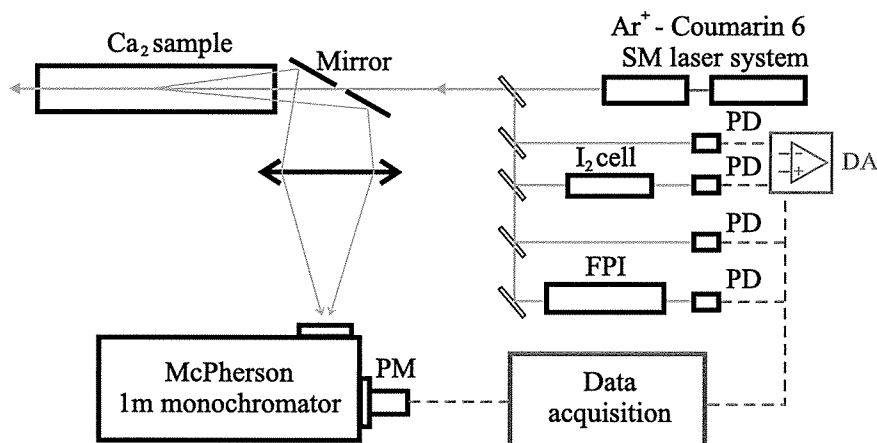


Figure 2.14: Experimental setup. DA: differential amplifier, FPI: Fabry-Perot interferometer, PM: photomultiplier

times and averaged after calibration. The different calibrations were realized using a numerical program developed by St. Falke [Falke St.,] which greatly simplifies and speeds up the procedure. The typical observed line width corresponds to the Doppler broadening ($\sim 0.05 \text{ cm}^{-1}$). In addition to the FLE lines, as it was mentioned before, the discrete fluorescence is accompanied by a strong background emission, slowly varying with the frequency, due to bound-bound-free and free-bound-free molecular transitions. This slowly varying background, intensity of which is comparable to the strongest lines, is mainly responsible for the noise in the spectra. This noise has random amplitude varying much faster in frequency than the line amplitude contributing thus weakly to the uncertainty of the determination of the line positions. We have no instrumental broadening, therefore, the main contributions to the uncertainty come from the precision with which we can determine the center of the Doppler profile of the Ca_2 lines and the profile of the I_2 lines. The estimated experimental uncertainty of the absolute position has been set to 0.006 cm^{-1} (150 MHz) for the strongest lines ($\text{SNR} > 5$). For the weakest lines, the SNR has been included in the estimation increasing progressively the uncertainty up to 0.008 cm^{-1} for a signal-to-noise ratio of 2.

Two excitation spectra are presented on figure 2.15 from the several recorded ones. The spectral window of the monochromator was set to the frequency of the $(2, 9) \rightarrow (2, 8)$ transition or to the frequency of the $(2, 15) \rightarrow (2, 14)$ transition respectively. On the graphs, one can follow the excitations up to $v'' = 37$ for $J'' = 14$ and 16 and up to $v'' = 38$ for $J'' = 6, 8$ and 10. The recorded experimental trace (black lines) contains some gaps, which were not

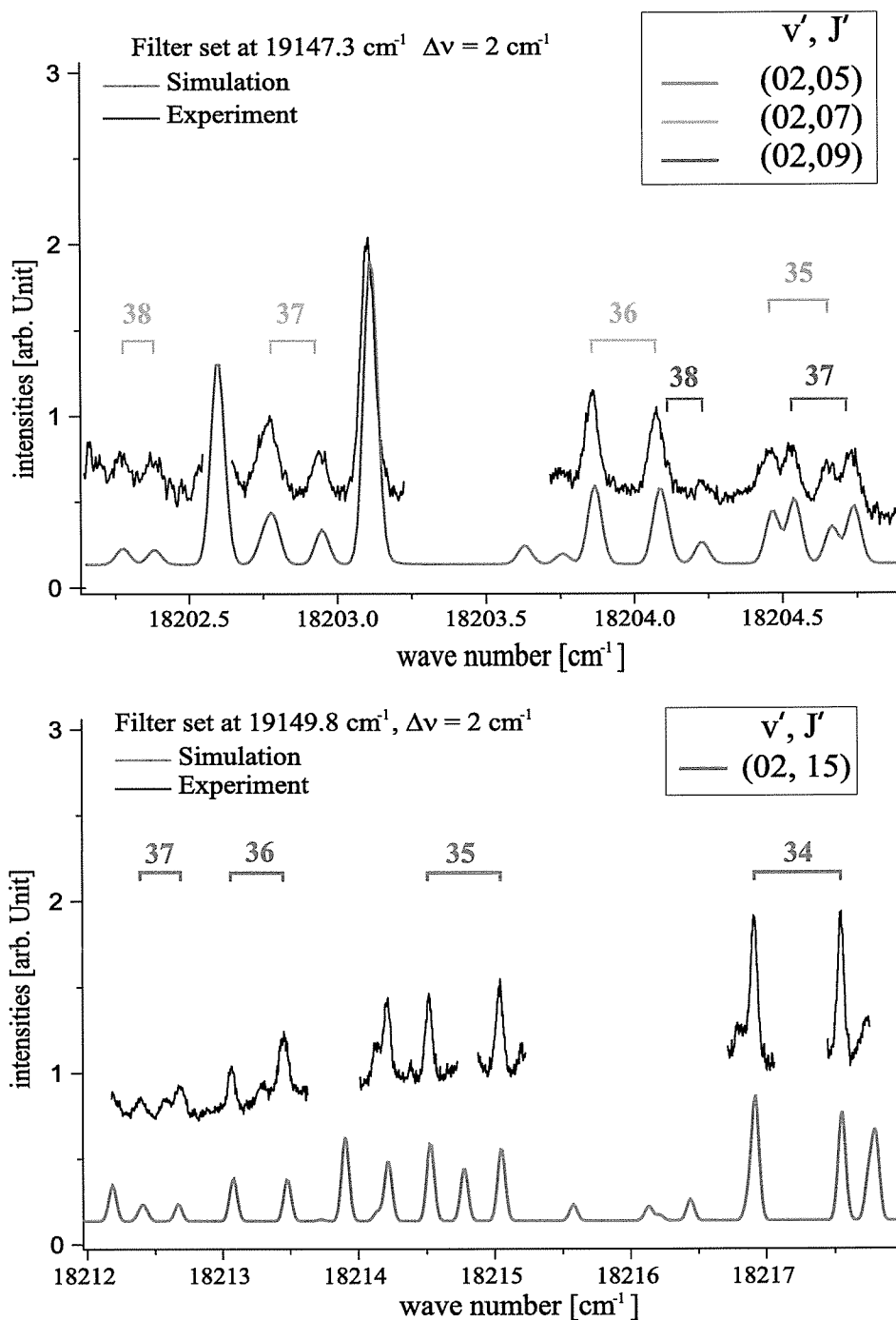


Figure 2.15: Portion of filter laser excitation spectra. Frequency position and width of the spectral windows of observation is given at the top left part. Only transitions from ground state levels $v'' \geq 34$ are labeled. The blue curve is the simulated spectra calculated with the previous ground state potential.

scanned, corresponding to positions of excited transitions whose fluorescence occasionally falls into the selected window but does not involve asymptotic levels. On the graph a simulation of FLE lines is presented in addition. The simulated spectra were calculated by determining all the transitions of the B-X system which have their frequency inside the monochromator spectral window. From them, only the position of transitions involving a B state level, which can be excited by the laser at a frequency within the scanned range, were selected. The excited line profiles and relative intensities were determined assuming a Doppler profile and considering a population of the ground state levels at $T = 1223$ K, Franck-Condon factors, and a constant dipole moment. Calculations were performed using the IPA potential of the B state published in [Vidal C. R., 1980] and using the potential derived previously using the LIF data set, which was reaching only $v'' = 35$. We see that the agreement with the observed positions of the recorded transitions, which have v'' higher than 35 is very good. The relative intensities and profiles show good agreements as well. Some differences still exist in the absolute position of the lines which is attributed to the limited accuracy of the B state IPA potential (~ 0.05 cm $^{-1}$). The relative position of lines within a progression (with a common upper level) is fairly good (better than 0.02 cm $^{-1}$). This proves the reliability of the previously derived ground state potential and the quality of the predictions that could be realized with it.

We have observed, using the filtered laser excitation technique, transitions from 44 ground state levels, 25 of which have a higher vibration quantum number $v'' \geq 35$ than the ones observed in the LIF experiments. The levels nearest to the asymptote are $v'' = 38$ with $J'' = 6, 8$ and 10 levels. The FLE data field is presented figure 2.16 in full black dots.

LIF complementary data In the section 2.2, I reported the experiment realized using the LIF technique. We were not using all possible lines of an argon ion laser but only the three following lines: 514 nm, 496 nm and 476 nm. We have enriched our LIF data set with the progressions obtained with the other lines 502 nm, 488 nm and 458 nm, with an Ar $^+$ laser from Spectra Physics (beamlock 2060). Most of the transitions, which have been already reported in [Vidal C. R., 1980], were observed here as well.

In a first step, the experimental uncertainty was estimated as in the previous LIF experiment. A reasonable estimation of the uncertainty normally gives an error in the order of one tenth of the line width for a good SNR. The choice of an uncertainty of 0.01 cm $^{-1}$ for a line having a width of 0.07 cm $^{-1}$, shows an overestimation. In addition, the value of the normalized standard deviation $\bar{\sigma} \approx 0.45$ resulting from the fitting procedure confirms the overestimation of

the magnitude of the experimental errors. A simple simulation of the possible error to find the line maximum introduced by the number of points falling into a line profile and by the influence of the noise shows that an uncertainty of 0.006 cm^{-1} is more realistic. Accordingly, we changed the errors of all the LIF frequencies by a factor 0.6.

Summary of observations All collected data from the two spectroscopic techniques, the LIF and the FLE, cover a range of rotational quantum numbers from $J''=4$ to 164, and extend from $v''=0$ to 38 for the vibration at ones. A total of 3580 transitions were observed involving 924 ground state levels. The total field of quantum number v'' and J'' is presented on the figure 2.16.

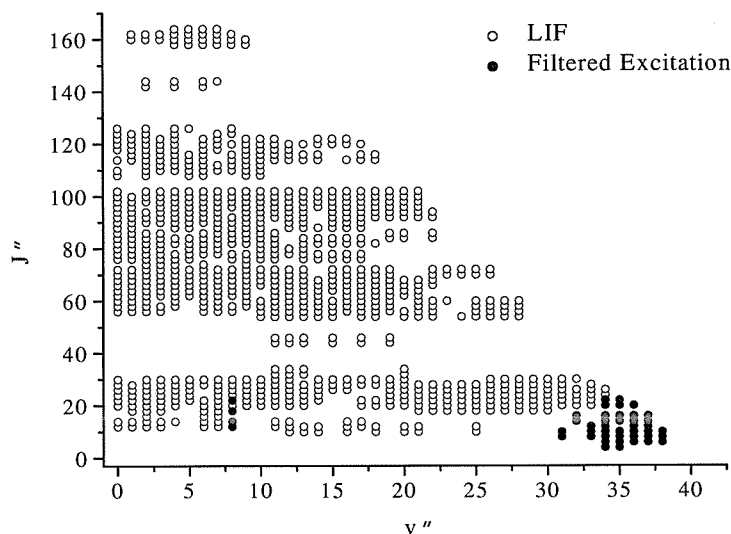


Figure 2.16: Data field summarizing the range of quantum number of the levels observed with the LIF and FLE spectroscopies

This data set will be used to improve the shape of the potential in the long-range region. We have made some changes in the procedure of fitting the data for the point-wise representation that the dispersion coefficients C_n can be adjusted as well with this method. I will present the changes we implemented. Then I will talk of the improvement on the shape of potential.

2.8 The interaction potential

The set of differences was constructed in the same way as previously within progressions with a common level of the B state. Only crossed differences were calculated. Because we only use the relative positions of the levels within observed progression by construction of differences, and because the FLE data contain only very few transitions with lower vibrational levels ($v'' \leq 32$), it could result that the relative position of the long range part of the potential obtained by the fit of the FLE data compared to the position of the lower part of the potential cannot be determined. To solve this problem, we have generated transitions extending from $v'' = 0$ to the low v'' of FLE data for each FLE progression, using presently the potential of the $X^1\Sigma_g^+$ state. Then, differences were calculated between generated and FLE transitions. Since the calculated low levels lie in the region of the potential, which is very well characterized, they have virtually no influence in the quality of the fit. We have constructed a total of 8490 differences from the 3624 observed and generated transitions from which we will fit the potential. As it was mentioned, the intermediate region of the potential is already very well defined due to the large amount of data. So, it is mainly the long range part, which will be improved.

2.8.1 Improvement of the potential

I will present in this section the slight changes introduced to fit the new data set. We have used the two representations for the determination of the potential. Both representations were defined in section 2.3.1.

The main changes were introduced to the point-wise representation and it concerns the long range region. The correction to the potential in the short and intermediate regions of the potential (from $R_{min} \approx 3.09\text{\AA}$ to R_{out}) is still represented by a set of points $\{c_i\}$ connected by modified cubic spline function, equation 2.19. This equation is now written with $f_i(R) = S_i(R)$.

$$\delta V(R) = \sum_{i=0}^n c_i S_i(R) \quad (2.19)$$

We want to include the long range model into the fitting routine. The C_n and D_e coefficients will be treated like the $\{c_i\}$ parameters. We will minimize the differences between $\Delta E_{v_1 J_1, v_2 J_2}^{obs}$ and the differences calculated with the corrected potential. The corrections to the long-range part are now included as:

$$\delta V(R) = \delta D_e - \frac{\delta C_6}{R^6} - \frac{\delta C_8}{R^8} - \frac{\delta C_{10}}{R^{10}}, \quad \text{for } R \geq R_{out} \quad , \quad (2.20)$$

where δD_e and the δC_n are the correction to the initial long-range parameters. According to the perturbation approach in section 2.3.1 the corrections to the energy differences due to δV can be written as:

$$\begin{aligned} \delta(\Delta E_{v_1 J_1, v_2 J_2}^{obs}) &= \sum_{i=1}^N \delta c_i (K_i^{v_1 J_1} - K_i^{v_2 J_2}) - \sum_{n=6,8,10} \delta C_n (L_n^{v_1 J_1} - L_n^{v_2 J_2}), \\ &+ \delta D_e (L_0^{v_1 J_1} - L_0^{v_2 J_2}) \end{aligned} \quad (2.21)$$

where

$$K_i^{vJ} = \int_{R_{min}}^{R_{out}} \Psi_{vJ}^2(\mathbf{R}) S_i(\mathbf{R}) d\mathbf{R} \quad (2.22)$$

$$L_n^{vJ} = \int_{R_{out}}^{\infty} \Psi_{vJ}^2(\mathbf{R}) \mathbf{R}^{-n} d\mathbf{R} \quad (2.23)$$

are the corresponding mean values of $S_i(\mathbf{R})$ and \mathbf{R}^{-n} calculated with the wave function $\langle \mathbf{R} | \chi_{vJ}^0 \rangle = \Psi_{vJ}(\mathbf{R})$ of the levels forming the differences. The connecting point R_{out} is chosen in the following way. Initially, the data are fitted using the point-wise form up to 13 Å. Secondly, this point-wise potential is stopped at $R_{out} = 9.5$ Å and the long range parameters δC_n and δD_e are adjusted on the data, beyond R_{out} . The continuity of the potential is still ensured by varying slightly the connecting point R_{out} and to a smaller extend the parameters C_{10} .

The derived potential using the analytic representation describes the total set of differences between observed spectral lines with a standard deviation $\sigma = 0.0064 \text{ cm}^{-1}$ and a normalized standard deviation $\bar{\sigma} = 0.69$. We can estimate the standard deviation for the near-asymptote levels using only differences involving at least one level with $v'' \geq 35$. We have obtained $\sigma_{v'' \geq 35} = 0.0092 \text{ cm}^{-1}$ and $\bar{\sigma}_{v'' \geq 35} = 0.92$. For the point-wise representation, we have $\sigma = 0.0068 \text{ cm}^{-1}$ and $\bar{\sigma} = 0.74$ for all the data and $\sigma_{v'' \geq 35} = 0.0092 \text{ cm}^{-1}$ and $\bar{\sigma}_{v'' \geq 35} = 0.89$ for the levels close to the asymptote. The standard deviation obtained using the analytic representation is satisfactory. The analytical potential gives a slightly better representation. The standard deviation of the differences between levels calculated with the two representations is 0.0023 cm^{-1} . Since this value is smaller than the mean experimental uncertainty, it is not necessary to try to obtain exactly the same quality of representation by both methods. The parameters of the so-called best potentials are listed in the appendix A for both representations.

The value of the dissociation energy D_0 with respect to $v'' = 0, J'' = 0$ is given in these tables. It should be clear that D_0 is the good parameter for

comparing the potential depth instead of D_e . Not only because, as it was mentioned, D_0 is the real observable, but because D_e is subject to the variation of the position of the bottom of the potential. Calling upon the WKB semi-classical view, we can say that different shapes of the potential below ($v = 0, J = 0$) can lead to the same accumulated phase of $\pi/2$ for the lowest level. The shape of the potential below ($v = 0, J = 0$) is dependent of the choice of representation of the potential. No physical inputs are known to restricting the possible shapes. So a different bottom form leads to a different energy position of ($v = 0, J = 0$) with respect to the minimum. The same difference echoes on every level of the potential and the dissociation energy. The relative position of these energies will be given with respect to ($v = 0, J = 0$) in the rest of the manuscript to avoid the addition of non-physical uncertainty on the determined quantities. It is then not surprising that the values of D_e are different for the two representations, namely they differ by 0.014 cm^{-1} . On the other hand, the very good agreement (within the experimental uncertainty) between the values of D_0 (they differ by 0.002 cm^{-1}) speaks again about the consistency of the two determinations.

A comparison with the same parameters as from section 2.4 shows, as well, a very good agreement. It tells that the potential derived using a theoretical value for C_6 with an uncertainty interval of 5% and the newly determined potential with more data are consistent.

Chapter 3

Precision of the long-range parameters

3.1 Introduction

3.1.1 Motivations

In the previous chapter, I presented the spectroscopic study which allowed us to collect rovibrational levels up to very close to the asymptote (outer turning point up to 13.1 Å). From the dense and large field of data we have derived a potential which describe the different observations within their experimental uncertainties. We have ensure that the potential is reliable for the whole range of internuclear distances.

Our interest is to make predictions of molecular or scattering properties. The reliability of the possible predictions is then of great importance. We need for that to establish the relation between the experimental data including their uncertainties and the accuracy of quantities we want to predict. We want to see how our measurement errors propagate through the determination of the PEC to the quantities we are interested to calculate. For these reasons, we need to ask what are the variations of the model parameters around the fitted ones, which are still in agreement with the experimental data. In the precedent analysis we have answer this question by investigating the variation of the goodness-of-fit with the long-range parameters. Though, the method give reasonable boundaries for the values of the LR coefficients, the obtained intervals can not be considered as definitive and satisfactory estimations of their uncertainties. We rather want to establish a confidence region for all the potential parameters including the LR coefficients. Having found this region, it is straightforward to predict the value of interesting quantities and to address their confidence intervals.

3.1.2 How to determine the confidence interval?

For the non-linear fitting procedure one can try to use the error surface in the parameter space to delimit a contour plot, which will correspond to a certain confidence limit. We face here a problem, since it is not clear to which confidence level the choice of the contour plots does correspond or equivalently the choice of an interval of variation $\Delta\bar{\sigma}^2$ for the value of $\bar{\sigma}_{min}^2$ because of the non-linear relation between observables and model parameters. Thus there is an ambiguity in the statistical interpretation of error limits of the fitted parameters determined by contours plots.

In the linear least squares fitting, the matrix of variances and covariances obtained from the linear system of equations can be used to determine the confidence limits of the model parameters. But one is allowed to use this matrix only when the fitted data are independent and their errors follow a normal distribution. This is not true in our case since we are fitting differences between observed transitions, thus the quantities which enter the fit are dependent.

We decided to use another method to get the confidence region of our model parameters. We employed a Monte Carlo simulation adapted to the case of molecular potentials for determining the reliability of the parameters of the potential model and in particular the long-range coefficients of the dispersion forces. One main advantage is that the procedure doesn't rely on the assumption that the data are uncorrelated. The Monte Carlo simulation provides in a same time quantitative estimations of confidence limits of the fitted parameters in a precise way and gives the possibility to present them in a very visual and simple form. It also answers to our former question by setting confidence intervals for predicted properties directly drawn up from the experimental data.

I will now explain the Monte Carlo simulation procedure and direct the discussion to the determination of the potential-parameter confidence regions. A rather complete explanation of the Monte-Carlo simulation can be found in [Press W.H. et al., 1985].

3.2 Determination of the parameter distribution from the experiment

3.2.1 The general case

Let us consider what would be the best way to obtain the desired confidence region on our model parameters directly from an experiment. This consid-

eration will lead us to important assumptions on which the Monte Carlo simulation is based.

We can suppose that in our physical world, it exists a true set of N_p parameters for a true mathematical form, that I call c_{true} . By measuring a data set, noted $D_{(0)}$, coming along with experimental random errors, we measure actually one of the possible realizations of the true parameters. In the following, the usual procedure is to fit the parameters of the model to the measured data set employing our favorite minimization technique to obtain the corresponding set of best parameters $c_{(0)}$.

The number of possible realizations from c_{true} is infinite due to the random character of the error process coming from the measurement procedure. Each realization could have been the one measured, but happen not to be. Supposing that we could repeat many times the experiment (each independently), we would have obtained each time a different data set $D_{(i)}$ and determined for each one a different parameter set $c_{(i)}$. Collecting all the parameter sets, we would obtain the distribution of all parameters in the N_p parameter space. We should note that the actual "measured" set $c_{(0)}$ is not a particular realization of c_{true} , it is just one member of the distribution. Having this parameter distribution, or better $c_{(i)} - c_{true}$, we could derive the probability for each parameter value to be realized and we could address quantitative uncertainties on the parameters directly from the experiments.

Of course this universe of possible realizations $c_{(i)} - c_{true}$ is not accessible to us in practice, since we cannot performed our measurements with a statistically sufficient number of times, and we cannot ensure each measurement to be really independent. Furthermore c_{true} is not accessible to us! So we should find some way to approximate or simulate the distribution $c_{(i)} - c_{true}$, having only one set of measured data and one set of fitted parameters. The way is to perform a Monte Carlo simulation.

3.2.2 The Monte Carlo simulation

The determined set $c_{(0)}$ is not the true one, but let us consider, for a moment, a fictitious world in which it would be the true one. Since we tried to do our best to "measure" the model parameters, we can reasonably think that they are not too wrong, and thus this fictitious world derived from $c_{(0)}$ is not too different from the true world of c_{true} . In particular, we can assume that the form of the distribution $c_{(i)} - c_{(0)}$ is very close to $c_{(i)} - c_{true}$. We are in this way following the assumption that the random statistic does not change rapidly with c_{true} , and so $c_{(0)}$ can serve as a good substitute (figure 3.1). We are now able to calculate the distribution of $c_{(i)} - c_{(0)}$.

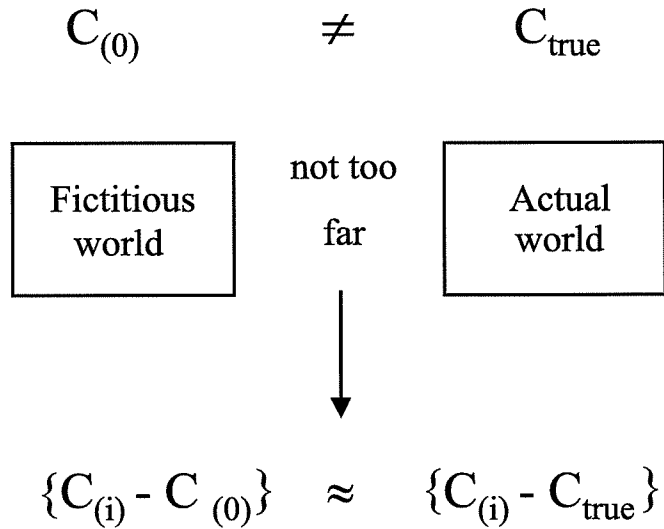


Figure 3.1: Schematic of the assumptions on which the Monte Carlo simulation is based.

Here is the way to proceed: We start with our derived potential. We simulate a set of data as our own synthetic realization applying the potential with the set of best parameters $c_{(0)}$ ¹. The simulated data are a set of transitions, which have exactly the same manifold of v , J and measurement uncertainties as the actual observed ones. To each transition frequency, a small random quantity is added, which has a normal distribution with mean value zero and a standard deviation equal to the experimental uncertainty of the transition. Then the obtained set of transitions is transformed to a set of differences $D_{(1)}^S$ in the same way we formerly done it. The synthetic set of differences is used to fit a new set of parameters $c_{(1)}$. The whole process can be repeated several times to generate different synthetic data sets $D_{(2)}^S, \dots, D_{(i)}^S$ and to obtain several parameter sets $c_{(2)}^S, \dots, c_{(i)}^S$. If sufficient simulations are performed we are able to map out the probability distribution $c_{(i)}^S - c_{(0)}$ in the N_p parameter space. A flow chart of a Monte Carlo simulation is presented figure 3.2.

¹All fitted potential parameters are meant by $c_{(0)}$ so including the long-range ones.

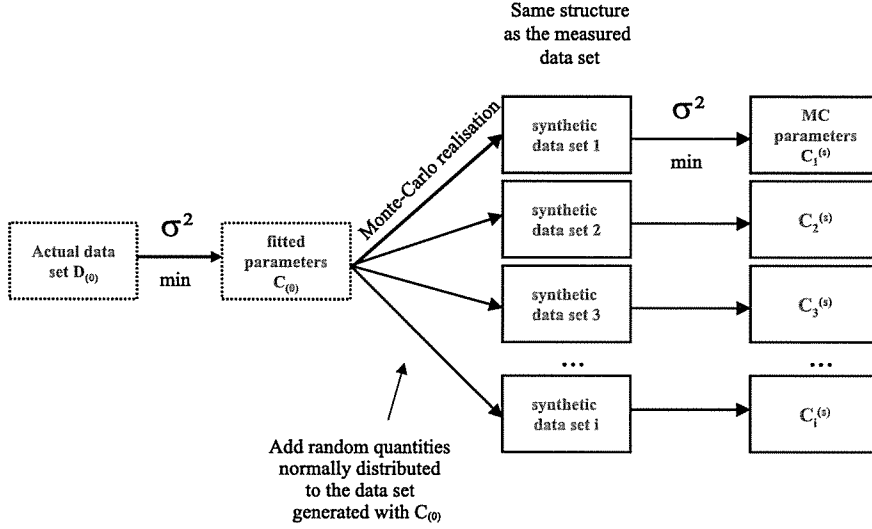


Figure 3.2: Principle of the Monte-Carlo simulation of an experiment.

3.2.3 Implementation of the Monte Carlo simulation

In order to apply the Monte-Carlo simulation we use only the iterative linear fitting procedure with the point-wise representation of the potential. For each iteration of the simulation, the best parameters corresponding to the simulated synthetic data set should be found. From the experience with the non-linear fitting procedure of the analytic potential we know that a fairly large number of fitting steps could be necessary to ensure convergence in the fit leading to a very time consuming process in total. In contrary, the linear fitting converge in few iteration steps and for an initial set of parameters not too far from the best ones only one step is often necessary. This situation is usually encountered since we are exploring the parameter space in the near vicinity of the "measured" parameters. The use of the IPA method provides immediately the distribution of $c_{(i)}^S - c_{(0)}$ since the procedure seeks directly correction $\delta c_i = c_{(i)}^S - c_{(0)}$ if at each iteration of MC simulation the fit is initiated with $c_{(0)}$ as first guess.

We have seen previously that the shape of the potential is very well fixed within the experimental uncertainty by the large amount of data in the region from 3.5 Å to 10 Å and doesn't depend on the choice of representation. By connecting the long range part of the potential at 9.5 Å, i.e within the well defined region, we expect that the performed analysis on the whole potential be almost independent of the choice of functional form modelling the potential in this region. The residual variations within the experimental

uncertainty of this region of the potential are included in the Monte-Carlo simulation since the whole set of parameters are adjusted at each iteration and not only the long range ones ($\delta c_i, \delta D_e, \delta C_n$). In the following part we will present the distribution of parameters and draw confidence region of their values. The dissociation energy will be given with respect to ($v''=0, J''=0$) not only, like we said it, because the observable is D_0 and not D_e but also because the precision reached with the new data set (with FLE) for the dissociation energy is in the order of $\pm 0.01 \text{ cm}^{-1}$ (see next section), which is of the same magnitude as the uncertainty of the minimum position taken with respect to ($v''=0, J''=0$).

3.3 Results: Confidence limits on the long-range coefficients

3.3.1 From the distribution to the confidence limits

The distribution of the potential parameters² were determined by performing $N_s = 3000$ simulations allowing a statistical treatment, and to set the probability distribution of the $N_p = 52$ parameters of the potential. The dimension N_p of the parameters space prevent from a detailed presentation of the results. We have compared the distribution of the LR coefficients solely obtained by fitting with and without the c_i parameters. No significant change³ was detected on their distribution confirming the statement that the data imposed strong constraints on the intermediate part of the potential. The distribution of the LR coefficients wasn't affected by the number of points c_i as well (as long as the fit itself is not influenced) confirming that the choice of representation for this region has weak influence on the long-range parameters distribution. This allows us to work only in the sub-space (C_n, D_0) and to present the result only for the long-range coefficients.

The confidence region is a domain of N_p dimensions ($N_p = 4$, now), centered on the best set parameters point c_0 , which contains a large percentage of the parameters probability distribution. The percentage is called the confidence level and some value are customary in physics, like 68.3%, 90%, 95.4%⁴ and so on. Since our experimental uncertainties are supposed to follow a normal distribution, the correct shape of the confidence region should be a N_p

²We should understand parameters as the corrections to them, namely $\delta c_i, \delta D_0, \{\delta C_n\}$.

³This is true while we use D_0 and not D_e .

⁴These values of the confidence level come from a normal distribution. The MC simulation can be performed in the case of non-normal distributions and these choices of values are clearly customary

dimension ellipsoid. The contour of the confidence region at a certain confidence level is called the confidence limit (CL). The ellipsoid should follow the shape or orientation of the distribution. So the first step is to find the correct axis of the ellipsoid. When the axes are found the equation for the ellipsoid in this frame follow the relation:

$$\sum_i^{N_s} \frac{(\delta c_i - \delta c_0)^2}{l_i^2} = R^2 \quad (l_i > 0 \forall i), \quad (3.1)$$

where the l_i keep the ratio of the length of the ellipsoid axis constant and R increase the volume of the ellipsoid. In practice the distribution is centered around zero by subtracting its mean value. Then the distribution is normalized to have a distribution width very closed to 1 by dividing each value of the parameters ($\delta C_n, \delta D_0$) by the variance of its distribution. Afterwards, we rotate the distribution to have the axis of the ellipse on the parameter axis and to apply directly eq. (3.1). Then, we count how many parameters are contained within the ellipsoid for the value of R^2 . The value of R is increased until the number of counted parameters reaches the selected confidence level. In this way, we find the confidence region for different choices of confidence levels. Then the whole distribution is rotated back, rescaled and center on the best parameters in the 4 dimension sub-space (D_0, C_6, C_8, C_{10}). The distribution is centered around the best set of parameters since the basic idea is that the confidence region should inspire confidence on the "measured" set of parameters, the so-called best parameters. The ellipsoid contour of the confidence region and the full distribution is projected onto a 2D parameters axis in order to be presented. Note that the confidence limit is determined in the four dimension parameter space and is projected afterwards. Performing firstly the projection and then counting the number of parameters into an ellipse up to obtain 68.3% of them would lead to a wrong statement. In this procedure we would count parameters lying outside the 4D confidence region, which would be, by projection, included in the 2D region. It would lead to a smaller and thus incorrect confidence limit.

3.3.2 Meaning of the confidence limits

Let us come back to the important statement on which the Monte-Carlo is based (fig: 3.1) to clarify the meaning of the confidence region. The following sentence is sometimes encountered in the literature: "There is a 68.3% chance that the true parameter values fall within the 68.3% confidence region around the measured value". It is not correct. The statement should be: If we center the 68.3% confidence region around all possible measured parameters (not the simulated) 68.3% of them will contain the true parameters. Now

following the assumption that the measured parameters set is very closed to the true set, then the area of overlap between the 68.3% confidence region around all possible measurements of the parameters should be nearly the same as the confidence region around the actual measured set. This assumption is then important to be able to state that there is a 68.3% chance that the confidence region contains the true set of parameters. Another wrong statement encountered sometimes in the literature, which found its origin in the somewhat not intuitive definition of the Monte-Carlo approach, is the following: "There is 68.3% probability that the value of C_6 lies inside the limit of the confidence region". In reality it is possible to speak only about the probability of an experimental outcome, and not about the probability of the true value of a physical quantity (like C_6). This true value is supposed to be constant.

3.3.3 Precision of the C_6, C_8, C_{10} and D_0 values

The projection onto the (D_0, C_6) sub-space of the full distribution and the projections of the 68.3% and 90% confidence limits are shown in figure 3.3. We can now set the confidence intervals for the dissociation energy D_0 and the leading dispersion term C_6 . In principle, the correct confidence limits are the boundary of the ellipse region. Therefore graphics should be presented as the results of the Monte-Carlo simulation. For a direct communication of the results one usually summarizes the graphics into confidence intervals by giving the values where tangents to the 68.3% ellipse are horizontal for the y-axis, and where they are vertical for the x-axis. This is presented in the figure 3.3. The confidence interval of D_0 is $[1069.858 \text{ cm}^{-1} - 1069.878 \text{ cm}^{-1}]$. So the uncertainty of the value of the dissociation energy is $\pm 0.01 \text{ cm}^{-1}$. The confidence interval for C_6 is $[0.969 \times 10^7 \text{ cm}^{-1} \text{ \AA}^6 - 1.036 \times 10^7 \text{ cm}^{-1} \text{ \AA}^6]$ which corresponds to a precision of 3.34%. The confidence interval for C_8 is $[3.15 \times 10^8 \text{ cm}^{-1} \text{ \AA}^8 - 4.46 \times 10^8 \text{ cm}^{-1} \text{ \AA}^8]$ which corresponds to a precision of 34% and the confidence interval for C_{10} is $[1.7 \times 10^8 \text{ cm}^{-1} \text{ \AA}^8 - 8.4 \times 10^8 \text{ cm}^{-1} \text{ \AA}^8]$ which means that C_{10} is not known with a precision better than 133%. The projection of the distribution concerning C_6 and C_8 is presented in the figure 3.4 and the confidence interval are summarize in the table 3.1. We can see on the distribution in the three plans (C_6, C_8) , (C_6, C_{10}) , (C_8, C_{10}) appendix B, that it results from the MC simulation that the coefficients C_n are strongly correlated with each other. The confidence intervals obtain meanings only in relation with the distributions and thus one must stress the correlations. In the pictures only the distributions are shown and not the 68.3% and 90% confidence limits for clarity.

The correlations show that individual contribution of the different dis-

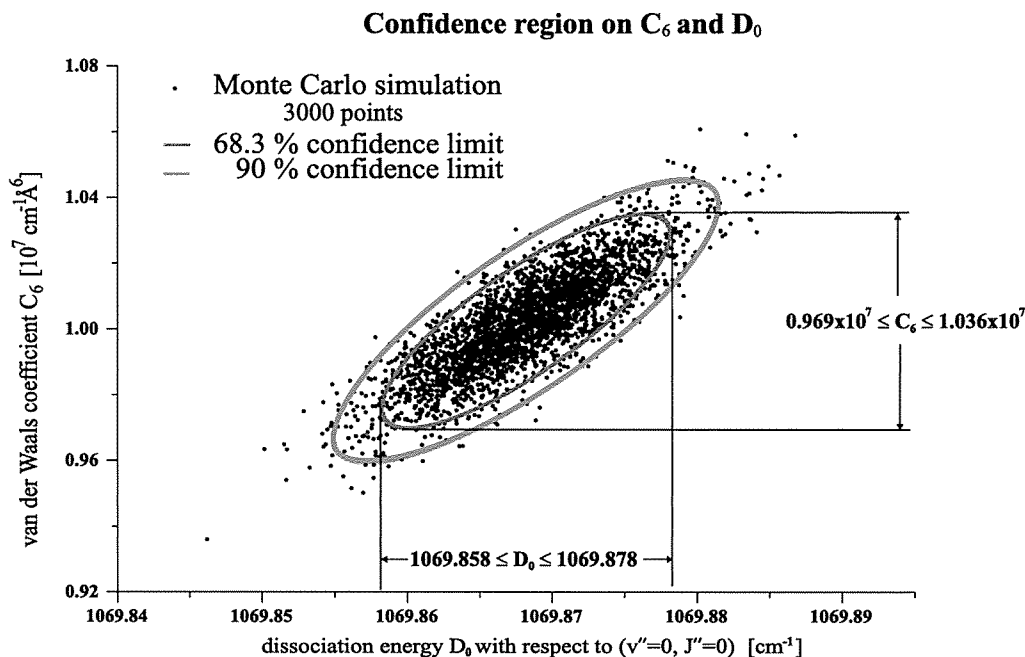


Figure 3.3: Projection on the long-range (C_6 , D_0) plane. The projection of 68.3% confidence region is delimited by the inner (red) ellipse. The outer (green) ellipse delimited the projection of the 90% confidence region. Confidence interval on C_6 and D_0 are given by the horizontal and vertical lines.

persion forces cannot be determined independently despite a rich data field for the near asymptote levels. Only two vibrational levels, namely $v''=39$ and $v''=40$, from the full vibration ladder are currently not observed. Information, in a classical view, has been obtained for fitting the long range coefficient from 9.5 Å up to 20 Å which is the outer turning point of the highest observed level $v''=38$. One would think that with the actual precision (~ 150 MHz) and the amount of observed data it should be possible to characterize each long-range coefficient. The Monte-Carlo simulation shows clearly that it is not the case.

We can see the improvement realized on the determination of the dispersion coefficients and the dissociation energy with the observation of levels below $v''=38$ by returning to our first experiment and compare the results now using the powerful tool, the Monte-Carlo simulation. With the LIF experiment the highest level was $v''=35$. We concluded at that time that we could not give a reasonable estimate for the value of the C_n coefficients without external information. Now, by using the Monte-Carlo we can be more rigorous. We can calculate and compare the parameter distribution obtained only

Table 3.1: Derived parameters of the long range expansion for the $X^1\Sigma_g^+$ state in $^{40}\text{Ca}_2$.

D_0, cm^{-1}	1069.868(10)
$C_6, 10^7 \text{cm}^{-1}\text{\AA}^6$	1.003(33)
$C_8, 10^8 \text{cm}^{-1}\text{\AA}^8$	3.15 – 4.46
$C_{10}, 10^9 \text{cm}^{-1}\text{\AA}^{10}$	1.7 – 8.4

with the LIF data with the one obtained with the addition of the FLE data. The distribution corresponding to the previous data set is generated using the precedent potential derived with this data with the theoretical value of C_6 . The errors of the LIF data are the ones before their revisions to be able to compare. In figure 3.5 page 68 both projections onto the (D_0, C_6) plane are presented. We see that the distribution for the previous data is very broad (black dots). The value of C_6 range from zero to $1.9 \times 10^7 \text{cm}^{-1} \text{\AA}^6$ and the precision on D_0 is in the order of 1cm^{-1} . This distribution is so broad that calculating the distribution with the theoretical $C_6 = 1.070 \times 10^7 \text{cm}^{-1} \text{\AA}^6$ or the new fitted one $C_6 = 1.003 \times 10^7 \text{cm}^{-1} \text{\AA}^6$ doesn't play a role. The broad distribution shrinks to the distribution in the center (the same distribution as figure 3.3) after the addition of the FLE data. In the insert a zoom of the central region is shown, where the red dots are the distribution obtained having the FLE data. Concerning the other coefficients C_8 and C_{10} their previous distributions were even extending to negative values. From this distribution it is clear now that solely from the previous data no precise determination of the dispersion coefficient was possible. What is important as well is that the recent distribution is entirely contained in the previous one showing the consistency of the analysis. The broad distribution shows the necessity at this time, for a complement of information coming from the theory side in order to better characterize the value of the dispersion coefficients and the dissociation energy. On the same graph are given the intervals coming from the choice of 5% variation of C_6 around the theoretical value. We see that the size of this interval is of the same order as the distribution of C_6 with FLE. This is simply a coincidence since it is due to the arbitrary although reasonable choice of 5%. From this point of view, it seems that the uncertainty of the long-range parameters has not been improved. We should consider that the determination on these LR coefficients is now determined

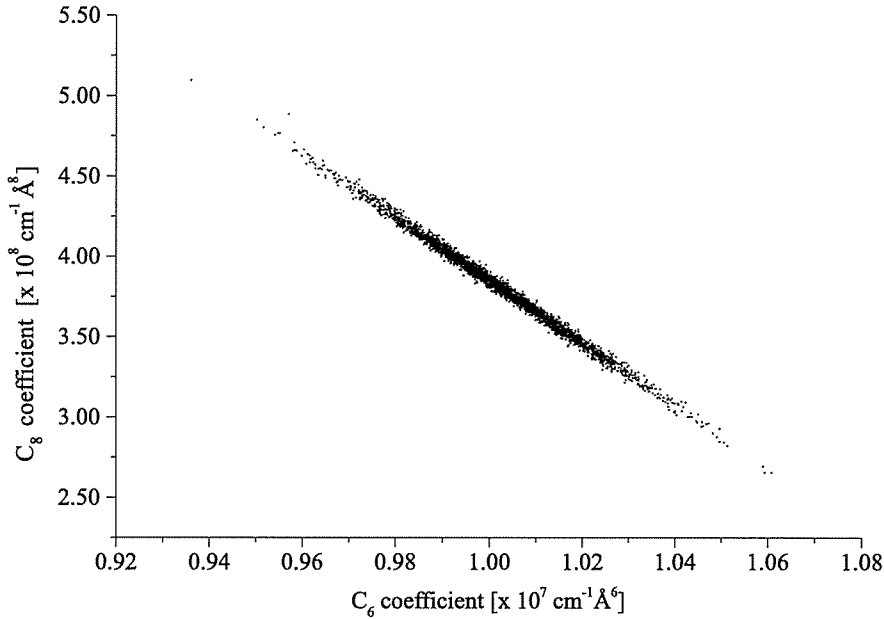


Figure 3.4: Projection on the long-range (C_6 , C_8) plane.

using only experimental data. No external information into the analysis was introduced to set the confidence region for our measured parameters. In the first analysis the intervals of possible variation of the dispersion coefficients were centered on the theoretical value of C_6 . This value differs from the value obtained by the new fit. That's why the distribution from the MC simulation is shifted compared to this interval. We will discuss in more detail this difference in the next section. The second point questions about the validity of the long range model down to 9.4 Å. The influence of other contributions was neglected since the actual model was adequate to reproduce the experimental data within their experimental uncertainty. These contributions can be readily included in our model if experimental evidences show their necessity. We know that the derived C_6 and the potential in general are always effective ones containing or compensating for weak effects not included in the model.

3.3.4 The exchange contribution

In the treatment, I have exposed so far, we have included in the long-range model only the dispersion terms with the coefficients C_6 , C_8 , C_{10} and the dissociation energy. The main influence which was neglected is the exchange energy. In order to have an estimate of the change of the value of the C_6 coefficient we have introduced in the model the term given in equation 2.17 with

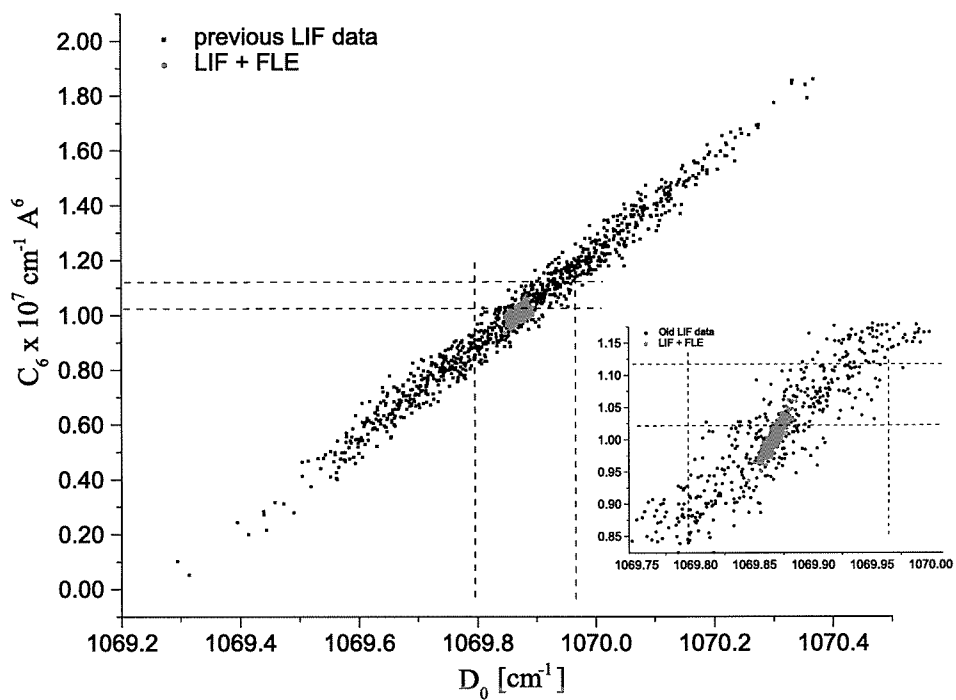


Figure 3.5: Comparison of the distributions projected onto the (D_0, C_6) plane for the LIF data (black dots) and the LIF+FLE data (red dots in the center). In the inset a zoom of the central region is given. The lines remind the selected 5% variation interval around the theoretical value of C_6 .

Table 3.2: Derived parameters of the long range expansion for the $X^1\Sigma_g^+$ state in $^{40}\text{Ca}_2$. Comparison with published calculated values.

References	$C_6 \times 10^7 \text{ cm}^{-1}\text{\AA}^6$	$C_8 \times 10^8 \text{ cm}^{-1}\text{\AA}^8$	$C_{10} \times 10^9 \text{ cm}^{-1}\text{\AA}^{10}$
This study: without exchange	0.969 – 1.036	3.15 – 4.46	1.7 – 8.4
with exchange	1.001 – 1.067	2.3 – 3.7	6.9 – 14.
[Maeder F. and Kutzelnigg, 1979]	0.9663	2.699	7.369
[Standard J.M. and Certain P.R., 1985]	1.3205–1.3639	2.564–3.360	6.689–8.616
[Stanton J.F., 1985]	0.9841		
[Mérava M. et al., 2001]	1.1205		
[Porsev S. G. and Derevianko A., 2002]			
semiempirical	1.070(7)		
ab-initio	1.045		
[Bussery-Honvault B. et al., 2003]	1.0983	3.2666	4.7350
relativistic	1.0781	3.2178	4.6265
[Moszynski R. et al., 2003]	1.0368		
[Mitroy J. and Bromley, 2003]	1.054	3.05	3.056

A , α and γ fixed to the values taken from [Radzig A.A. and Smirnov P.M., 1985, Kleinekathofer A., 1995]. The fitting procedure leads to a higher value of the coefficient C_6 to $1.034 \times 10^7 \text{ cm}^{-1} \text{\AA}^6$ and of the dissociation energy D_0 to 1069.873 cm^{-1} . Since the exchange energy is positive, in order to have the same position of the levels, the coefficient C_6 should be larger. The quality of the fit did not change by the addition of the exchange term. Performing the Monte-Carlo simulation with the new model, but keeping the coefficients of the exchange energy fixed, we have obtained the same distribution area but centered on the new values. Since the quality of the fit is not changing, we cannot conclude about the necessity to have these additional terms in our model. What we show is which influence the addition of the exchange term, in the form it was modeled, has on the overall determination.

3.3.5 Comparison with other published values of the C_n coefficients

Table 3.3.5 gathers calculated values of the dispersion coefficients C_6 , C_8 and C_{10} I found in the literature, and the ones determined in this study. All the published values of the C_6 coefficient can be found within an interval of $\pm 8\%$, except for the values given by [Standard J.M. and Certain P.R., 1985] which differ from other values by more than 27%. The most recent values

of C_6 given by [Moszynski R. et al., 2003] (which is a new calculation of C_6 by the same group compared to the one published in [Busser-Honvault B. et al., 2003]), and the value reported in [Mitroy J. and Bromley, 2003] as well as the ab-initio value given in the publication [Porsev S. G. and Derevianko A., 2002] fall inside the 68.3% confidence interval determined with the long-range model including the exchange energy. All the ab-initio values were determined with high accuracy relativistic many body calculations. Another value calculated using a semi empirical approach reported in the same article [Porsev S. G. and Derevianko A., 2002] which is published with an error bar outside the confidence interval. The confidence interval and the stated error bar overlap. This semi empirical value was calculated using the dipole matrix element of the dipole transition $^1P_1 \leftarrow ^1S_0$ from the photoassociation study at this asymptote in [Zinner G. et al., 2000]. Since new results have been obtained on the photoassociation experiment leading to a change in the value of C_3 by -2.5% [Degenhardt C. et al., 2003], the calculation of the value of the van der Waals coefficient C_6 should be updated, as the authors proposed it, in case of new results.

It is often that the values given by theoretician are reported without their uncertainties; it is then not easy to conclude about their reliability and to compare them with our derivations. From our side, the correlations between the experimentally determined dispersion coefficients prevent us from a comparison with the calculated theoretical coefficients realized independently for each dispersion forces. We can just notice that the most recent calculations and the values (including the exchange energy) derived in this study for the value of the C_6 are consistent. For the C_8 coefficient all published values fall within the 68% confidence interval. And for the C_{10} coefficient the agreement with all published value and its confidence interval is mainly due to the fact that this interval is large.

3.4 Critical analysis

Our analysis is based on different assumptions that I would like to remind, not only due to their importance but also because they will help to point out what could be the limitations of the study and to engage a critical discussion of their validity.

The main assumption is that the long range model equation 2.11, is valid starting from $R_{\text{out}} = 9.5 \text{ \AA}$ which allowed us to connect the long-range expansion to the well determined region of the potential. This opens at least two questions:

- What is the influence of the position of the connecting point R_{out} ?

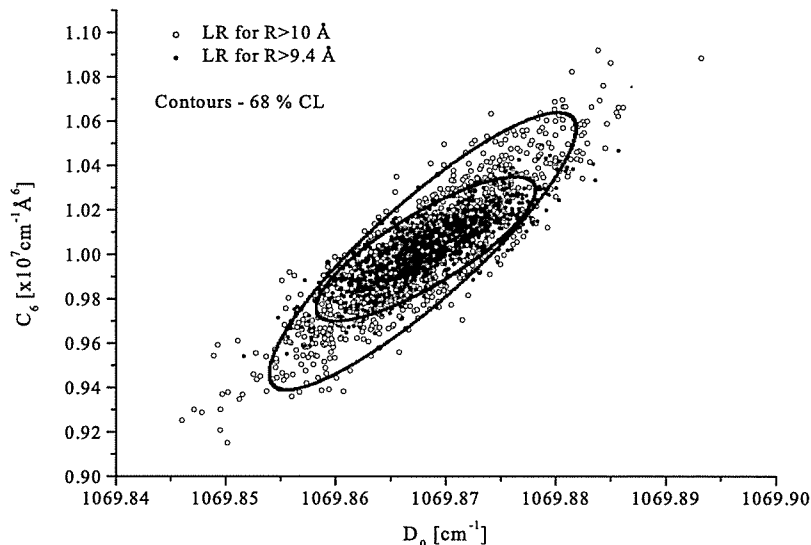


Figure 3.6: Projections of the LR parameter distribution onto the $(D_0 - C_6)$ plane using a connection at 9.4 Å and at 10 Å.

- Which consequences are expected from neglecting the contribution of the exchange energy?

Let us start by the first question. The addition of data doesn't increase very significantly the range of internuclear distances in which the potential is well defined without using the long-range model, in the sense we have described it in the section 2.4 (we refer to the graph 2.10). The amount of data is still one order of magnitude higher in this region than in the long-range part ($R > 9.5$ Å). Thus connecting the LR model beyond 9.5 Å will suffer from the relatively weak determination of this part of the potential. The reliability of the analysis is then based on the possibility to link the lower levels to the long range ones by the LR model already from 9.4 Å with a reproduction of the data within their uncertainty. We will check the variation of precision by connecting at $R_{out} > 9.5$ Å using the Monte-Carlo simulation. The graph 3.6 shows the distribution of the D_0 and C_6 parameters in the case of a connection at $R_{out} = 9.4$ Å and 10 Å and the change of the 68.3% confidence region. The procedure to get the distribution was repeated in the same way as describe before but starting with the potential representing the best data set using the point-wise representation up to 10 Å. We see that the distribution has broadened significantly compared to the one obtained

with a connection at $R_{out} = 9.4 \text{ \AA}$. The loss of accuracy reach a factor two for the C_6 coefficient and the confidence interval for D_0 has increase from $\pm 0.01 \text{ cm}^{-1}$ to $\pm 0.0145 \text{ cm}^{-1}$. The change is mainly affecting the long-range dispersion coefficients. The uncertainty on D_0 is mainly determined by the uncertainty on the highest observed level. That's why we see also a rotation of the distribution.

Let us go now to another point in our study that should be considered, namely the influence of the repulsive branch of the potential. We saw in figure 2.10 that the region below 3.5 \AA is not well fixed by the experimental data. Imagine a variation of the repulsive part that generate a change in energy position of the last bound level in the order of only 1 MHz. Could this variation affect this level without influencing the position of the other levels? To answer this question we call upon again the first order perturbation theory. The shape of the wave functions for the high lying levels of a potential are almost identical at small internuclear separations and differ only in amplitude. The position of the last bound level $v'' = 40$ with respect to the asymptote is in the order of $D_0 - E_{40} \approx 1 \text{ MHz}$ (we will come back on this prediction in the next section). The shape of the waves function $\langle R | v'' \rangle = \Psi_{v''}(R)$ of $v'' = 40$ and a more deeply bound high level $v'' = 35$ are identical up to 7.5 \AA and the ratio of their amplitude is:

$$A = \frac{\Psi_{v''=35}(R)}{\Psi_{v''=40}(R)} \approx 35 \text{ for } R < 7.5 \text{ \AA}$$

So using the perturbation theory we have a change in energy position $\delta E_{v''}$ induced by a correction to the inner potential $\delta V(R)$ localized at $R < 3.5 \text{ \AA}$ given by:

$$\delta E_{35} = \delta E_{40} \frac{\langle v''=35 | \delta V | v''=35 \rangle}{\langle v''=40 | \delta V | v''=40 \rangle} = A^2 \delta E_{40} \frac{\langle \delta V \rangle_{40}}{\langle \delta V \rangle_{40}} = A^2 \delta E_{40},$$

where the notation has been simplified. it is obvious that a variation of the potential for $R < 3.5 \text{ \AA}$ shifting the position of $v'' = 40$ by 1 MHz will shift the position of $v'' = 35$ by $\approx 1.2 \text{ GHz}$ (0.04 cm^{-1}). This local change of the potential will not affect the position of the deeply bound levels, for instance the position of ($v'' = 0$) will not be influenced. The difference $E(v''=35) - E(v''=0)$ will then change by the same amount of 1.2 GHz which is 6 times the typical experimental uncertainty. The fitting procedure will not "accept" such variation. So we see by this scaling law that the influence of the repulsive part is limited to variation of the lower v in energy position. It does not mean that the position of the steep repulsive branch is known precisely. In

fact its variation may be large but is not sufficient to move the high lying levels. In other words, its influence on the position of those levels is very weak.

Another point in our study is the estimation of the experimental uncertainties of the data. In particular we made a revision of the LIF data and obtained a normalized standard deviation of the fit close to one. The value is in fact slightly smaller than one for the long range levels ($\bar{\sigma} \sim 0.9$) and clearly smaller for the overall fit ($\bar{\sigma} \sim 0.7$), independently of the choice of representations of the potential. This indicates that either the models for the potential are too flexible or the estimation of the experimental uncertainties is still too "pessimistic". The models, in the intermediate region of the potential ($R < 9.5 \text{ \AA}$), are probably not flexible enough to compensate the random process involved in the uncertainties. Furthermore the amount of collected data is very large in this region. Therefore, it is not reasonable to think that the experimental uncertainties are relatively large and the model can compensate for all the observed levels and lead, by the fitting procedure, to smaller standard deviations than the experimental uncertainties. For the long range region we can assume that the physical model employed is simple enough to be not too flexible as well. We have tested the influence of the addition of other contributions into the model on the quality of the fit. Fitting the long-range parameters and the other terms, like the exchange energy, described previously, or higher terms in the dispersion expansion like $-C_{12}/R^{12}$, provides more degrees of freedom for the representation of the LR levels, but doesn't give a better reproduction of the observations. The value of the standard deviation doesn't decrease significantly showing that the simple model (D_e, C_6, C_8, C_{10}) is sufficient and not too flexible. We can then conclude that the uncertainties are probably still overestimated, particularly the ones of the LIF data. The consequence on the distribution of parameters, of a reduction of the uncertainties, will be observed on the long-range parameters. The c_i parameters are already very well constrained and no change will occur. Changing the errors of the FLE data to obtain an increase of the normalized standard deviation from $\bar{\sigma} \sim 0.9$ to 1 will slightly shrink the distribution of the long range parameters within the distribution obtained with $\bar{\sigma} \sim 0.9$. The confidence limits presented ($\bar{\sigma} \sim 0.9$) as results of this study are thus too large and the precision of the determination slightly underestimated.

There is another assumption inherent to every experiment which is present, for this reason, in our study as well. We suppose our measurement not affected by a bias that wasn't detected or can't be detected with our experiment solely. In this case only comparisons with other experiments devoted to the

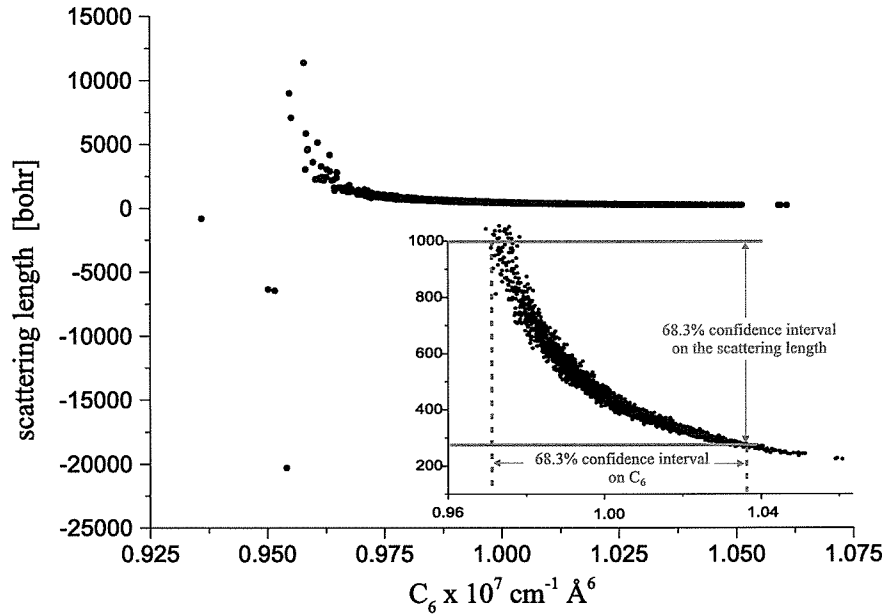


Figure 3.7: Distribution of the scattering length as function of the value of the van der Waal C_6 coefficient. A zoom of the region of the scattering length restricted by the confidence interval of the C_6 values is given in the inset.

measurement of the long range dispersion terms or involving the determination of any quantities calculable using the ground state potential can help to detect such bias. The Monte-Carlo simulation is not of help since the bias and its statistical error are not known by assumption and cannot be introduced in the simulation. Another related point is the supposition that the experimental errors follow a normal distribution. This is very likely since we have a large body of data and that every statistical distribution should tend to a normal distribution as the number of observed events or random variables increase as we learn it from the central limit theorem.

3.5 Predictions

3.5.1 The s-wave scattering length

For each simulated potential of the distribution obtained by the Monte-Carlo procedure using the model without the exchange term, we have calculated the s-wave scattering length a . The distribution of its value is shown on the figure 3.7. The 68.3% confidence interval for C_6 as well as the corresponding

interval for the value of the s-wave scattering length are shown on the inserted picture. The confidence interval of the scattering length ranges from $270a_0$ to $1000a_0$. This interval is large. The size of this interval depends also on the value of C_6 and not only on the experimental uncertainty. Since we are trying to determine a quantity which is close to a singularity, a relatively small uncertainty on the value of C_6 have a large effect on the precision of the scattering length.

The discussion in the previous section showed that the introduction of an exchange term in the long range model shifts the distribution to higher value of C_6 . The interval for the scattering length becomes $200a_0 - 800a_0$. This interval is slightly smaller due to the non-linear dependence of the scattering on C_6 .

3.5.2 The last bound level

The singularity of the scattering length is due to the weak bounding energy of the last level $v''=40$. We predict the position of this level with respect to the dissociation to be 1.3 MHz with a precision of 1.1 MHz. The distribution of predicted bond energy of the last level is presented on the graph 3.8. The 68.3% confidence on C_6 is also display. This very small value of the binding energy shows the precision of the prediction we can make with the potential. Let's understand why. As we have shown in the section 3.4 the repulsive branch of the potential has a very weak effect on the position of the levels near the asymptote and in particular on the last one. The intermediate part of the potential is fixed by the dense amount of data, so the possible value of the position of $v''=40$ can only depend on the dispersion coefficients. In fact, the binding energy of the last level is not so sensitive to the dispersion coefficients since this energy is the difference between two energies, the dissociation energy D_0 and $E_{v''=40}$ both with respect to the deepest bound level ($v=0, J=0$) which have a similar dependence on the main coefficient C_6 . Thus, this binding energy depends weakly on C_6 as we can see it in the figure 3.8. The dependence on C_6 of the binding energy of the last level is inverse to the behavior of the value of the scattering length while approaching the singularity. The reliability of derive potential and the weak variation of the binding energy with C_6 explain the precision. For the same reason an equivalent precision on the scattering length demands much higher precision on experimental data.

We see also in the figure that the distribution is narrowing as the binding energy of the level is decreasing. The influence of the other terms than C_6 express themselves in widening the distribution. So their influence decrease as the binding energy becomes smaller.

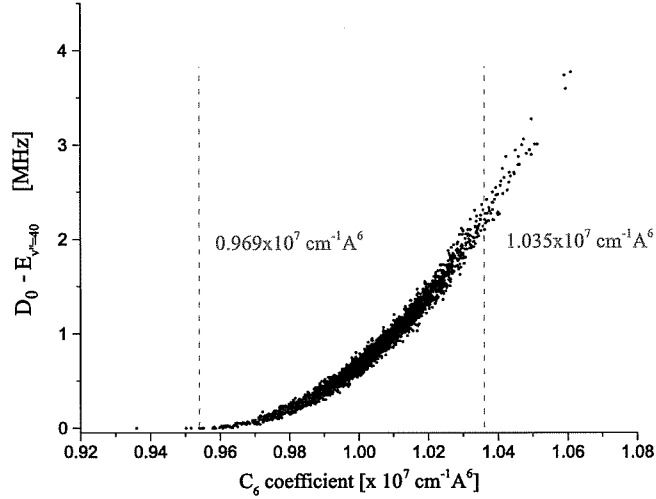


Figure 3.8: Position of the last bound level with respect to D_0

3.5.3 Analytic dependence

As a remark from the distribution of the last bound level and the scattering length it is possible to extract an analytic formula for their dependence on the coefficient C_6 . Plotting the two previous graph in log-log scales we see clearly linear dependences graphs 3.9. This means that both quantities follow a power law $\propto (C_6 - C_6^0)^m$. With a linear fit we can extract the exponents m and the coefficient C_6^0 which is the value of C_6 where the scattering length becomes singular and the binding energy of $v''=40$ reach zero. The value of $C_6^0 = 0.954(1) \text{ cm}^{-1} \text{ \AA}^6$ was determined using the figure 3.7. The value of m from the linear fit was found to be respectively $m = -0.90(5)$ for the scattering length and $m = 2.08(6)$ for the binding energy of the last bound level.

3.6 Continuation of the study

We will see in this section that the next step of this study should provide a significant improvement of the experimental uncertainty to have a better characterization of the precision of the long-range coefficients. To specify what procedure should be applied, we can ask the question whether the observation of one higher level with the filtered laser excitation spectroscopy,

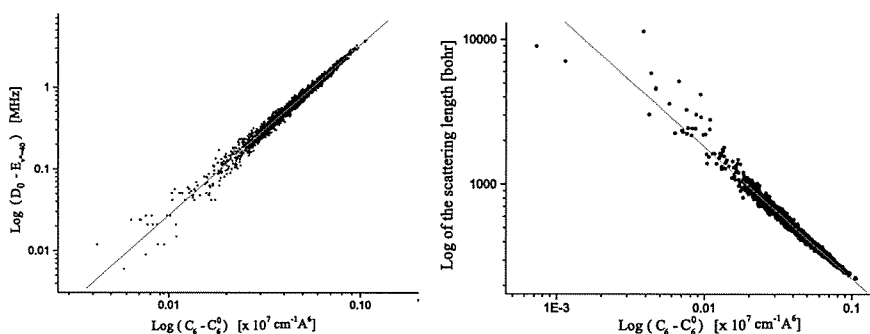


Figure 3.9: Power law on the binding energy of the last bound level with respect to D_0 and on the scattering length in function of C_6 .

namely $v''=39$, could help to decrease the uncertainty on the long range coefficients and whether the correlations can be broken. One great advantage of the Monte-Carlo simulation is it offers the possibility to simulate an experiment in which this level would have been observed. Let us suppose we have observe transitions from $v'=2$ and $J'=3$ of the B state to the levels of the ground state from $v''=31$ to $v''=39$ for $J''=2$ and 4. The uncertainty is the one obtained with the FLE technique (~ 150 MHz). The positions of these levels are generated using the potential with the best parameters. Let us now perform the Monte-Carlo simulation in the same way we have done it until now. The $(D_0 - C_6)$ projection of the resulting distribution of the long-range coefficients is plotted figure 3.10. We observed that the area covered by the both distribution without $v''=39$ in black and with $v''=39$ in red are very similar. We learn from this that the additional observation of a closer level to the dissociation, does not improve the determination of the LR dispersion coefficients, even if its classical turning point lies around 25 \AA which is 5 \AA beyond the actual largest turning point.

We can understand this fact by calculating, which constraints impose the last bound levels and its uncertainty on the potential parameters by the theory of perturbations at the first order. We consider simply the C_6 term for the long range. The change in energy position of a level δE^v introduced by a slight correction δC_6 to the value of C_6 is scaled by the expectation value of $1/R^6$. Considering two levels, one very close to the asymptote $v=40$ and a deeper one $v=35$ into the potential which have both an outer classical turning point in the long-range region. We have, in the first order:

$$\delta E^{35} = \langle v=35 | 1/R^6 | v=35 \rangle \delta C_6^{35}$$

$$\delta E^{40} = \langle v=40 | 1/R^6 | v=40 \rangle \delta C_6^{40}$$

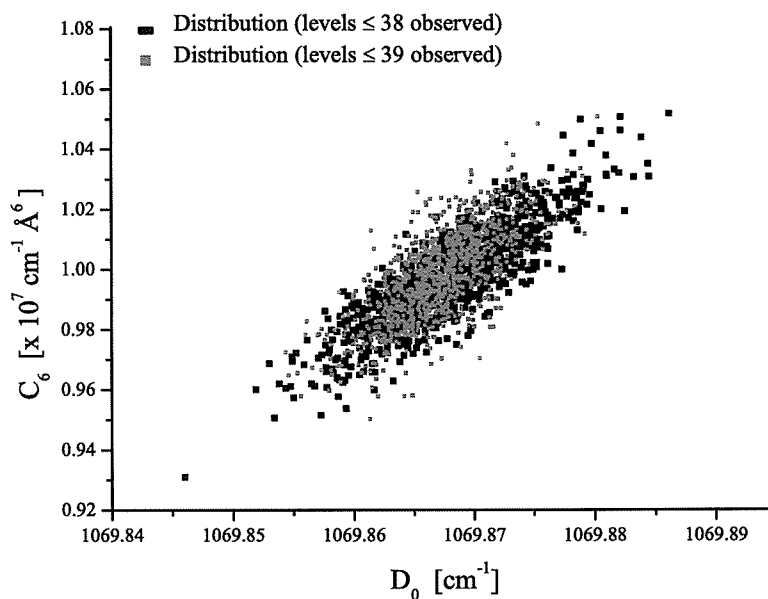


Figure 3.10: Projection on the long-range (D_0 , C_6) plane with two different synthetically constructed level sets.

A same variation or uncertainty in the position of both level will lead to different uncertainty in the value of C_6 which scales as:

$$\frac{\delta C_6^{35}}{\delta C_6^{40}} = \frac{\langle 1/R^6 \rangle_{40}}{\langle 1/R^6 \rangle_{35}},$$

where the notations of the expectation values have been simplified. The expectation value of $1/R^6$ decrease rapidly with the increase of the vibrational number v due to the increase of the amplitude of the wave function at large internuclear distance while the level approaches the asymptote. Thus we have:

$$\frac{\delta C_6^{35}}{\delta C_6^{40}} \ll 1,$$

The variation of the position of the level $v=35$ demands a correction of C_6 which is much smaller than the one necessary for a same change of the position of $v=40$. A precise knowledge of where are located the lower levels leads to stronger constraints on the variation of the value of C_6 . That is why, for similar experimental uncertainties, it is more efficient to observed deeper

bound levels than the last ones. Of course we have simplified the potential with the single term C_6/R^6 . The deeper the level is bound the more its position is influenced by the other contributions, the C_8, C_{10}, \dots dispersion interactions and the exchange energy. To describe the position of this level we need to include more term into the model. The degrees of freedom in the potential form are increasing with the number of parameters and the precision with which we can determine each contribution, knowing the position of this level accurately, decreases in consequence. To avoid such limitation one should observe levels influenced by the less contributions as possible, imposing to observe the closest levels to the asymptote. So we see that both considerations are in conflict. The higher efficiency, whether to observe the pure long-range levels or the more bound levels, depends strongly on the molecular system which is studied. For the calcium dimer case, observations with better accuracy of levels lying between $v'' = 31$ and 37 will have stronger influence on the determination of the long range-model coefficients than observations of $v'' = 38, 39$ and surely 40 with limited accuracy due to the fact that the long range model is valid at relatively short distances compared for instance, to the alkaline dimers. So the influence of the other contributions than the dispersion forces play a significant role at much shorter distance than what we expect for a non van der Waal dimer. So we can keep the long-range model simple.

Thus, a significant reduction of the parameter uncertainties can only come from a more precise spectroscopy of the last bound levels. The limitation of the present study was coming from the Doppler effect, which broadens the observed lines. To go beyond it is necessary to perform a Doppler free or highly reduced Doppler spectroscopy. Using the heat pipe apparatus the realization of such study will require a two photon spectroscopy. It is not recommended to undertake such study in a Calcium heat-pipe oven due to the rapid loss of coherence provoked by the collisions between the buffer gas or the calcium atoms with the Ca_2 molecules. One proposition is to use a beam experiment where the Doppler width of observed lines could be reduced by a factor of 100 compared to the lines obtained during this study.

The construction of such molecular beam apparatus has been started in the group. The beginning of the construction coincided with the end of the experiment using a molecular sodium beam. We have then taken the opportunity to use this apparatus and to adapt it to the case of calcium. The main difficulty is coming from the temperature that should be reached in the oven containing the calcium sample to obtain a sufficient vapor pressure of molecules. The temperature is the same as for the heat-pipe, at least 1225 K. A thermal beam apparatus is usually composed of at least two chambers. One is containing the oven with a small aperture (< 1 mm) from where the

material is expanding, and the second chamber separated from the previous one by a wall with a hole giving the arrangement of differential pumping. The axis passing by the center of both holes defines the beam axis. The two chambers are pumped and one is usually satisfied for such experiment with a background pressure in the order of 10^{-6} mbar in the second chamber where interactions with laser radiation are set up. Due to the presence of the oven with evaporating material in the first chamber, the vacuum one can reach, with usual pumps, is not so low. The presence of the relatively high voltage, necessary to heat the oven, in this environment, could lead to undesired discharges. To solve this problem we have decided to place the heaters outside the oven chamber and to heat it entirely. The price to pay is the increase of the volume to be heated and a raise of the losses either by radiation or conduction. The oven should contain enough material to provide several hours of work with one fill leading to boundaries of its size. The oven has a diameter of 6 cm and a length of 10 cm. The heated chamber has a diameter of 8 cm and a length of 50 cm. To decrease the losses a shield in the back side of the oven was placed in order to reflect radiations to the direction of the oven. The power necessary to reach at least 1225 K inside the oven place in this chamber is 2300 W. Due to the losses the non directly heated vacuum parts connected to this chamber are getting hot (100 – 200 °C). Water coolers have been then added to these parts. A design of the whole apparatus is presented in the figure 3.11. With the help of the shielding, we have reached temperatures above 1225 K as it is shown on the graph 3.12. The sudden increase of the temperature at $t = 1.5$ h comes simply from a raise of the applied voltage to the heaters. The conditions to have a beam are fulfilled but no test with calcium in the oven has been performed at the time when I am writing this manuscript.

Depending on the employed spectroscopy method to observed the last bound levels of the ground state different limitations on the precision with which one can determine the line positions can be encounter. I discuss shortly the case of a two step process. The first step is to transfer population to a selected rovibration level of the B state from a low lying vibrational level of the ground state. In a molecular beam, only levels with low rotation and vibration quantum numbers are significantly populated. The level of the B state is selected for having favorable Franck-Condon factors with the last bound levels of the ground state. Then a second scanned laser stimulates transitions from the excited level to near asymptote levels each time a resonance is crossed. The total fluorescence of the upper level is monitored as function of the second laser frequency [Samuelis C. et al., 2000]. At the same time FPI peaks for relative frequency position of lines and absorption Iodine spectrum for the absolute frequency position are recorded simultane-

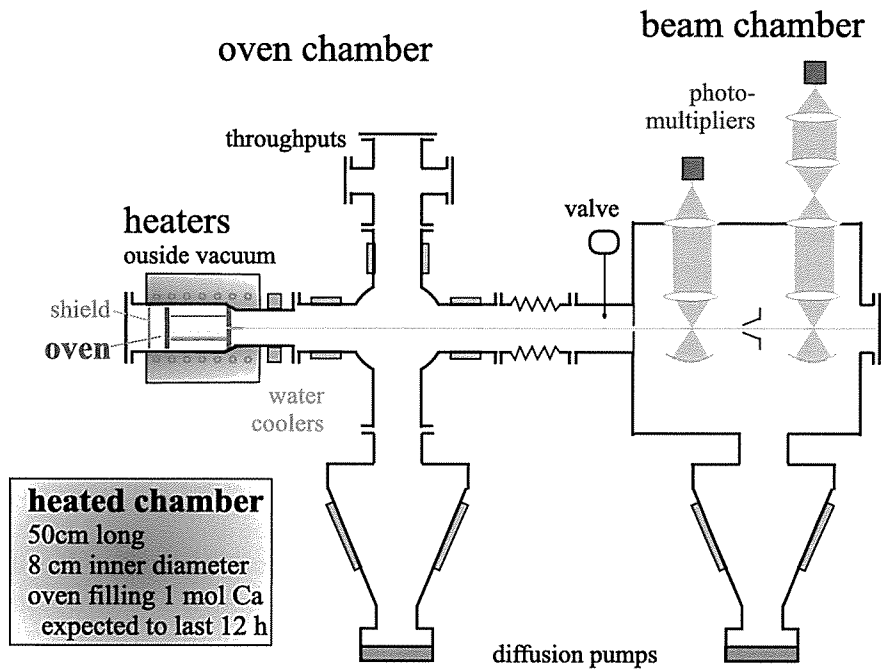


Figure 3.11: Beam apparatus adapted to the calcium dimer case (Status from june 2004). The beam chamber have not been modified compared to [Samuelis C., 2002]

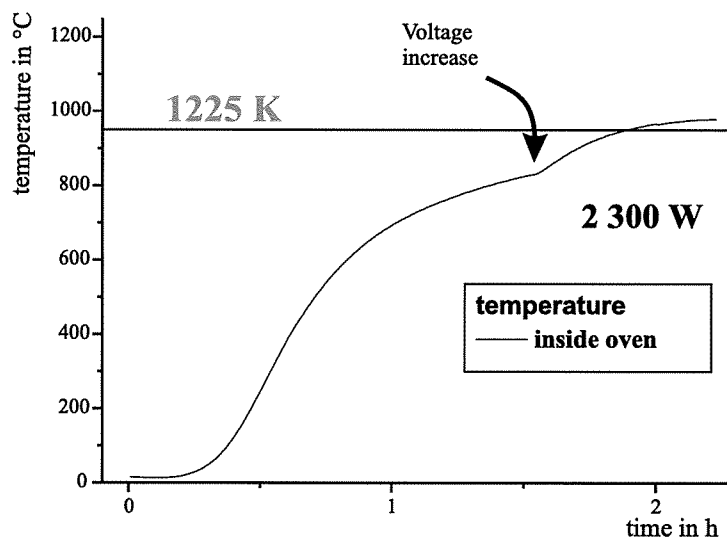


Figure 3.12: Heating-up profile with 2300 W electric power for $t \geq 1.5$ h.

ously with the second laser. One obtains a depletion spectra and the width of the observed lines is determined by the lifetime of the B state $\tau = 22 \pm 7$ ns [Bondybey V. E. and English J.H., 1984]. This lifetime broadening is the dominant effect. The residual Doppler broadening for a typical collimation ratio of 1/500 is 10 times smaller. One can propose to use a stimulated Raman adiabatic passage STIRAP configuration for the two lasers that would suppress the limitation by the upper level lifetime since it plays, in principle, no role in the transfer of population from the low to the high lying levels. No population is transferred to the intermediate level when the lasers are in resonance. In this case the Doppler broadening will be the main limitation of the experimental uncertainty.

With the reduction of Doppler effect in the molecular beam, one can obtain, in principle, an experimental uncertainty in the order of 4 MHz for the lifetime-limited measurement, and 0.3 MHz in the STIRAP configuration. With such precision we ask the question: What will be the quantitative improvement in the determination of the long-range coefficients? We ask to which extend the confidence region will be reduced and if the correlations between the parameters will decrease? Once again we could perform a simulation of the proposed experiments. I will only consider in the following that the measurements have an experimental uncertainty in the order of 4 MHz corresponding to the lifetime-limited measurement. We take the potential corresponding to the best set of parameters and generate "measured" levels. I chose to generate levels having the same quantum numbers v'' and J'' as the ones observed in our study. That is to say, I suppose to have observed levels with v'' from 35 to 38 and J'' from 4 to 10 with a precision of 3 MHz. The long range model contains the dispersion terms (D_0, C_6, C_8, C_{10}) which are fitted and the exchange energy term whose parameters are kept fixed. Then a Monte-Carlo simulation has been performed with 3000 iterations. The generated parameters set distribution is presented in the figure 3.13 projected onto the different plans of parameters and the former distribution is as well presented. We clearly see the shrink of the distribution to the small area plotted in red in the center. The real or absolute position of this distribution is not known. We just believe it lies within the 68.3% confidence limits with a probability of 68.3%. The present point of interest is not this absolute position but the reduction of the uncertainty on the long-range coefficients. The choice to put the distribution centered on the previous experiment best parameter set is thus arbitrary. The uncertainty on the value of the C_6 coefficient reduce to 0.17%, the value of C_8 to 2.5%, the value of C_{10} to 3.6%, and the uncertainty on the value of the dissociation energy is ± 80 MHz. We see that despite the high accuracy of the simulated experiment the long range coefficient C_8 and C_{10} cannot be determine better than few percent. Fur-

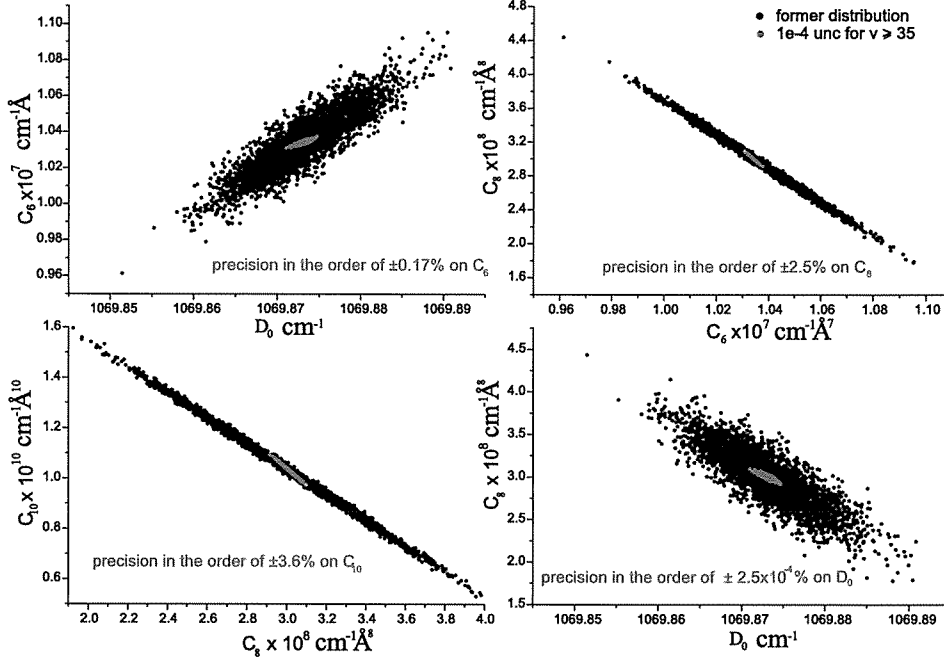


Figure 3.13: Simulation of an experiment which would have allowed to observe the high lying levels with a precision in the order of 4 MHz

thermore, we see clearly on the distribution that the correlations between the coefficients do not disappear and even do not decrease with the higher experimental precision.

We have nevertheless to consider these predictions with care. Apart from the assumptions on the model in general we have largely discussed already, some limitations of such predictions should be emphasized. In particular, the higher experimental accuracy will show the necessity of a better characterization of the exchange energy. Then, the possibility to adjust the coefficients of the exchange terms should be introduced in the fitting procedure. The distribution of the long-range coefficients from the Monte-Carlo simulation will be therefore modified. It is probable that the confidence region will be larger than calculated here. Therefore, we should see these predictions as the optimistic view of the results for the given experimental uncertainty. In addition, we see that the correlations between parameters are still present. Furthermore, the introduction of the exchange term will probably add new correlations between its parameters and the LR ones. It is certainly informative in this case to observe deeper levels than the $v'' = 35$ assumed in this simulation to have a better characterization of the exchange energy. Then,

definitively, different distributions of parameters will be obtained. It could be interesting to determine the best data set that should be observed for a given experimental line uncertainty using the Monte-Carlo simulation in order to obtain the smallest confidence limits for the LR coefficients and the exchange energy parameters.

Chapter 4

The calcium dimer B state

4.1 Introduction

The B state and the ground state potentials were not obtained independently in the study by Vidal [Vidal C. R., 1980]. Since the ground state potential have been improved significantly, we should re-investigate the $B^1\Sigma_u^+$ state as well. In section 2.3 the way we have constructed differences between observed transitions belonging to the same progressions ensured to have a set of data to fit the ground state almost independent of the B state. The determined potential of the X state allows us to construct term energies for the levels of the B state with the observed transitions of the B-X system (see chapter II and III). The applied vibrational assignment for the B state follows the one achieved by Vidal [Vidal C. R., 1980], and was used in the previous chapter. A comparison between the observed intensity patterns of several fluorescence progressions and the corresponding Franck-Condon factors will support the vibrational assignment, and will be presented in the section 4.3.

Almost all transitions from both spectroscopic methods were observed several times. We weighted them according to the inverse of their uncertainties and averaged them. We have added to the averaged transitions the calculated energies of the ground state levels involved in each transition to form a set of term energies for the B state taking the minimum of the ground state potential as the reference of energy. The predictions of level energies of the ground state potential are reliable and sufficiently accurate compared to the experimental uncertainty of the observed transitions, therefore we keep the uncertainties of the calculated term energies equal to the uncertainties of the transitions. Then the obtained term energies corresponding to the same rovibrational levels have been averaged. Altogether, the data set is composed of 72 level energies. This set will be used to determine the potential energy

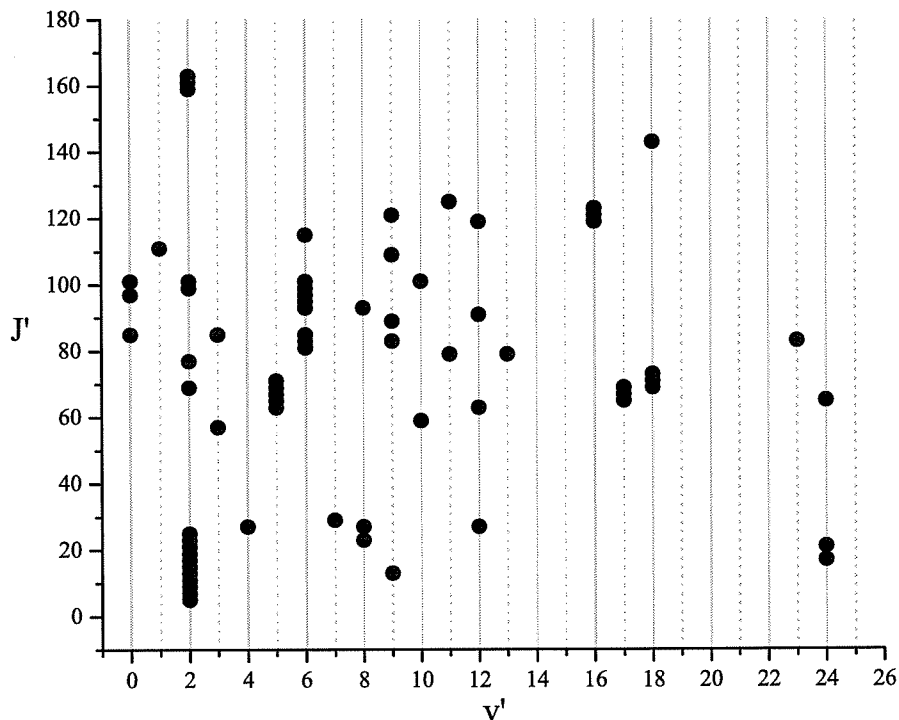


Figure 4.1: Observed data field of quantum numbers for the $B^1\Sigma_u^+$ state.

curve (PEC) of the B state. We give the field of quantum numbers of the observed data in the figure 4.1.

4.2 Potential energy curve

We assume a single potential representation within the Born-Oppenheimer approximation. We neglect all other surfaces that could be coupled to the $B^1\Sigma_u^+$ state. We will check a posteriori whether this approximation is sufficient. The potential energy curve is determined by a direct fitting procedure on the experimental term energies. We represent the potential by the analytical form as described in section 2.3.1.

At large internuclear distances the expansion is extended by

$$V(R) = D^B - C_3/R^3 - C_6/R^6 \quad \text{for } R \geq R_{out} \quad (4.1)$$

in order to ensure proper boundary conditions for the numerical resolution of the Schrödinger equation. The parameter C_6 and the dissociation energy D^B were adjusted to have a smooth connection between the analytic expansion (equation (2.8)) and the extension part (equation (4.1)). The value of R_{inn} and R_{out} are chosen to be close to the values of the smallest (3.232 Å) and the largest classical turning points (5.094 Å) of the observed levels. The RKR potential published by Vidal has been used to determine an initial representation of the potential curve. For that, the parameters $\{a_i\}$ were adjusted with a linear fitting routine in order that the functions defined in equations (2.8) and (2.9) reproduce the RKR potential curve. The value of b and R_m have been determined in this way and then fixed. Then, the parameters $\{a_i\}$ were adjusted using the non-linear fitting program (MINUIT) [MINUIT web page,] for the spectroscopic data. At each iteration the value of A , B , C_6 and D^B are adjusted to keep the continuity of the curve at the connecting points. Finally, the value of the parameter C_3 was chosen such that the dissociation energy equals $D_e^B + T_e^B = \Delta E(^1P - ^1S) + D_e^X = 24754.389 \text{ cm}^{-1}$. T_e^B is the electronic term difference between the B state potential and the minimum energy of the ground state potential, $D_e^X = 1102.074(9) \text{ cm}^{-1}$ is the dissociation energy of the ground state and $\Delta E(^1P - ^1S) = 23652.309(1) \text{ cm}^{-1}$ [C. Degenhardt, 2004] is the energy separation between the two atomic states $(4s^2)^1S_0$ and $(4s4p)^1P_1$.

We have determined a potential, which reproduces all the observed term energies with a standard deviation of $\sigma = 0.013 \text{ cm}^{-1}$ corresponding to a normalized standard deviation of $\bar{\sigma} = 1.61$. The representation of the potential is achieved with 20 parameters, 13 of which are the free parameters a_i .

4.3 Analysis

With the determined potential of the B state and the potential of the ground state, Franck-Condon factors (FCF) can be calculated and can be used to verify the assignment of the B state, which was used up to now. Figure 4.2 presents a comparison between calculated Franck-Condon factors and the intensity pattern of several fluorescence progressions. The progressions were obtained by the excitation of low vibrational levels of the $B^1\Sigma_u^+$ state by the two single mode $2\omega\text{Nd:YAG}$ lasers. The excited levels (v', J') are (0, 85), (0, 101) and (2, 21). We choose these low vibrational levels since their Franck-Condon factors are very sensitive to the choice of assignment. We see in the graph that an excellent agreement is obtained between the observed intensity patterns and the FCF using the present potentials, which confirms

that the original assignment by Vidal was correct.

We see in figure 4.1 that the field of data is quite scattered. Therefore, we

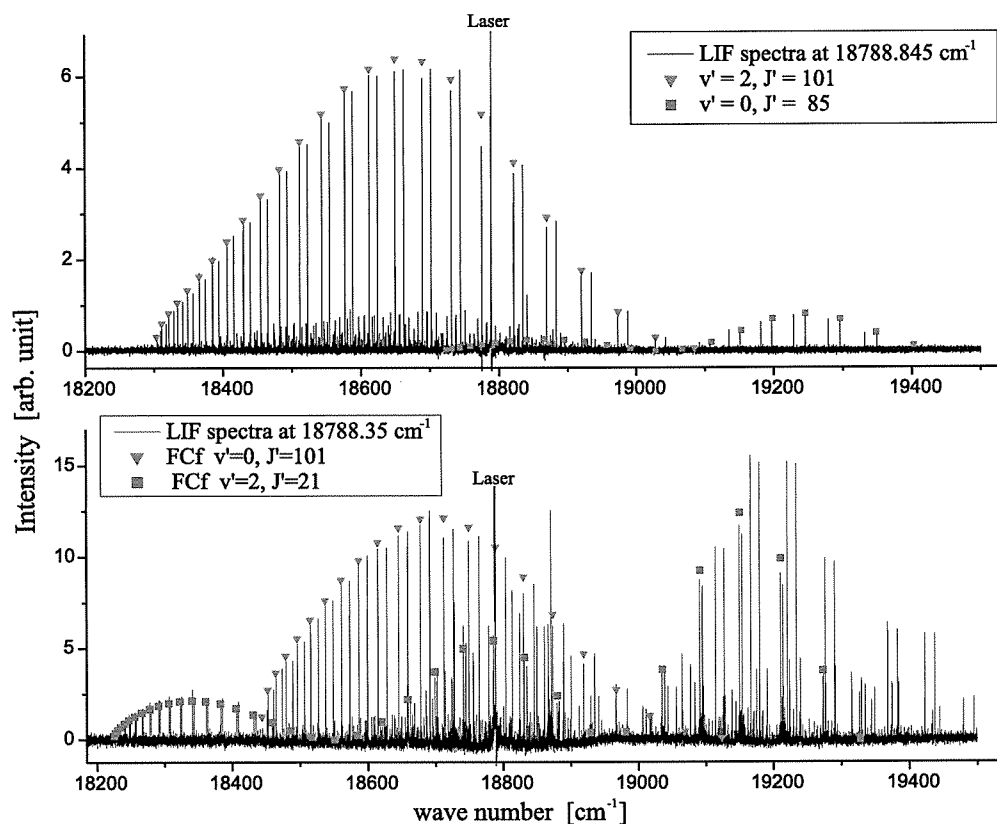


Figure 4.2: Comparison between calculated Franck-Condon factors with the intensity pattern of several fluorescence progressions to the $X^1\Sigma_g^+$ state from low excited levels of the $B^1\Sigma_u^+$ state. The good agreement confirms the assignment made by Vidal.

check whether the data constrain sufficiently the shape of the potential over the whole range of observed turning points. This is not this range, which defines the range where the potential is reliably determined as it has been demonstrated in section 2.4. Depending on the density of data, the range of reliability can be smaller than the range of turning points of the collected data. In this case the extrapolated parts the potential can not be used for making accurate predictions of molecular quantities like, for instance, energy level positions. To check this point, we have fitted the term energies using another representation of the fitted potential with the same analytical form but using 14 a_i parameters and a different value for R_m and b . The achieved

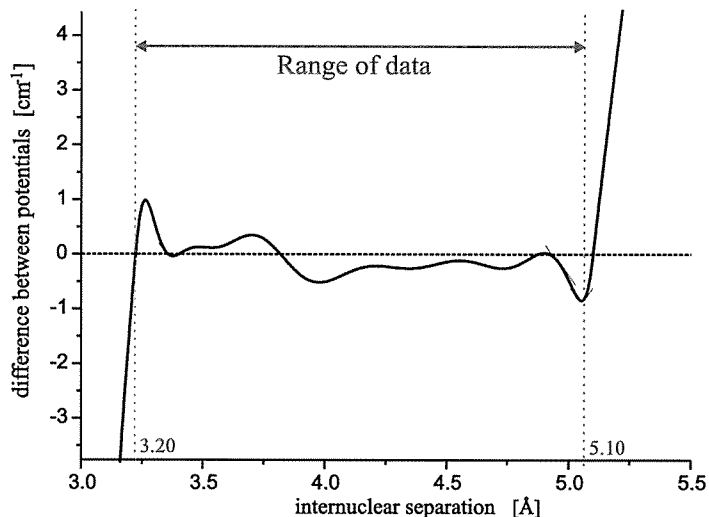


Figure 4.3: Difference between two potential curves of the $B^1\Sigma_u^+$ state. Both represent the observed data with similar quality.

quality of the fit is very similar $\bar{\sigma} = 1.59$. Figure 4.3 presents the difference between both potential curves. In the range $2.2 \text{ \AA} \geq R \geq 5.1 \text{ \AA}$, the difference between both potentials oscillate. Obviously, these oscillations do not affect the quality of the representation of the spectroscopic data, since the value of the standard deviation $\bar{\sigma}$ of both potentials are almost equal. But, the shape of the potential curve depends on the choice of representation. We can attribute the presence of these oscillations to the restricted amount of data. These data are probably not sufficient to strongly constrain the shape of the potential; therefore the representation of the observed levels is not unique. Nevertheless, the goal to determine a potential energy curve, which can accurately reproduced the observe data, is fulfilled. This potential can be used to make reliable predictions of energy positions of levels whose turning points lie within this range with an accuracy in the order of our experimental uncertainty. Outside the range of data, the difference between the potentials is significantly larger. For clarity, at very large internuclear separations, not presented in the figure, the difference between the potentials tends to zero since the potential were built to have the same dissociation energy. The extension functions (2.10) and (4.1) are used at $R_{out} = 5.1 \text{ \AA}$ and beyond. This connection is thus realized at very short internuclear distance. Therefore, the coefficients of these functions have no other meaning than ensuring correct boundary conditions for the resolution of the Schrödinger equation. This potential can not be used to predict the position of levels having a classical

turning point larger than 5.1 Å.

The potential energy curve of the B state has been determined from 2.2 Å to 5.1 Å corresponding to an energy range of 2899 cm⁻¹ from the minimum to the potential energy at 5.1 Å. The values of all the parameters of the potential are listed in the table A.3. The value of the electronic term difference was calculated with the determined potential function $T_e^B = 18963.9(5)$ cm⁻¹. Thus, the dissociation energy of the B state is $D_e^B = 5790.4(5)$ cm⁻¹. These values depend on the choice of the representation and can not be determined with a better precision than 0.5 cm⁻¹ as we can see it in the figure 4.3. The energy distance between the level ($v' = 0, J' = 0$) and the asymptote, which is independent of the chosen representation, is $D_0^B = 5722.317(9)$ cm⁻¹. The parameters of the determined potential and the molecular constants are given in the table A.3.

The standard deviation, given in section 4.2, is slightly larger than the average experimental uncertainty, which is equal to 0.009 cm⁻¹. This is due to 17 levels whose residuals exceed the experimental uncertainty by a factor varying from 2 to 5. No typographic errors or misassignments in the data list have been found for these levels. Since the orders of magnitude of these deviations are smaller or equal to the possible Doppler shift plus collisional shift, we cannot attribute them to be caused by a perturbing molecular state. Thus, among the observed data there is no evidence of any perturbation within the experimental uncertainty. This is in agreement with the observations made by Vidal who claimed that significant deviations appear only for levels with $v' \geq 25$ which is above the highest observed vibrational levels of this study. Nevertheless, we cannot exclude the presence of weak or much localized perturbations below $v' = 25$ due to the fact that the present field of data is rather scattered. For this reason, and also to improve the quality of the potential curve even more, a complete and precise investigation is necessary.

Chapter 5

The A–c coupled electronic states of calcium dimer

We are interested in the $A^1\Sigma_u^+$ ($^1D_2 + ^1S_0$), $c^3\Pi_u$ ($^3P + ^1S_0$), and $a^3\Sigma_u$ ($^3P + ^1S_0$) coupled states. The knowledge of the potential curves can allow the description of the scattering of atoms in ground and 3P_1 excited states. The contribution of the atom-atom collisions to the error budget of an optical clock using the $^3P_1 \leftarrow ^1S_0$ intercombination transition can be analyzed. Trap loss while cooling on this transition can be also estimated.

The A - c coupled states have been studied since the middle of the eighties by Bondybey and English in a supersonic beam [Bondybey V. E. and English J.H., 1984], and by Hofmann and Harris using a heat pipe cell [Hofmann R. T. and Harris D. O., 1986]. Molecular constants and coupling coefficients have been derived by Hofmann and Harris using a local deperturbation approach.

In this work a coupled channel treatment using the Fourier grid Hamiltonian method combine with a fitting procedure will be employed to determine the shape of the potentials and of the coupling in order to reproduce the observed energy levels. In the section 5.1 I will present the results achieved by Hofmann and Harris, then I will present our own spectroscopy. In the section 5.2, I will describe the theory underlying the coupled system and present the deperturbation analysis and the achieved results in section 5.3.

5.1 Spectroscopic measurements

5.1.1 Background

The $A^1\Sigma_u^+ - X^1\Sigma_g^+$ red system was first observed by [Bondybey V. E. and English J.H., 1984] using a supersonic jet experiment created from the vaporization of calcium metal by a pulsed, Q-switched Nd-YAG laser. The spectroscopic interrogation was realized by a pulsed dye laser system limiting their experimental uncertainty to a few tenths of a wave number. The total fluorescence emission was recorded tuning the excitation laser. Only bands starting from low ro-vibrational levels of the ground state, the only ones populated in the supersonic beam, were observed. 10 vibronic bands were recorded from 14500 cm^{-1} to 15730 cm^{-1} . Vibrational constants were derived. Their vibrational assignment was based on the fact that no bands below $\sim 14500\text{ cm}^{-1}$ were observed and thus the lowest band around 15417.6 cm^{-1} was labeled as $v_A = 0 - v'' = 0$. Numerous rotational perturbations were observed but no deperturbation analysis was performed. The same year Hofmann and Harris published Franck-Condon factors between the first vibrational levels of both the X and A states are very weak for low J-values, and thus are not observable in a supersonic jet [Hofmann R. T. and Harris D. O., 1984]. The vibrational assignment achieved by Bondybey and English is thus questionable!

Hofmann and Harris published two years later the results of a more thorough investigation of the $A^1\Sigma_u^+ - X^1\Sigma_g^+$ system [Hofmann R. T. and Harris D. O., 1986]. Since their observed and assigned transitions were available we collected them and used them for our own investigations. They performed laser induced fluorescence spectroscopy in a heat pipe oven, and used, in addition, the filtered laser excitation technique to observed band heads. Argon ion pumped DCM dye laser operated in single mode configuration was employed for the excitation to the A state. A $3/4\text{ m}$ monochromator of 0.1 nm resolution was used for the frequency-selective detection of the induced fluorescence. The I_2 atlas from Gerstenkorn and Luc was used for absolute calibration of the obtained spectra. They stated an experimental uncertainty of 0.01 cm^{-1} . From the observation of P-R doublets they assign the progression to the $A^1\Sigma_u^+ - X^1\Sigma_g^+$ system, and measured 720 lines corresponding to 340 different levels of the A state and involving 10 different vibrational quantum numbers of the A state. Rotational assignment was realized using Vidal's data of the X state. Since the observed A-X bands never involved ground state levels with vibration quantum number v' higher than 11, the quality of the ground state Dunham coefficients allowed reliable rotational assignments (see beginning of the chapter devoted to the ground state).

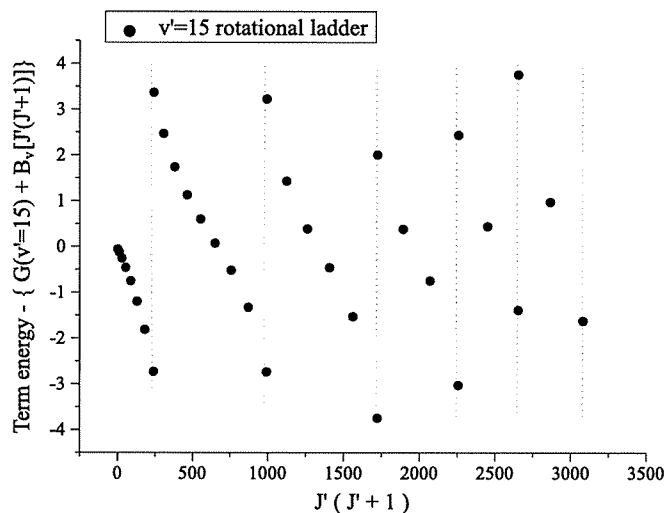


Figure 5.1: Presentation of the 6 local perturbations observed by Hofmann and Harris on the rotational levels of the vibrational level assign by them to be $v' = 15$. Term energies of the rotation ladder subtracted by the regular $G_{v_A} + B_{v_A} J'(J'+1)$ behavior.

The vibrational assignment was realized by comparing Franck-Condon factors obtained with an RKR potential of the A state and the Vidal's X state potential to the relative emission lines intensities. Their assignment of the lowest observed vibrational level of the A state is $v_A = 7$. This consists of a large extrapolation from the lowest vibrational levels, which are usually more sensitive to different assignments. A number of 28 local perturbations were observed. Splitting of lines from 5 to 15 cm^{-1} have been observed. For instance, the rotational ladder of v_A assign to be $v_A = 15$ presents up to 6 local perturbations in the observed region from $J' = 1$ to $J' = 55$. The figure 5.1 presents the perturbations for $v_A = 15$. To see clearly the perturbations a simple Dunham expansion $G_{v_A} + B_{v_A} J'(J'+1)$ has been subtracted from the term energies obtained by adding to the observed transitions the energies of the ground state levels.

The lowest local perturbation was observed for the vibrational level assigned to $v_A = 7$.

5.1.2 Spectroscopy

We are interested to collect precise spectroscopic data on the $A^1\Sigma_u^+$ and $c^3\Pi_u$ states. The $c^3\Pi_u$ state is not optically connected to the ground state $X^1\Sigma_g^+$. Therefore the observation of its level-structure by a direct laser excitation

from the ground state is not efficient. One can propose to perform a two step excitation. First populate a level of the $A^1\Sigma_u^+$ state which has sufficient triplet character due to its coupling with the *c* state, and from this level, excite a level of another triplet state, and observed the fluorescence to the *c* state. This method would provide a lot of information about the *c* state. The realization of such spectroscopy is not favorable since no other triplet states than the *c* state have been studied so far for the calcium dimer. Furthermore, the choice of a two step excitation performed with our apparatus is not judicious due to the relatively high density of calcium atoms present in the heat pipe oven. The first excited level will be depopulated by collision and will lead to an extremely weak efficiency for the second excitation.

We have chosen the same approach as proposed by Hofmann and Harris to study the A -c system. The rovibrational levels of the A state will be investigated by laser induced fluorescence. Only the effects caused by the coupling of the *c* state to the A state levels will be observed. The LIF technique provides less information on the upper state than on the lower state. We use the possibility to increase the collisionally induced lines by varying the temperature of the heat pipe oven to populate more neighbor rovibrational levels of the A state.

We performed this study using the same apparatus as described in the chapter 2, which was employed for the LIF study of the $B^1\Sigma_u^+ - X^1\Sigma_g^+$ system. The fluorescence was recorded and analyzed with the Fourier transform interferometer. A frequency stabilized, linear DCM dye laser (Coherent 599) pumped by an argon ion laser (Innova 400) was run in single mode with a typical output power of 70 mW. It was used to excite transitions in the interval 14900 cm^{-1} to 15650 cm^{-1} . Transitions to the vibrational levels $v_A = 7$ to 13 (following the assignment of Hofmann and Harris) were observed. The long term drift of the frequency of the laser was less than 10 MHz per hour, which is sufficiently smaller than the Doppler width of the lines in this frequency region $\sim 1.3\text{ GHz} \approx 0.043\text{ cm}^{-1}$ at 1260 K, to allow a stable excitation during the time of recordings (~ 20 min corresponding to 20 scans). To observe transitions involving more levels of the A state, the oven was operated at (1240 - 1275 K). In this way the number of collision induced satellites was increased. The figure 5.2 presents the P-R doublets progression from the excitation transition $(11, 29) \leftarrow (0, 28)$ at 15514.843 cm^{-1} . On the insert a zoom around the fluorescence lines P(28) and R(30) of $v'' = 0$ shows the relatively large number of induced collision satellites (24 satellites corresponding to 12 different J' -values). The instrumental resolution of the interferometer was chosen to be 0.05 cm^{-1} . With a triangular apodization the instrument line width is 0.05 cm^{-1} (section 2.2.4). Since in single mode operation of the laser, only a selected velocity class is excited, no Doppler

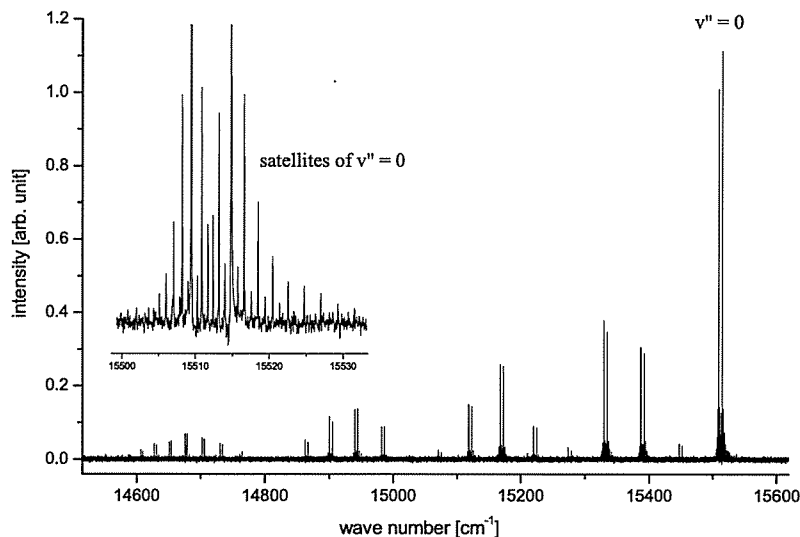


Figure 5.2: Vibrational progression obtained from the excited $(11, 29) \leftarrow (0, 28)$ transition. In the inset the faster decrease of the intensity of the satellite lines at lower frequency, corresponding to lower J' -values, compared to intensity at the higher frequency is due to the decrease of degeneracy of the rotational levels $\propto (2J+1)$ and not due to a local perturbation.

broadening occurs. The lifetime of the A state is 57 ± 5 ns [Bondybey V. E. and English J.H., 1984] giving a homogeneous broadening of $5.85 \times 10^{-4} \text{ cm}^{-1}$, which is negligible compared to the instrumental broadening. The broadening due to the size of the aperture of the instrument (~ 1.3 mm) is in the order of 0.025 cm^{-1} (see explanation section 2.2.4). Taking the relation 2.3 and $\delta\sigma_{\text{laser}} = 10 \text{ MHz}$ we obtain a line width of 0.056 cm^{-1} . The widths of the measured lines with a signal to noise ratio higher than 10 was $\sim 0.062 \text{ cm}^{-1}$. Collisional broadening due to the higher temperatures are probably responsible for the additional width of 0.026 cm^{-1} .

The relative uncertainty of the line positions within a spectrum is then estimated to 0.006 cm^{-1} for lines having a SNR higher than 10. The relative uncertainty was increased to 0.01 cm^{-1} for lines with a SNR around 5, and to 0.02 cm^{-1} for lines with a SNR lower than 3.

Due to the possible excitation of different class of velocities depending on the frequency of the laser a Doppler shift can happen. The OPUS software, controlling the interferometer, offers the possibility to perform short scans in order to fast record spectra with low resolution, and to display them on live

in a preview mode, before starting the recording with a higher resolution. We used this option to check that the excitation was tuned at maximum of emission for the selected A-X transitions before recording. In this way we reduced the Doppler shifts to a magnitude of about ten times smaller than the observed width, i.e. in the order of $\sim 0.006 \text{ cm}^{-1}$.

The absolute accuracy in line positions for different recordings with the interferometer, in the region around 670 nm, is equal to $220 \text{ MHz} \approx 0.0075 \text{ cm}^{-1}$. The residual Doppler shift and the absolute accuracy of the instrument lead to an absolute uncertainty of line positions of 0.009 cm^{-1} . We will have to take into account this absolute uncertainty when we will form term energies with the transitions from different recordings.

The next step of our investigation was to observe lower vibrational levels than $v_A = 7$ and to detect whether local perturbations are present. The transitions to $v_A = 6$ with favorable Franck-Condon factors fall into the gain profile of the DCM dye, i.e. in the region $14950 - 15085 \text{ cm}^{-1}$. Positions of these transitions were estimated using an extrapolated Dunham expansion to lower v_A . The estimation was not better than few tenth of a wave number, so the laser was scanned and the fluorescence intensity was monitored using the preview mode of the interferometer software system.

From the highest laser frequencies to the lowest ones we used, we have observed a continuous increase of the noise in the recorded spectral region coming from the oven radiation. This was particularly visible in the preview mode since only fast Fourier transformation of single low resolution scans are performed and displayed. Nevertheless we could still use the preview mode to search for the lines. Once a transition to $v_A = 6$ for a given J' was found, normal high resolution scans were recorded, and the spectrum showed the P - R doublets and their neighboring rotational satellites. It was then straightforward to follow the rotational progression. In the region around $J' = 51$ a local perturbation was found with a splitting of 10.58 cm^{-1} . As the rotational levels approach the local perturbation the intensity of the lines decreases rapidly due to the raising of the $c^3\Pi_u$ character of the levels. A much smaller local perturbation $\sim 0.5 \text{ cm}^{-1}$ compared to a regular behavior was found approaching $J' = 39$. An occasional excitation of a higher J' of $v_A = 6$ during the observation of the lowest rotational levels allowed us to "pass" the local perturbation. We completed the observation to $J' = 89$ and a more complex structure was found from $J' = 81$ to 89. The rotational progression of the vibrational level still assigned to $v_A = 6$ is presented on the figure 5.3. In the same way as in figure 5.1 we subtracted from the term energies a simple linear Dunham expansion which has the only purpose to scale the progression to present clearly the observed perturbations.

To observe even lower v_A we used in the same linear dye laser, the pyridine 1

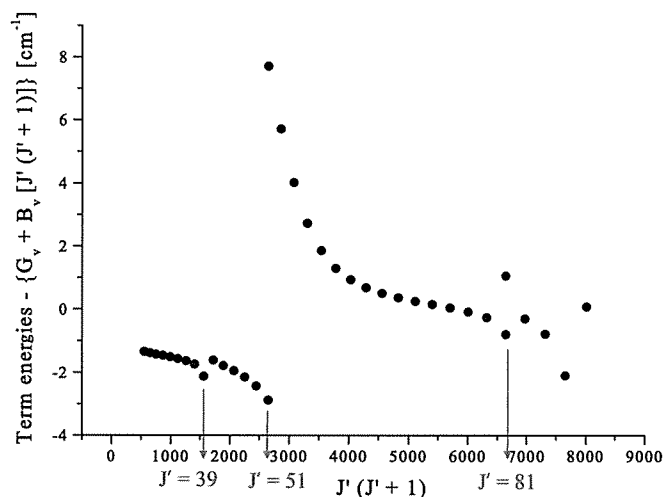


Figure 5.3: Presentation of the local perturbations on the assigned $v_A = 6$ rotational levels. Term energies of the rotation ladder subtracted by the regular $G_{v_A} + B_{v_A} J'(J'+1)$ behavior.

dye. The gain profile of the dye allowed us to obtain lasing from 13850 cm^{-1} to 14560 cm^{-1} with an output power of 100 mW at maximum. This lasing region does not overlap with the one obtained with the DCM dye. There is a frequency region from 14560 to 14950 cm^{-1} , which was not accessible. DCM and Pyridine dyes cannot be mixed to enlarge the gain profiles. With slight mixing of both dyes no lasing can be obtained. Among the well established dyes there is none, which produces lasing in this frequency region and can be pumped by our argon ion laser. Furthermore, we do not have in our group another laser working in this frequency interval. This region corresponds to the transitions offering the most favorable Franck-Condon factors between the ground state levels to the $v_A = 4$ and 5 levels of the A state. The ro-vibrational levels below $v_A = 4$ are reachable with the pyridine dye laser with favorable Franck-Condon factors. Like for the higher vibrational levels we wanted to use the preview mode to find the lower v_A lines. But, the signal-to-noise ratio in this mode was very low due to the emitted red light of the oven. Furthermore, the gap in frequency between DCM and pyridine lasers and the unknown magnitude of the global or local shifts due to the perturbation hinder large and precise extrapolation towards the lower v_A by the present Dunham expansion or potential energy curve. It was necessary to proceed differently than previously to find the resonances and to tune precisely the laser to the maximum of emission of the found lines.

To observe the fluorescence lines when tuning the laser, the emission should

be recorded through a very narrow spectral band width to increase significantly the SNR of the detection. We then decided to employ the 1 m (GCA/McPherson Instruments) monochromator in a similar way as during the filtered laser excitation spectroscopy. We kept one optical access of the heat pipe for recording spectra via the interferometer and used the other optical access to collect the fluorescence light and to reflect and focus it to the entrance slit of the monochromator. This monochromator was used with a band pass frequency width of about 2 to 5 cm^{-1} giving a much higher signal-to-noise ratio compared to the one in the preview mode. In addition, low pass filters RG665 and RG695 were employed. The light passing through the monochromator was detected using a broad band Hamamatsu photomultiplier (R928). Knowing the frequency range in which the laser is scanned to excite a selected upper ro-vibrational level, and knowing precisely the position of the ground state levels, it is easy to set the central position of the frequency window to a chosen transition involving neighboring v'' of the excited one. The sufficiently large size of the window permits to keep it fixed during the scan of the laser by 2 or 5 cm^{-1} . When the laser comes into resonance, fluorescence to the ground state is emitted, but only upper excited levels which fluorescence falls down into the selected window are detected. More detailed explanations of the technique can be found in the section 2.7. To improve the detection a differential amplifier was added. A time averaging of 100 ms was applied for the intensity detected through the monochromator I_{PMT} . The intensity of the laser I_ν was simultaneously recorded and used to form the following signal: $I = [g \times I_{\text{PMT}} - I_\nu] / I_\nu$, where g is an adjustable gain factor. When a Ca_2 line is found and the laser put to the maximum of emission and stabilized there, a fluorescence spectrum is recorded with the Fourier transform interferometer. A scheme of the setup is presented figure 5.4. Using this technique we have localized transitions to the $v_A = 1, 2$ and 3 vibrational levels of the A state. Only some satellites were present in the spectra due to the decrease of the signal-to-noise ratio. Double-sided forward and backward scans allowing an increase of the signal-to-noise ratio compared to the single sided scans for the same number of scans was employed. Nevertheless, often not more than 8 collision satellites were observed for the strongest lines corresponding to 4 different rotational quantum numbers J' . For the rotational levels $v_A = 1, 2$ and 3 we did not observed local perturbations. In order to check whether a local perturbation appears at high J' of $v_A = 3$ the rotational progression was followed from $J' = 93$ to 113. A progressive deviation towards lower term value from a regular behavior, compared to the rotational progression of $v_A = 2$ was discovered. To observe $v_A = 5$ and 4 excitations of transitions having not so favorable FCF should then be performed. This was realized for $v_A = 4$ but necessitated

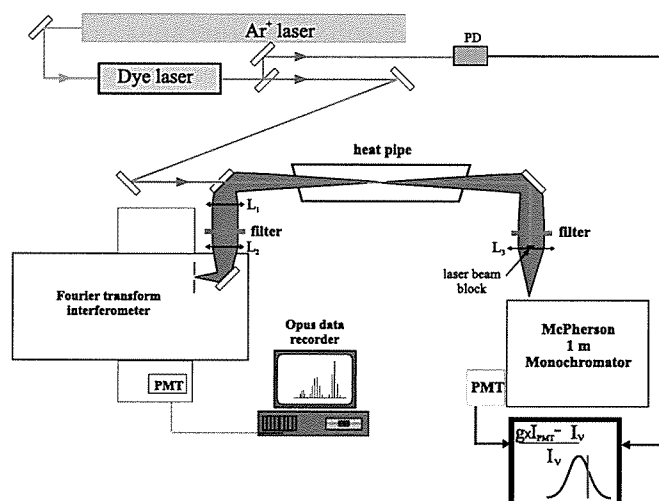


Figure 5.4: Experimental setup for finding and tuning the laser radiation to resonance and record LIF spectra.

a different spectroscopic method since the obtained signal was rather weak. Since no satellites were present, the Fourier transform spectroscopy was not of particular advantage.

We decided to apply the complete filtered laser excitation spectroscopy. Until now, we had the possibility to observe lines through the monochromator but no frequency scale for measuring the position of the lines was used. The purpose was just to find lines and to excite them at the maximum of emission and to record Fourier transform spectra.

The temperature of the heat pipe oven was reduced to 1240 K. We used the spectroscopy exactly as it was described for the observation of the last bound levels of the ground state, section 2.7. The window width was set to 2 cm^{-1} and adjusted on $v'' = 3$ for a selected J' which corresponds to the highest Franck-Condon factor of its oscillatory pattern in function of v'' . We scanned the laser continuously within intervals of ~ 10 to 15 GHz to excite reachable transitions from $v'' = 11$ which correspond to the second maximum of FCF, which is a factor 2 lower than the first one. We recorded simultaneously iodine differential absorption spectra, from a 60 cm heated cell (820 K), for absolute frequency calibration and high finesse cavity peaks of 149.7 MHz spectral range for relative frequency determination. The molecular signal was time averaged for about 300 ms . The power of the laser was taken as well for intensity calibration of the molecular calcium signal. The four signals were recorded via a multi-channel voltage recorder connected to an analogue-to-digital signal converter treated by computer Labview software

equipment. We used the IodineSpec software program to calibrate the spectra [IodineSpec,]. It provides a prediction of I₂ transitions with an accuracy better than 25 MHz in this spectral region. The width of the calcium lines was 0.042(1) cm⁻¹ corresponding to the Doppler width of 0.04 cm⁻¹ and a residual broadening of about 0.012(3) cm⁻¹. The width of the Iodine lines (heated to 850 K) was in the order of 0.04 cm⁻¹ depending on the underneath hyperfine structure. The absolute experimental uncertainty is determined by the precision whose I₂ and Ca₂ line centers are estimated. The signal-to-noise ratio was sufficiently high for the I₂ and Ca₂ lines to allow a determination of their centers better than 0.004 cm⁻¹ for each of them. The accuracy of the position of lines was then estimated to be 0.005 cm⁻¹. The (4, 61) → (11, 62) measured Ca₂ line is presented on the figure 5.5. Rotational levels

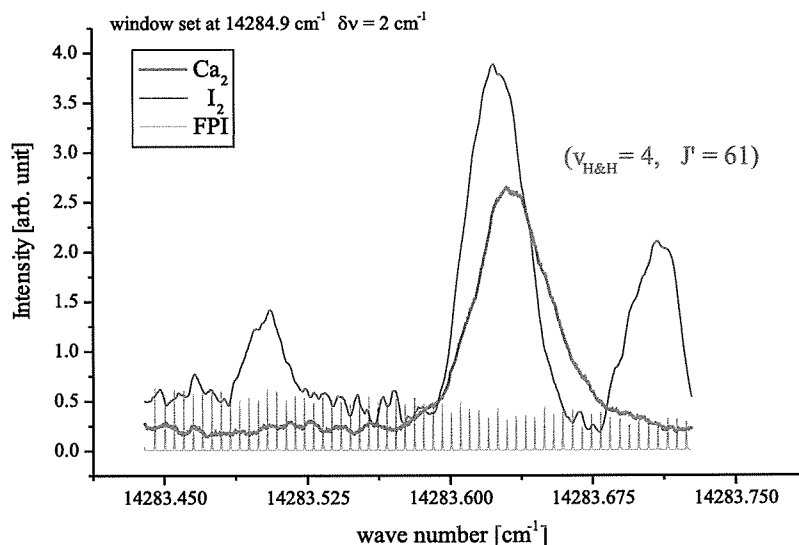


Figure 5.5: (4, 61) → (11, 62) Ca₂ calcium line recorded with I₂ absorption lines (reversed here) and FPI peaks. The traces of Ca₂ and I₂ have been smoothed.

from $J' = 27$ to 77 were observed for $v_A = 4$ in this way. No local perturbations were observed for low J' but a strong deviation to lower term values is present towards $J' = 77$. These onsets of local perturbations for $v_A = 3$ at high J' and for $v_A = 4$ for J' -value approaching 77 are caused by the rotational progression of the same vibrational v_c level of the $c^3\Pi_u$ state. Since no local perturbation has been observed for lower levels both perturbations are the manifestation of the two lowest local perturbations of the A - c system. The presence of strong perturbations, the frequency position of the laser at the end of the gain profile of the dye laser to excite transitions with smaller

Franck-Condon factors compared to $v_A = 4$, and the presence of impurities becoming rather strong in this region prevented us to observe more than three rotational levels for $v_A = 5$ ($J' = 43, 45$, and 47) with the FLE technique. The signal to noise ratio was very low, in the order of 1.5, leading to an accuracy for these three lines to be not better than 0.03 cm^{-1} . Rovibrational levels of $v_A = 5$ with J' -values higher than 99 have been obtained during the LIF experiment.

Search for $v_A = 0$ has been tried. The transitions starting from $v'' = 13$ of the ground state offer the most favorable Franck-Condon factors 0.033 to excite $v_A = 0$ for J' -values around 45. This corresponds to frequency transition lying outside the gain region of the pyridine dye laser. The laser was then tuned in the interval [$13817 \text{ cm}^{-1} - 13823 \text{ cm}^{-1}$] with which the transitions starting from $v'' = 9$ can be searched. The FCF is then 0.024. The scanned range was larger than the expected spacing between two consecutive rotational transitions ($\sim 4.3 \text{ cm}^{-1}$). The window of the monochromator was set to the frequency interval [$13660 \text{ cm}^{-1} - 13664 \text{ cm}^{-1}$] where we expect fluorescence from $v_A = 0$, $J' = 45$ to $v'' = 13$, $J'' = 46$. The laser intensity was two times lower than in the frequency range for the excitation of $v_A = 1$ and 2. During the scanning procedure we have not found any transition that we could assign to $v_A = 0$.

5.1.3 Revision of the vibrational assignments

Let us talk first about the vibrational assignment of the A state. The coupling between the A state and the c state affects the vibrational levels below $v_A = 4$ as a global shift of the rovibrational levels towards lower energies. The variation of the shifts with v_A -values and J' -values is much more monotonic compared to the local perturbation at higher v_A -values. These shifts are also much smaller than the vibrational spacing of the levels. We can thus consider that although a one channel fit of such levels will not provide a good reproduction of energy level positions, will nevertheless be sufficient for a determination of Franck-Condon factors. We can test different assignments and compare the intensity pattern of the fluorescence progressions to the calculated FCF for each fitted potentials. Three different assignments other than the one of Hofmann and Harris and fits of potential energy curves of the A state on the observed levels were performed for $v < 4$. Labeling the vibrational assignment of Hofmann and Harris as $v_{\text{H\&H}}$ four potential curves were tested corresponding to $v_{\text{H\&H}} - 1$, $v_{\text{H\&H}}$, $v_{\text{H\&H}} + 1$ and $v_{\text{H\&H}} + 2$. The fluorescence progressions obtained by the excitation of the transition ($v_{\text{H\&H}} = 1, 61$) \leftarrow (8, 62), ($v_{\text{H\&H}} = 2, 57$) \leftarrow (6, 58) and ($v_{\text{H\&H}} = 3, 47$) \leftarrow (4, 46) are compared to the predicted Franck-Condon factors for the different

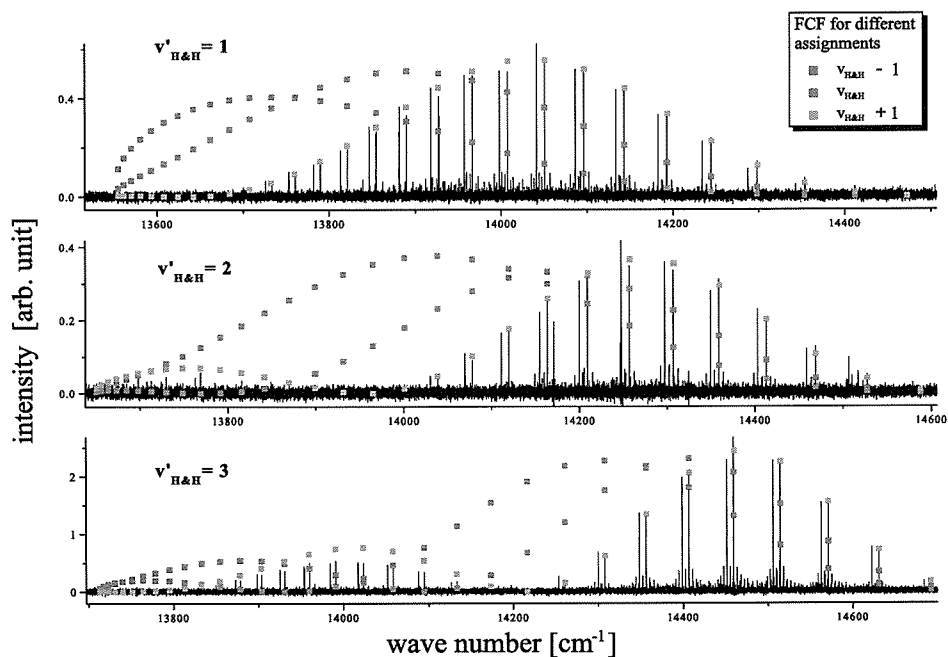


Figure 5.6: Comparison between observed spectra obtain by the excitation of the lower vibrational level $v_{\text{H\&H}} = 1, 2$ and 3 of the A state and Franck-Condon factors. Agreement is obtained for $v_{\text{A}} = v_{\text{H\&H}} + 1$.

assignments, and normalized to the most intense lines of each progressions. These comparisons are presented on the figure 5.6. For clarity the assignment corresponding to $v_{\text{H\&H}} + 2$ has been omitted on the picture. The best agreement is obtained for the assignment corresponding to $v_{\text{A}} = v_{\text{H\&H}} + 1$. Therefore the assignment for the A state should be revised. All vibrational levels observed should be numbered with one unit more.

Let us talk now about the c state vibrational numbering.

In the graphs of figure 5.7 the values of the effective rotational constant B_v of the lower observed vibrational levels are presented. The calculation of the rotational constant was made using a simplified Dunham expansion: $B_v \approx \Delta E / (4J' - 2)$. ΔE is the spacing between two consecutive observed rotational levels $J' - 2$ and J' . We see on the lower graph that the B_v -values of $v_{\text{A}} = 8$ develop towards the smaller B_v -value of the perturbing c state. The two lower perturbations are clearly visible and progressive. In their analysis Hofmann and Harris proposed the following assignment: the "downward" shift at the lowest J' -value of this $v_{\text{A}} = 8$ level is due to the level $v_{\text{c}} = 0$. Since they have not observed lower vibrational levels, they explained

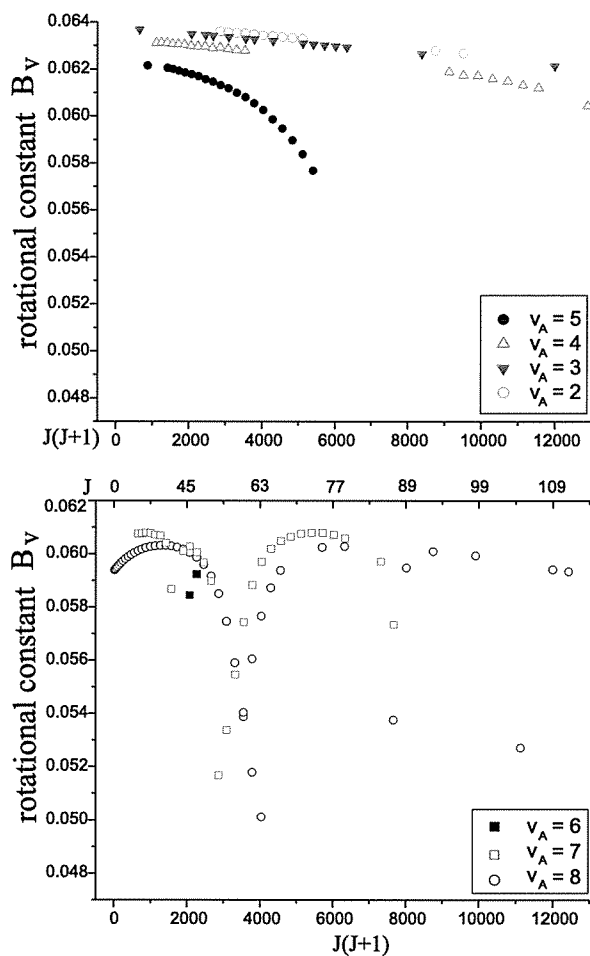


Figure 5.7: Rotational constant for the lower observed vibrational levels.

that this proposition should be understood as temporary. We have observed 6 lower vibrational levels than $v_A = 8$ and observed new local perturbations. In the same graph we see a decrease of the observed B_v -value of $v_A = 7$ and a level crossing at $J' = 57$ ($J'(J'+1) = 3306$). A smaller local perturbation is present for the same v_A for $J' = 39$. For the rotational constant of $v_A = 6$ we have little information, but we can see that the B_v -values are decreasing strongly with decreasing J' -values. It indicates the presence of a level crossing at $J' < 43$. Finally the decreasing of the B_v -value of $v_A = 5$ for $J'(J'+1)$ approaching 6000 ($J' \sim 77$) and of $v_A = 4$ for $J'(J'+1)$ approaching 12900 ($J' \sim 113$) indicate two additional local perturbations.

Considering the magnitude of possible perturbations for the levels $v_A = 3$ and 2, we could expect by a comparison with rotational constants of the

higher vibrational levels, the effects of perturbations should be visible on the observed levels, despite the gaps in the series of observed levels. But, such effects are not observed; therefore we conclude that these two lower observed levels are not locally perturbed. The same vibrational level of the c state, crossing $v_A = 4$ at high J' -values, causes the decrease of the B_v -value for $v_A = 5$. From this graph we conclude that these two local perturbations are the lowest ones in energy, and, therefore are caused by the level $v_c = 0$ of the $c^3\Pi_u$ ($\Omega = 0$) state.

We have constructed term energies with the observed transitions and the collected transitions from Hofmann and Harris by adding to them the term energies of the involved levels of the ground state potential derived in chapter II. The term energy of a level of the A state is obtained several times since observed spectrum consists of a transition progression from a selected upper level. We have averaged the transitions belonging to one spectrum weighted with their relative uncertainty. To the averaged relative uncertainty we have added the absolute uncertainty 0.009 cm^{-1} (see section 5.1.2) to obtain the experimental of one term energy. Then the term energies of the same levels from different recordings have been averaged, weighted with their experimental uncertainty. The data of Hofmann and Harris consist of P and R transitions for 340 levels of the A state. We have added the term energies of the ground state levels and averaged the two values obtained for each upper level with the same weight.

We have compared the data obtained by Hofmann and Harris to our own measurements. We calculated the differences between their and our term energies. It corresponds to 64 common levels. The mean difference between both data is -0.037 cm^{-1} and the standard deviation of the differences is 0.038 cm^{-1} . This standard deviation is larger than our experimental accuracy and the one claimed by Hofmann and Harris (0.01 cm^{-1}). Hofmann and Harris have recorded their spectra (of I_2 and Ca_2) by mode hopping through consecutive cavity modes (line width 0.0067 cm^{-1}), which were separated by 0.0167 cm^{-1} . The line width of the Iodine lines in the observed frequency range is in the order of 0.03 cm^{-1} . Thus they have very few points per lines. In addition they claimed that they needed to make interpolation of the order of 1 cm^{-1} between strong I_2 lines and the Ca_2 lines. It is thus difficult to believe that they reached effectively an experimental uncertainty of 0.01 cm^{-1} . Their experimental uncertainty is probably larger than they claimed and can explain for a great extend the standard deviation of the differences between the two data sets. Concerning the global shift, we only found that they used the I_2 atlas from 1978, which should be corrected by -0.0056 cm^{-1} compared to recent atlas. This value is not sufficient to explain the observed shift.

We decided to shift arbitrarily all the term energies from Hofmann and Har-

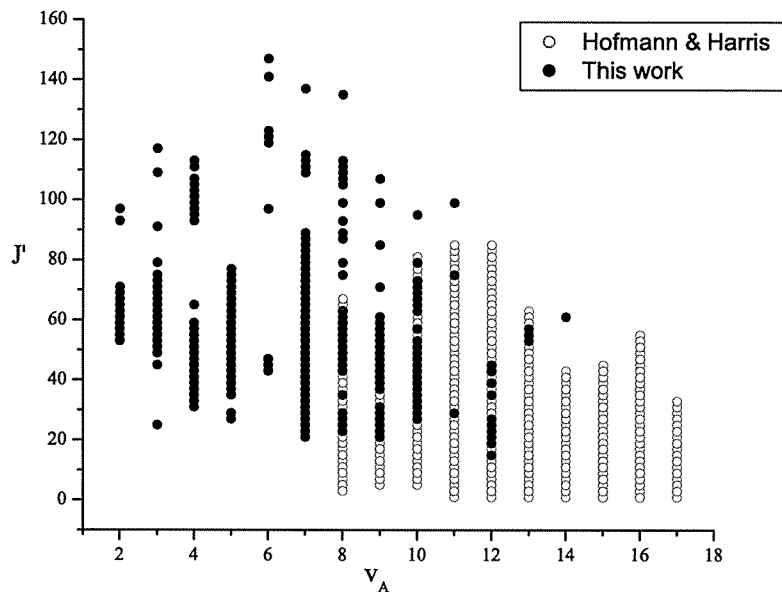


Figure 5.8: Range of quantum numbers of observed levels following the new assignment. The black dots are the observed levels in this work. The blue open circle are the data of Hofmann and Harris. Levels corresponding to extra lines have received the same vibrational quantum numbers as these of the A state levels.

ris by an amount of -0.037 cm^{-1} and to give to all of them an error of 0.038 cm^{-1} . We choose to remove from the data set of Hofmann and Harris the 64 common levels and to keep ours. The total data set consists of 503 term energies. The figure 5.8 gives the range of vibrational and rotational quantum numbers observed in this work and those observed by Hofmann and Harris. Extra lines at the strong local perturbations levels have been labeled with the same vibrational quantum numbers as these of the A state.

5.2 Theory

The body-fixed molecular Hamiltonian is given in a specific subspace of states by the following terms:

$$\hat{H} = V^{\text{BO}} + \hat{T}^{\text{N}} + \hat{H}^{\text{ROT}} + \hat{H}^{\text{rel}} \quad (5.1)$$

where V^{BO} are the Born-Oppenheimer potentials, solutions of the fixed-nuclei electronic Schrödinger equation, and \hat{T}^{N} is the nuclear kinetic energy operator without the rotational term, which is given by:

$$\begin{aligned}\hat{H}^{\text{ROT}} &= \frac{1}{2\mu R^2} [\hat{R}]^2 \\ &= \frac{1}{2\mu R^2} [(\hat{J}^2 - \hat{J}_z^2) + (\hat{L}^2 - \hat{L}_z^2) + (\hat{S}^2 - \hat{S}_z^2) + \\ &\quad \underbrace{(\hat{L}_+ \hat{S}_- + \hat{L}_- \hat{S}_+)}_{\text{Spin-electronic}} - \underbrace{(\hat{J}_+ \hat{L}_- + \hat{J}_- \hat{L}_+)}_{\text{L-uncoupling}} - \underbrace{(\hat{J}_+ \hat{S}_- + \hat{J}_- \hat{S}_+)}_{\text{S-uncoupling}}] \quad (5.2)\end{aligned}$$

We use the ladder operators $\hat{O}_{\pm} = \hat{O}_x \pm i\hat{O}_y$ in the molecule-fixed axis xyz where \hat{O} stands for \hat{J} , \hat{L} and \hat{S} , see [Lefebvre-Brion H. and Field R.W., 1986]. H^{rel} contains the spin-orbit interaction H^{SO} , the spin-spin interaction H^{SS} and the spin-rotation interaction H^{SR} .

We are interested in this section to derive the Hamiltonian matrix describing the $A^1\Sigma_u^+$ ($4s4s^1S + 4s3d^1D$), $c^3\Pi_u$ ($4s4s^1S + 4s4p^3P$), and the $a^3\Sigma_u^+$ ($4s4s^1S + 4s4p^3P$) coupled-state manifold (see figure 5.9). Other states dissociating at the asymptote $4s4s^1S + 4s3d^3D$ can couple to the considered states but they are lying above the triplet manifold according to the ab-initio calculations from [Czuchaj E. et al., 2003]. Their coupling will be much less pronounced because of no resonance effect, and thus will not be included in this analysis. The potentials we will derive will contain these small influences, and in this respect should be considered as effective potentials. One potential, the $^3\Pi_u$ ($^1S + ^3D$) is deep enough according to the ab-initio calculations to overlap with the A, c and a states. But this overlap appears at the very bottom part of $^3\Pi_u$, where the density of levels is small. Only occasional local perturbations can happen. Their magnitude are probably small, since the wave functions of the A or c states are oscillating faster than these of the bottom of the $^3\Pi_u$ in this overlapping region. Therefore we do not include this state in the analysis. We will check latter whether this approximation is justified.

5.2.1 Basis functions

In the Hund case (a) the angular momentum basis functions are: $|\alpha, J, S, \Omega, \Lambda, \Sigma \rangle$, where α stands for all other state labels (e.g. vibration, electronic configuration). We have seen in the section 2.2.2 that the ground state has only even values of J. Electronic dipole transition for $\Sigma \rightarrow \Sigma$ transitions obey the selection rules $\Delta J = \pm 1$, and for the (e_f) symmetry of the rotational levels the selection rules are $e \leftrightarrow e$ and $f \leftrightarrow f$ [Brown J.M. et al.,

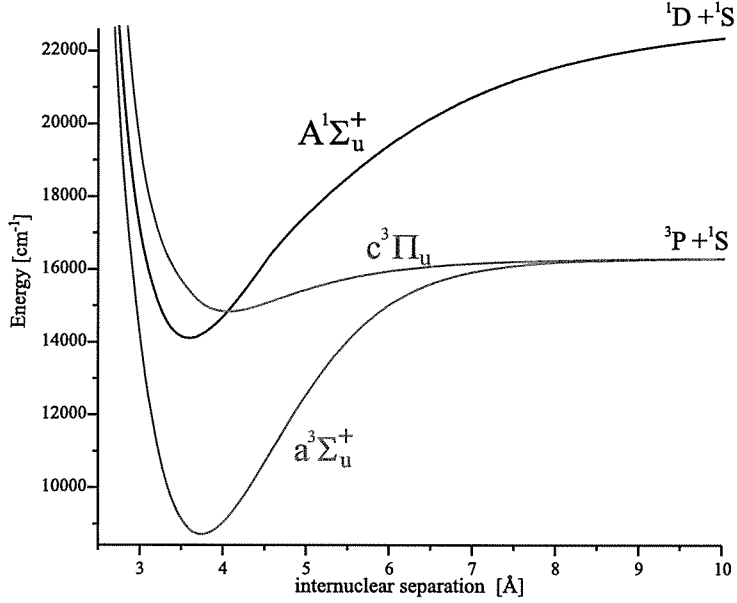


Figure 5.9: Schematic view of the Ca_2 potential curves involved in the present study.

1975]. In consequence only rotational levels with (e) symmetry have been observed for the $B^1\Sigma_u^+$ via the excitation from the ground state $X^1\Sigma_g^+$. In addition perturbation can occur only between levels of same (f) symmetry. Therefore, in the following we are only considering the subspace of levels with (e) symmetry. [Brown J.M. et al., 1975] defined (f) basis functions these with symmetry $(\pm)(-1)^J$ for molecules with even number of electrons. Thus, the properly symmetrized functions with (e) symmetry and odd value of J are the following (see [Lefebvre-Brion H. and Field R.W., 1986]):

$$|^{2S+1}\Lambda_\Omega, J, e \rangle = (2)^{-1/2}[|\alpha, J, \Lambda, S, \Sigma, \Omega \rangle - (-1)^{-S}|\alpha, J, -\Lambda, S, -\Sigma, -\Omega \rangle]$$

Thus the normalized wave functions for the five involved states are:

$$\begin{aligned} |A^1\Sigma_u^+, J, e \rangle &= |\alpha, J, 0, 0, 0, 0 \rangle \\ |c^3\Pi_u(0), J, e \rangle &= (2)^{-1/2}[|\alpha, J, 1, 1, -1, 0 \rangle + |\alpha, J, -1, 1, 1, 0 \rangle] \\ |c^3\Pi_u(1), J, e \rangle &= (2)^{-1/2}[|\alpha, J, 1, 1, 0, 1 \rangle + |\alpha, J, -1, 1, 0, -1 \rangle] \\ |c^3\Pi_u(2), J, e \rangle &= (2)^{-1/2}[|\alpha, J, 1, 1, 1, 2 \rangle + |\alpha, J, -1, 1, -1, -2 \rangle] \\ |a^3\Sigma_u(1), J, e \rangle &= (2)^{-1/2}[|\alpha, J, 0, 1, 1, 1 \rangle + |\alpha, J, 0, 1, -1, -1 \rangle] \quad (5.3) \end{aligned}$$

For simplicity the labels (e) and α will not be repeated hereafter.

5.2.2 Matrix elements

Selection rules

The main coupling operators are the spin-orbit \hat{H}^{SO} and the rotation \hat{H}^{ROT} . The selection rules for the matrix elements of \hat{H}^{SO} , (see [Lefebvre-Brion H. and Field R.W., 1986] table 2.2 and page 89), are:

$$\begin{aligned} \Delta J &= 0, \quad \Delta S = 0 \ (S \neq 0) \quad \text{or} \quad \Delta S = \pm 1 \\ \Delta \Omega &= 0, \quad \Delta \Lambda = \Delta \Sigma = 0 \quad \text{or} \quad \Delta \Lambda = -\Delta \Sigma = \pm 1 \\ g &\not\leftrightarrow u, \quad e &\not\leftrightarrow f, \quad \Sigma^+ \leftrightarrow \Sigma^- \end{aligned} \quad (5.4)$$

Consequently the $A^1\Sigma_u^+$ state couples to the $\Omega = 0$ component of the $c^3\Pi_u$ state. This interaction is responsible for the strong perturbations observed in the rotational energy ladder of the A state. The $a^3\Sigma_u^+$ ($\Omega = 1$) couples to the $c^3\Pi_u$ ($\Omega = 1$). The $\Omega = 0$ component of the $a^3\Sigma_u^+$ is not coupled to $c^3\Pi_u$ ($\Omega = 0$) state nor to the $A^1\Sigma_u^+$ state.

The coupling by the rotational interactions follows the selection rules $\Delta S = 0$, and depending on the considered term in \hat{H}^{ROT} , $\Delta \Omega = 0$ or ± 1 , meaning that only states within the same multiplicity can couple.

Diagonal matrix elements

For \hat{H}^{SO} :

$$\langle {}^{2S+1} \Lambda_\Omega, J | \hat{H}^{\text{SO}} | {}^{2S+1} \Lambda_\Omega, J \rangle = \Lambda \Sigma A(R) \quad (5.5)$$

and for \hat{H}^{ROT} :

$$\langle {}^{2S+1} \Lambda_\Omega, J | \hat{H}^{\text{ROT}} | {}^{2S+1} \Lambda_\Omega, J \rangle = \frac{\hbar^2}{2\mu R^2} \times [J(J+1) - \Omega^2 + S(S+1) - \Sigma^2] \quad (5.6)$$

Other terms of the relativistic Hamiltonian \hat{H}^{rel} can contribute to the energy, but with much smaller magnitude than the precedent ones. They are the spin-rotation interaction and the spin-spin interaction. An effective form of the spin-rotation Hamiltonian can be written as follows (see [Lefebvre-Brion H. and Field R.W., 1986]):

$$\hat{H}^{\text{SR}} = \gamma \hat{R} \cdot \hat{S} = \gamma(\hat{J} - \hat{L} - \hat{S}) \cdot \hat{S} \quad (5.7)$$

It gives:

$$\langle {}^{2S+1} \Lambda_\Omega, J | \hat{H}^{\text{SR}} | {}^{2S+1} \Lambda_\Omega, J \rangle = \gamma[\Sigma^2 - S(S+1)] \quad (5.8)$$

An usual form of the effective spin-spin Hamiltonian is:

$$\hat{H}^{\text{SS}} = \epsilon(3\hat{S}_z^2 - \hat{S}^2) \quad (5.9)$$

leading with $\Delta S = \Delta \Sigma = 0$ to:

$$\langle {}^{2S+1} \Lambda_{\Omega}, J | \hat{H}^{\text{SS}} | {}^{2S+1} \Lambda_{\Omega}, J \rangle = \epsilon(3\Sigma^2 - S(S+1)) \quad (5.10)$$

γ and ϵ depend on R.

Off-diagonal matrix elements

For \hat{H}^{SO} :

$$\langle c^3\Pi_u(0_u^+) | \hat{H}^{\text{SO}} | A^1\Sigma_u^+ \rangle = \chi(R) \quad (5.11)$$

$$\langle c^3\Pi_u(1_u) | \hat{H}^{\text{SO}} | a^3\Sigma_u(1_u) \rangle = -\zeta(R) \quad (5.12)$$

For \hat{H}^{ROT} we distinguish the different contributions of the rotational Hamiltonian.

The S-uncoupling operator is:

$$\hat{H}^{\text{JS}} = -\frac{1}{2\mu R^2}(\hat{J}_+\hat{S}_- + \hat{J}_-\hat{S}_+) , \quad (5.13)$$

it contributes as:

$$\begin{aligned} & \langle \alpha J, \Lambda, S, \Sigma, \Omega | \hat{H}^{\text{JS}} | \alpha J, \Lambda, S, \Sigma - 1, \Omega + 1 \rangle = \\ & 2 \times \frac{\hbar^2}{2\mu R^2} \times \sqrt{J(J+1) - \Omega(\Omega+1)} \times \sqrt{S(S+1) - \Sigma(\Sigma-1)} \end{aligned} \quad (5.14)$$

The spin-electronic term is:

$$\hat{H}^{\text{LS}} = \frac{1}{2\mu R^2}(\hat{L}_+\hat{S}_- + \hat{L}_-\hat{S}_+) , \quad (5.15)$$

it gives the contributions:

$$\begin{aligned} & \langle \alpha J, \Lambda, S, \Sigma, \Omega | \hat{H}^{\text{LS}} | \alpha J, \Lambda + 1, S, \Sigma - 1, \Omega \rangle = \\ & 2 \times \frac{\hbar^2}{2\mu R^2} \times \sqrt{S(S+1) - \Sigma(\Sigma-1)} \times L(R) \end{aligned} \quad (5.16)$$

And the L-uncoupling operator is:

$$\hat{H}^{\text{JL}} = -\frac{1}{2\mu R^2}(\hat{J}_+\hat{L}_- + \hat{J}_-\hat{L}_+) \quad (5.17)$$

it gives the contributions:

$$\begin{aligned} & \langle \alpha J, \Lambda, S, \Sigma, \Omega | \hat{H}^{\text{JL}} | \alpha J, \Lambda - 1, S, \Sigma, \Omega + 1 \rangle = \\ & 2 \times \frac{\hbar^2}{2\mu R^2} \times \sqrt{J(J+1) - \Omega(\Omega+1)} \times L(R) \end{aligned} \quad (5.18)$$

where we have the following matrix element from the \hat{L}_\pm operator:

$$L(R) = \langle \alpha J, \Lambda + 1, S, \Sigma, \Omega + 1 | \hat{L}_+ | \alpha J, \Lambda, S, \Sigma, \Omega \rangle \quad (5.19)$$

$$= \langle \alpha J, \Lambda, S, \Sigma, \Omega | \hat{L}_- | \alpha J, \Lambda + 1, S, \Sigma, \Omega + 1 \rangle \quad (5.20)$$

Finally we have the non-diagonal contribution of the spin-rotation Hamiltonian:

$$\begin{aligned} & \hat{H}^{\text{SR}} = (\gamma/2)(\hat{J}_+\hat{S}_- + \hat{J}_-\hat{S}_+) \\ & \langle \alpha J, \Lambda, S, \Sigma, \Omega | \hat{H}^{\text{SR}} | \alpha J, \Lambda, S, \Sigma - 1, \Omega + 1 \rangle = \\ & \gamma \sqrt{J(J+1) - \Omega(\Omega+1)} \sqrt{S(S+1) - \Sigma(\Sigma-1)} \end{aligned} \quad (5.21)$$

We apply the above calculation to the normalized wave functions given in (eq. 5.3)¹. It results in the 5-dimensions Hamiltonian matrix for the considered subspace of states, for a given J, and a fixed parity, shown on the following page:

We note $X = J(J+1)$, and $H_0^{(2S+1)\Lambda_\Omega} = \langle (2S+1)\Lambda_\Omega | \hat{H}^{\text{el}} + \hat{T}^{\text{N}}(R) | (2S+1)\Lambda_\Omega \rangle$ is the matrix element of the diabatic Hamiltonian, diabatic with respect to the spin-orbit and rotational couplings, for each state.

And with $\langle (2S+1)\Lambda_\Omega | \hat{H}^{\text{el}} | (2S+1)\Lambda_\Omega \rangle$ are the diabatic potentials $V^{\text{diab}}(R)$, and therefore $H_0^{3\Pi_u^0} = H_0^{3\Pi_u^1} = H_0^{3\Pi_u^2}$.

¹The factor 2 in the non-diagonal matrix elements cancel with the $1/\sqrt{2}$, which normalizes the wave functions

$$\begin{array}{cccc}
\Omega_A = 0 & \Omega_c = 0 & \Omega_a = 1 & \Omega_c = 2 \\
\left(\begin{array}{l}
H_0^{1\Sigma_u} \\
\chi(R) \\
0 \\
0 \\
0
\end{array} \right) & \left(\begin{array}{l}
\chi(R) \\
H_0^{3\Pi_u} - \gamma + \epsilon + \frac{\hbar^2}{2\mu R^2} X - A(R) \\
C_{JS}^{(0)} + C_{SR}^{(0)} \\
C_{JL}^{(0)} \\
0
\end{array} \right) & \left(\begin{array}{l}
0 \\
C_{JL}^{(0)} \\
C_{LS}^{(0)} - \zeta(R) \\
H_0^{3\Sigma^1} - \gamma + \epsilon + \frac{\hbar^2}{2\mu R^2} X \\
C_{JL}^{(2)}
\end{array} \right) & \left(\begin{array}{l}
0 \\
0 \\
C_{JS}^{(2)} + C_{SR}^{(2)} \\
C_{JL}^{(2)} \\
H_0^{3\Pi_u} + A(R) - \gamma + \epsilon + \frac{\hbar^2}{2\mu R^2} (X - 3)
\end{array} \right)
\end{array}$$

$$C_{LS} = \frac{1}{2\mu R^2} \sqrt{2L}(R)$$

$$C_{JL}^{(0)} = -\frac{1}{2\mu R^2} \sqrt{XL}(R)$$

$$C_{JS}^{(0)} = -\frac{1}{2\mu R^2} \sqrt{2X}$$

$$C_{SR}^{(0)} = \frac{\gamma}{2} \sqrt{2X}$$

$$C_{JL}^{(2)} = -\frac{1}{2\mu R^2} \sqrt{X - 2L}(R)$$

$$C_{JS}^{(2)} = -\frac{1}{2\mu R^2} \sqrt{2X - 4}$$

$$C_{SR}^{(2)} = \frac{\gamma}{2} \sqrt{2X - 4}$$

5.2.3 Fourier grid Hamiltonian method

The Fourier Grid Hamiltonian (FGH) method provides a precise way of calculating bound energy positions of coupled channels. It was formulated by [Kosloff R., 1988] and further developed by [Monnerville M. and Robbe J.M., 1994] and [Dulieu O. and Julienne P.S., 1995]. This method was applied successfully to the interpretation of the highly perturbed spectra in Rb₂ [Amiot C. et al., 1999] and for the determination of potential energy curves in the case of K₂ [Lisdar Ch. et al., 2001]. In these two papers, the perturbations induced by the spin-orbit coupling of the A¹Σ_u⁺ and the b³Π_u states², both dissociating to the first excited dissociation limit, were analyzed. We are concerned in our work by a similar situation, except that the A¹Σ_u⁺ and the c³Π_u states do not share the same asymptote, so that the spin-orbit coupling vanishes at large distances, instead of converging towards the atomic spin-orbit. The FGH was also employed and partly adapted to the description of long-range molecular states for the interpretation of strong perturbation effects in the photoassociation spectrum of Rb₂ at the 5s + 5p asymptote [Kokoouline V. et al., 1999].

The stationary radial Schrödinger equation for a diatomic system in the Born-Oppenheimer approximation is written as

$$\langle R | \hat{H} | \chi_{v,J}^\alpha \rangle = E_{v,J}^\alpha \langle R | \chi_{v,J}^\alpha \rangle, \quad (5.22)$$

where \hat{H} is given by equation 5.1 and $\langle R | \chi_{v,J}^\alpha \rangle$ is the wave function in the continuous radial representation. We have the normalization relation $\langle R | R' \rangle = \delta(R - R')$. The Schrödinger equation can be written again as

$$\langle R | [\hat{T}^N + \hat{V}] | \chi_{v,J}^\alpha \rangle = E_{v,J}^\alpha \langle R | \chi_{v,J}^\alpha \rangle \quad (5.23)$$

where we have inserted into \hat{V} all potentials and coupling energies. For a two-channel problem α and β , the potential operator writes $\hat{V} = \hat{V}^\alpha + \hat{V}^\beta + \hat{V}^{\alpha\beta}$. The basic principle of the method is to discretize the representation $| R \rangle$ into a finite grid of length L of N equally spaced points. We have the normalization and closure relation becoming:

$$\langle R_i | R_j \rangle = \delta(R_i - R_j) \quad (5.24)$$

$$\sum_j^N | R_j \rangle \langle R_j | = \mathbb{I} \quad (5.25)$$

²A small misprint is present in the title of the [Amiot C. et al., 1999]. ¹Σ_u⁺(0_u⁺) is written instead of ¹Σ_u⁺(0_u⁺).

Inserting the closure relation into the equation 5.22 on both side of the Hamiltonian and using the normalization relation one obtain.

$$\hat{H}_{ij} \chi_{v,J}^{\alpha}(R_j) = E_{v,J}^{\alpha} \chi_{v,J}^{\alpha}(R_j) \quad (5.26)$$

where we have the projections of the wave function as

$$\chi_{v,J}^{\alpha}(R_i) = \langle R_i | \chi_{v,J}^{\alpha} \rangle = \sum_j^N \delta(R_j - R_i) | \chi_{v,J}^{\alpha} \rangle \quad (5.27)$$

We obtain the $N \times N$ matrix representation of \hat{H} on the grid of points express as $\hat{H}_{ij} = \hat{T}_{ij}^N + \hat{V}_{ij}$. The potential energies of both electronic states $\hat{V}^{\alpha}(R)$ and the coupling interactions depends only on the variable R . \hat{V} is then a local operator and each matrix \hat{V}^{α} , \hat{V}^{β} and $\hat{V}^{\alpha\beta}$ are diagonal $N \times N$ matrix. The kinetic operator \hat{T}_{ij}^T is independent of R . Its a non-local operator and its matrix is non-diagonal. This operator is in fact local in the reciprocal momentum space. Its eigen-values onto the discrete reciprocal space momentum basis $\delta(P_i - P_j)$ are the local kinetic energy at R_i . The inverse Fourier transforms of these matrix elements are calculable [Kokoouline V. et al., 1999] and the results is given by:

$$\begin{aligned} T_{ii} &= \frac{h^2}{4\mu L^2} \frac{N^2 + 2}{6} \\ T_{ij} &= (-1)^{i-j} \frac{h^2}{4\mu L^2} \frac{1}{\sin^2[(i-j)\pi/N]} \quad \text{for } i \neq jA \end{aligned} \quad (5.28)$$

For the two channel problem ($\alpha\beta$) the formulation of the total Hamiltonian is express as :

$$\begin{pmatrix} H^{\alpha} & H^{\alpha\beta} \\ H^{\beta\alpha} & H^{\beta} \end{pmatrix} = \begin{pmatrix} T_d + V^{\alpha} & V^{\alpha\beta} \\ V^{\beta\alpha} & T_d + V^{\beta} \end{pmatrix} + \begin{pmatrix} T_{nd} & 0 \\ 0 & T_{nd} \end{pmatrix} \quad (5.29)$$

In the first matrix on the right side of the equation (5.29), each block is diagonal and in the second one the two blocks are non-diagonal. The generalization to a more channel problem is then straightforward, as it consists in building the corresponding kinetic and potential energy blocks, as well as the blocks for the coupling between the channels. The main advantage of the FGH method is now clearly express since the solution of the coupled channel problem is simply restricted to the diagonalization of the $2N \times 2N$ Hamiltonian matrix, which gives the $2N$ lowest eigenvalues of the coupled states and the eigenvectors on the grid of the N points.

Due to the sampling of the radial basis, variation of the wave function faster than the grid spacing ΔR cannot be reproduced. This puts conditions on the maximum value of the determinable wave number k_{max} . This is given by the Nyquist theorem summarize as: $k_{max} = \pi/(2\Delta R)$. Then we should ensure that the choice of grid spacing will be sufficient in order to reproduce the highest wave number in our physical situation. This is given by the difference between the highest energy and the lowest minimum of the involved potentials that I note ΔV . We should then implement the grid in order to have:

$$\Delta R \leq \pi \hbar / \sqrt{2\mu\Delta V} \quad (5.30)$$

This relation supposes that the wave function varies as a sine function. In the classically forbidden region it is not true since the amplitude of the wave function drops down exponentially. The accuracy of the calculated energies is then lower than we could expect from the Nyquist theorem solely. A parameter called β is then introduced to tune down the grid spacing to obtain the desired precision. Further development of the Fourier grid Hamiltonian method have been realized in the Orsay group [Kokoouline V. et al., 1999] to avoid implementation of very large grid to treat correctly the asymptotic region of potentials. In the present case, the collected data for the $A^1\Sigma_u^+ - c^3\Pi_u$ system in calcium dimer concerns the relatively deep bound region of the potentials and the need of such improvements of the method was not essential.

The FGH method allows the calculation of energy position of coupled channels for fixed potential. Our interest is to determine the potential energy curve and coupling strengths, which reproduce measured term energies within their experimental uncertainty. We need to combine to the FGH a procedure to fit the parameters of the modeled potentials and couplings to the observed data. The development of such procedure has been already realized in the frame of the collaborations between our group and O. Dulieu from the Orsay group and led to a satisfactory representation of the same coupled electronic state system in K_2 [Lisdat Ch. et al., 2001]. The minimization MINUIT routine from the CERN is employed for the adjustment of the parameters in the same way as presented section 2.3.1. To save a lot of computing time during the fit, eigenvectors of the matrix 5.29 are not calculated. The attribution of the calculated vibrational levels to the observed levels for a given J' -value is done by the closest approach. This may lead to wrong attributions when calculated levels are far from the observed ones. We implemented a routine which do the attribution by going through the list of calculated levels (for a given J') by two directions: from lower to high values, and reverse. The assignment, which gives the lowest standard deviation, is kept.

5.3 Deperturbation analysis

The term energies are located between 14600 cm^{-1} and 16272 cm^{-1} . The classical vibrational motion is then restricted from 3.08 \AA to 4.52 \AA for the A state and from 3.37 \AA to 8.65 \AA for the c state in the non-coupled picture. According to equation 5.30 a uniform grid of at least 123 points is required to represent properly the coupled states over a total internuclear interval ranging from 2.38 \AA to 10 \AA . This range is larger than the range of classical turning points in order to include the extension of the wave function into the classically forbidden region. The changes of values of the calculated term energies decrease with the decrease of the value of the parameter β . We observed that these variations become much smaller than our experimental accuracy for values of $\beta \leq 0.5$. With $\beta = 0.5$ the representation requires a 1235×1235 matrix for the 5-channel model. Since this matrix is diagonalized for each J of the data field at each iteration of the fit, the time needed to run one fit (typically 3000 iterations) can be rather long.

5.3.1 Two-states model

The first approach is to limit the manifold of states to the two surfaces $A^1\Sigma_u^+$ and $c^3\Pi_u(\Omega = 0)$ to reduce computational time, but also because we observed mainly levels of the A state. We have no direct observations of levels of the triplet state except for few perturbed levels, which have a significant singlet character ($> 15\%$). Using the perturbation-theory picture the other surfaces contribute at higher orders, since they are not directly coupled to the A state. They are coupled indirectly through $c^3\Pi_u(\Omega = 0)$ state. The matrix 5.22 reduces then to a 2×2 matrix.

Initial potential guesses

The problem to find the potential curves is rather complex, in the sense that the fitting procedure, which minimize the standard deviation $\sigma(p_1, p_2, \dots)$ (see eq. (2.12)), is a highly non-linear function of the free parameters p_i of the model. Furthermore, all the parameters of the fit are strongly correlated with one another. Therefore, we should start the fitting procedure with the simplest model possible to reduce the number of parameters. Another consideration is that the time of convergence of the fit depends critically on the initial guesses for the potential energy curves and the coupling. Therefore, we have constructed initial diabatic potentials, which follow as much as possible the observed rovibrational ladder. As we can see in the graph

5.10, the vibrational and rotational structure can be well identified for the A state (black dots). The constructed A state potential gives the levels represented by the blue dots. They follow the observed vibrational and rotational structure. For the c state, we have only the local perturbations to construct the initial potential. The rotational ladder of one vibrational level of the c state cross several rotational ladder of different vibrational levels of the A state at different J-values. This was used to estimate the rotational constants, and vibrational spacing to obtain an initial c state potential, and the corresponding rovibrational levels (red dots). By this we ensured that the level functions of both states cross at the observed local perturbations. The vibrational assignment achieved in section 5.1.3 has been used.

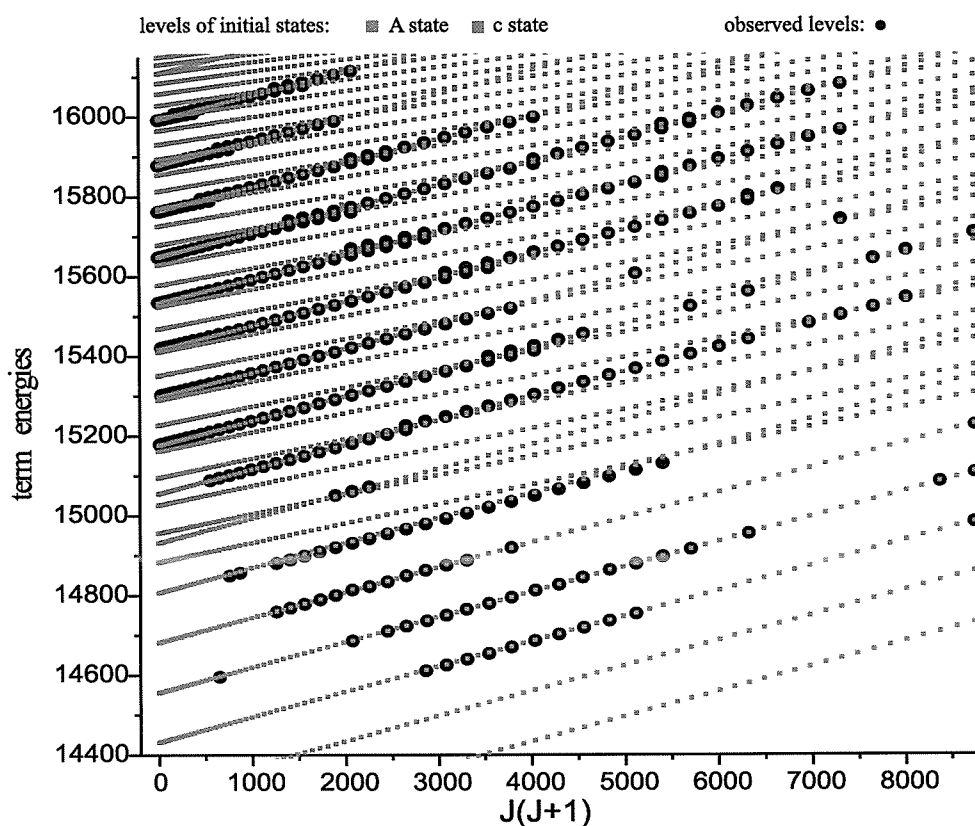


Figure 5.10: Observed term energies (thick dots) and level positions of the initial potentials for the A and c states. All odd and even J-values were plotted just to realize this picture to make the functional form more visible.

The coupling of the states lead to a global and a local shift of each level. Therefore, the construction of levels, which follow the observed position of

the term energies, in a regular rovibrational series, gives a rough estimation of the positions of the uncoupled levels. In a first iteration step, we used the coupled-channel Hamiltonian with a spin-orbit interaction χ to be independent of R . We fitted only this constant to improve the representation of all the observed levels. In this way we obtained a first guess of the magnitude of the shifts caused by coupling. These shifts have been subtracted to the observed term energies, which are not too perturbed. Then, the initial potential of the A state has been fitted to these roughly deperturbed levels. The obtained potential has been used again to improve the value of the spin-orbit parameter. The procedure has been repeated several times to improve iteratively the A state and the coupling. Then this method has been employed once for improving the c state using this time the strongly perturbed levels and the obtained value of χ . The initial potentials and the constant coupling give a standard deviation between observed and calculated levels $\bar{\sigma} = 170$. The improved potentials lead to a standard deviation of about $\bar{\sigma} = 110$.

I mention here that the levels observed by the filtered laser excitation technique have an experimental uncertainty smaller than those obtained by LIF and these of the Hofmann and Harris data set. Only the level $v_A = 5$ have been observed with this technique. In order to avoid a too high weight, for the fit, on a single vibrational level, we have increased their uncertainties to 0.030 cm^{-1} .

Constructed potential curves

The matrix 5.22 reduces to the 2×2 matrix ($\Omega_A = 0$ and $\Omega_c = 0$). The fitted potential $V_0^{\text{fit}}(R)$ for the $c^3\Pi_u$ ($\Omega = 0$) include the diagonal spin-orbit matrix element $A(R)$ since we cannot distinguish its contribution from the Born-Oppenheimer potential. Therefore, we have $V_0^{\text{fit}}(R) = V^{BO}(R) - A(R)$. The contribution of the spin-spin interaction and the spin-rotation interaction are expected to be small compared to the other contributions, and we can neglect them ($\gamma = \epsilon = 0$) at first. The representation of the initial potentials, mentioned previously, was obtained by the analytic expansion as described in section 2.3.1. We used 12 a_i parameters for the A state and 16 for the c state. The experience in our group, obtained by fitting potential surfaces with this choice of representation, shows that this manifold of parameters should allow correct descriptions of the potential curves, for the small range of observed vibrational levels and for the expected well behaved potentials (no shelf or double well structure, see ab-initio calculations from [Czuchaj E. et al., 2003]³). According to our experience the fixed parameter b in the

³The $^1\Sigma_u(1D + 1S)$ state in this publication is lying 2000 cm^{-1} above the $^3P + ^1S$ asymptote. The potential curve of a $^1\Delta_u(1D + 1S)$ state have a similar depth and shape as

function (2.9) should have a value lying between -0.6 and 0.3 for a good representation. This value was fixed to -0.57 for the A state and -0.2 for the c state. The short and long-range extrapolation functions are connected near the shortest and the largest classical turning points of the observed levels. For both potentials the short-range extrapolations are done by the same function:

$$V(R) = A + B/R^{10} \quad \text{for } R \leq R_{inn} \quad (5.31)$$

$R_{inn}^A = 3.080 \text{ \AA}$ for the A state and $R_{inn}^c = 3.369 \text{ \AA}$ for the c state.

The long-range extrapolations are obtained with the following functions, for the A state:

$$V(R) = D_e^A - C_5/R^5 - C_6/R^6 - C_8/R^8 \quad \text{for } R \geq R_{out} = 4.511 \text{ \AA} \quad (5.32)$$

and for the c state:

$$V(R) = D_e^c - C_6/R^6 - C_8/R^8 \quad \text{for } R \geq R_{out} = 8.608 \text{ \AA} \quad (5.33)$$

The dissociation limits $D_e^{A/c}$ are calculated with respect to the ground state dissociation energy $D_e^X = 1102.074(9) \text{ cm}^{-1}$.

$D_e^A = \Delta E(^1D + ^1S) + D_e^X = 21849.634 + 1102.074 = 22951.708(9) \text{ cm}^{-1}$ and $D_e^c = \Delta E(^3P_1 + ^1S) + D_e^X = 15210.063 + 1102.074 = 16312.137(9) \text{ cm}^{-1}$

The atomic transition energies are taken from the reference [S. Bashkin and J.O. Stoner, 1978].

Spin-orbit coupling

For the spin-orbit coupling $\chi(R)$ of $A^1\Sigma_u^+$ with $c^3\Pi_u$ there are no published ab-initio calculations that we could use and model by mathematical functions. We only know that $\chi(R)$ vanishes for large internuclear separations since the atomic spin-orbit interaction between the $(4s4p)^3P$ state and the $(4s3d)^1D$ state is zero for reason of parity. We have then to guess the function, which will model the interaction. We started the fit with a constant coupling, which does not have the proper behavior at large internuclear distances but allows representing the coupling with only one parameter. It simplifies the representation, and permits to improve by fitting the shape of the potentials before introducing a more complex function with more parameters to adjust. This approximation can be justified by the fact that the range of internuclear distances for the limited data set is small and located at fairly short distance.

the A state potential. There is probably some inversions of electronic symmetry concerning the calculated states from [Czuchaj E. et al., 2003].

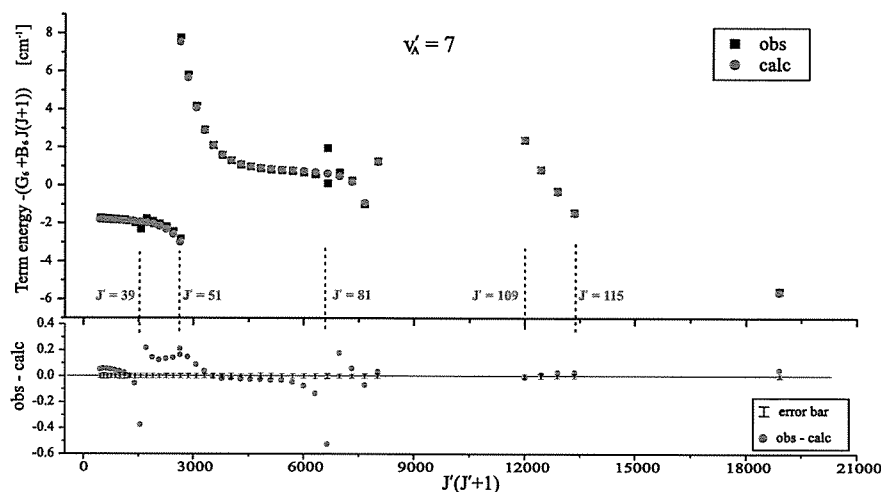


Figure 5.11: Upper graph: Observed and calculated term energies minus the regular $G_{v_A=7} + B_{v_A=7} J'(J'+1)$ behavior for the 2-states model. Lower graph: Observed minus calculated term energies together with the experimental error.

Result of the fit

With the 2-states model, we obtained a normalized standard deviation of the fit of $\bar{\sigma} = 4.08$. This represents an important improvement compared to the situation with the initial potential guesses, which were giving $\bar{\sigma} = 110$. The derived value of the spin-orbit coupling $\chi = 36.46 \text{ cm}^{-1}$ is of the same magnitude as the spin-orbit splitting between the 3P_1 and the 3P_2 atomic states $2A_0 = 105.88 \text{ cm}^{-1}$.

The positions and magnitudes of the strong perturbations are well reproduced for all observed vibrational levels. Let us exemplify the achieved quality of the description by taking the rotational levels of $v_A = 7$ and $v_A = 12$. In the upper parts of figures 5.11 and 5.12, deviations from a regular rotational behavior of the A state levels for the observed and calculated term energies are plotted. In the lower parts, the difference between observed and calculated term energies together with the experimental error bars, are presented. We see that the deviations at the main local perturbations (around $J' = 51, 109$ and 115 for $v_A = 7$; around $J' = 37, 63$ and 75 for $v_A = 12$), which are in the order of 8 or 10 cm^{-1} , are reduced to $0.2 \sim 0.4 \text{ cm}^{-1}$. Most of the residuals are within or in the order of the error bars. It is a significant improvement compared to the initial situations.

Nevertheless, the quality of the representation of the observed levels is not satisfactory. The residuals at the strong perturbations are still ten times

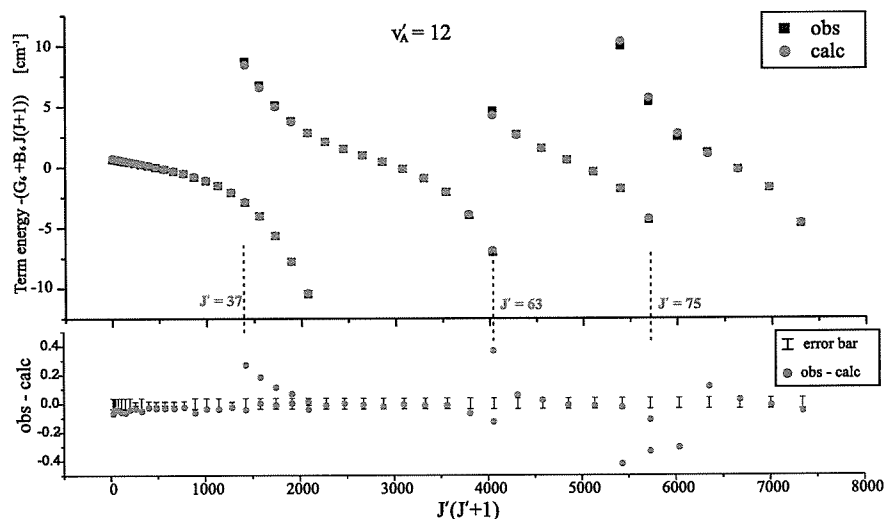


Figure 5.12: Upper graph: Observed and calculated term energies minus the regular $G_{v_A=12} + B_{v_A=12} J'(J'+1)$ behavior for the 2-states model. Lower graph: Observed minus calculated term energies together with the experimental error.

larger than the experimental error. Some contributions to the level shifts are not yet taken into account in the 2-surface model. In addition, the perturbations of smaller amplitudes, which are observed at several positions in the data set are not described at all (for instance around $J' = 39$ and 81 for $v_A = 7$). Such "secondary" local perturbations appear between two consecutive vibrational levels of the ${}^3\Pi_u(\Omega = 0)$ state, therefore cannot be caused by this state. These features show that the model is incomplete. It is necessary to introduce the ${}^3\Pi_u(\Omega = 1)$ surface in the model.

5.3.2 Three-surfaces model

Potentials and couplings

We add to the coupled channel calculations the third state $c^3\Pi_u(\Omega = 1)$. The contribution of the spin-orbit diagonal element $A(R)$ can be distinguished now from the Born-Oppenheimer potential, therefore it has been explicitly included in the 3×3 Hamiltonian matrix. There are effectively two potentials, and thus no additional parameters for the representation of the $c^3\Pi_u(\Omega = 1)$ state is needed, since: $V_1^{fit}(R) = V_0^{fit}(R) + A(R) = V^{BO}(R)$. The only additional parameters concern the model for the diagonal spin-orbit coupling

$A(R)$:

$$A(R) = A_0 + \frac{A_6}{R^6} + \frac{A_{12}}{R^{12}} \quad (5.34)$$

where A_0 , A_6 and A_{12} are free parameters. This functional form assures to approach a constant value for large internuclear distances being the atomic one of the manifold 3P .

In the 3-surface matrix, the $a^3\Sigma_u^+$ ($\Omega = 1$) state is not included. The spin-orbit and the rotational couplings (the $C_{LS}^{(0)} - \zeta(R)$ matrix element) between the $^3\Pi_u(\Omega = 1)$ state and the $a^3\Sigma_u^+$ ($\Omega = 1$) state are thus neglected. This is justified at relatively short internuclear separations where the energy spacing between the two potentials is large compared to $|\zeta(R)| \approx A(R) \approx 52.94 \text{ cm}^{-1}$. The energy spacing is approximately 5600 cm^{-1} at the internuclear distance where the $c^3\Pi_u$ state cross the $A^1\Sigma_u^+$ state [Busserly-Honvault B. et al.,]. But at large internuclear distance the Born-Oppenheimer potentials of the $^3\Pi_u$ and the $^3\Sigma_u$ converge diabatically to the same asymptote, and at infinite R they are degenerate. The effect of the coupling between the diabatic potentials, which breaks the degeneracy, changes the shape of the potentials. The adiabatic behavior of the $^3\Pi_u(\Omega = 1)$ should be taken into account. The diagonalization of the 2×2 potential matrix will allow getting a good approximation for the adiabatic potential:

$$\begin{pmatrix} V_0^{\text{fit}} + A(R) & C_{LS}^{(0)} - \zeta(R) \\ C_{LS}^{(0)} - \zeta(R) & V_{\text{diab}}(^3\Sigma_u) \end{pmatrix} \quad (5.35)$$

$\zeta(R)$ was approximated by $\zeta(R) = -A(R)$, $A(R)$ is given by equation (5.34). $C_{LS}^{(0)}$ is small compared to $A(R)$, therefore it was neglected. We have used the ab-initio potential of the $a^3\Sigma_u^+$ state from [Busserly-Honvault B. et al.,]. It was smoothly extended to the center $^3P + ^1S_0$ asymptote by the dispersion functions $-C_6/R^6 - C_8/R^8$. This state is attractive. Therefore, the adiabatic $a^3\Sigma_u^+$ ($\Omega = 1$) state converges to the $^3P_1 + ^1S_0$ asymptote, and the adiabatic $^3\Pi_u$ ($\Omega = 1$) state correlates to the $^3P_2 + ^1S_0$ asymptote see figure 5.13.

We have still a 3-surface model, therefore the dynamical effects caused by the $a^3\Sigma_u^+$ ($\Omega = 1$) are not included. The change from the diabatic potential to the adiabatic potential of the $^3\Pi_u(\Omega = 1)$ has an effect on the quality of the fit, which is not negligible.

Result of the fit

The potentials obtained previously with the 2-surface model are used as starting point for the fit.

The standard deviation achieved by fitting with the 3 states is $\bar{\sigma} = 1.913$. It

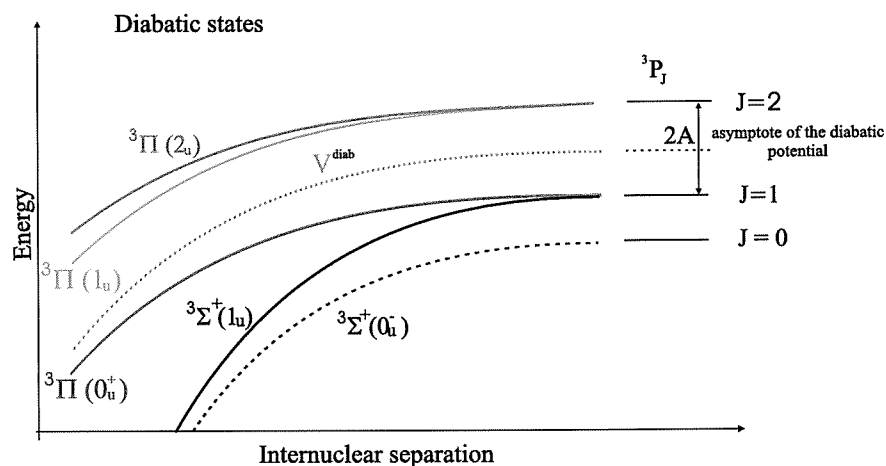


Figure 5.13: Adiabatic potential of u-symmetry states correlated to the ${}^3P + {}^1S$ asymptote.

shows that the global description is clearly improved. The obtained value of the spin-orbit coupling $\chi = 36.51 \text{ cm}^{-1}$ is almost equal to the value obtained with the 2-surface model. We take again the rotational ladder of $v_A = 7$ to show the improvements of the representation, figure 5.14. The description of the strong perturbations is better. The magnitude of the residuals has been reduced by a factor two. The secondary local perturbations, which were not reproduced previously, are now better described. Their residuals have been significantly reduced (by a factor 10 for $v_A = 7$, $J' = 39$ for instance). The calculation of the mixing fractions of the different states shows that the ${}^3\Pi_u(\Omega = 1)$ character is not negligible for such levels, and even higher than the ${}^3\Pi_u(\Omega = 0)$ mixing percent. Anyway we see in the lower graph of figure 5.14 that there are still some trends in the representation. It concerns the highly perturbed levels. Their residuals exceed the error bars. Additionally, we observed few levels (less than 10), residuals of which exceed the experimental uncertainty by a factor of 3 to 10. Their residuals are not following the trends of the residuals of the neighbor rotational levels 5.16.

5.3.3 Four-surface model

Including the $c^3\Pi_u(\Omega = 2)$ leads to a very small enhancement of the global quality. The achieved standard deviation is $\bar{\sigma} = 1.83$. The trends observed with the 3-surface model at the local perturbations remain. Few occasional levels, which are perturbed by a neighboring level of the ${}^3\Pi_u(\Omega = 2)$, are better represented. It is the case, for instance, for the level $J' = 39$ and

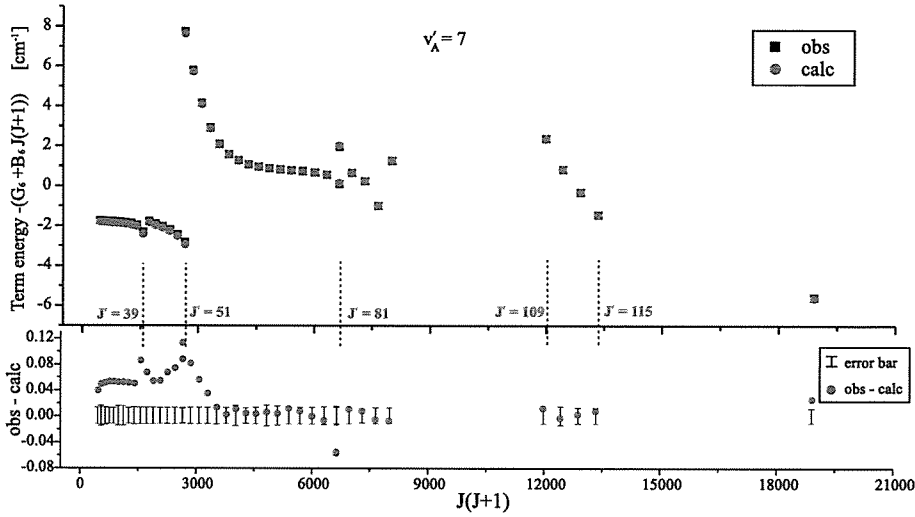


Figure 5.14: Upper graph: Observed and calculated term energies minus the regular $G_{v_A=7} + B_{v_A=7} J(J+1)$ behavior for the 3-states model. Lower graph: Observed minus calculated term energies together with the experimental error.

for the two levels with $J' = 81$ for $v_A = 7$ as we can see in figure 5.15. Their residuals are now within the error bars. The calculation of the mixing fractions of the different states confirms that the ${}^3\Pi_u(\Omega = 2)$ character is not negligible for such levels ($\sim 1\%$). We have fitted the parameter γ of the spin-rotation interaction as a constant with respect to the internuclear distance. The improvement given by the release of this parameter is marginal. The obtained value is $1.97 \times 10^{-3} \text{ cm}^{-1}$, which is small compared to A_0 , and compared to the rotational constant of the c state ($\sim 0.05 \text{ cm}^{-1}$). To neglect the variation of γ with the internuclear distance was then justified. We kept the parameter ϵ from the spin-spin interaction to zero, since it will only be effectively a very small change of the spin-orbit splitting between the triplet states.

The few levels mentioned in the previous section, which have a larger residual than neighboring rotational levels of the same v_A , are not better described by the inclusion of the $c^3\Pi_u(\Omega = 2)$ state into the coupled channel calculations (compared to figure 5.16). These levels belong to the data set from Hofmann and Harris. The coupled-channel calculation shows that most of these levels have mainly triplet character (c). Consequently, the intensity of the lines involving these levels are expected to be weaker than the intensity of the lines coming from a level with mainly singlet character (A). The ratio of both intensities $\sim (C_s^A)^2 / (C_s^c)^2$, where $C_s^{A/c}$ are the percentage of singlet

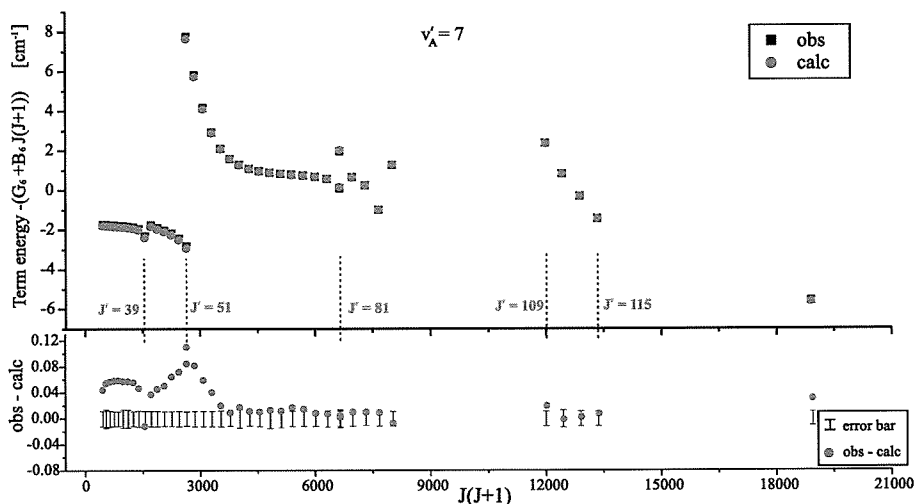


Figure 5.15: Upper graph: Observed and calculated term energies minus the regular $G_{v_A=7} + B_{v_A=7} J(J+1)$ behavior for the 4-states model. Lower graph: Observed minus calculated term energies together with the experimental error.

state in the wave function, is similar or smaller than the signal-to-noise ratio of the spectra obtain by Hofmann and Harris (SNR taken from a spectra shown in [Hofmann R. T. and Harris D. O., 1986]). Therefore, it is possible that these lines have been not properly assigned.

We have checked also whether these higher deviations could be caused by the $a^3\Sigma_u^+$ ($\Omega = 1$) state. We included this state into the coupled-channel calculations, using the potential from [Czuchaj E. et al., 2003]. We have set the spin-orbit coupling to $-\zeta(R) = A(R)$. The matrix element $L(R)$, equation 5.19, have been approximated to its asymptotic value: $L(R) = \sqrt{2}$. No fit has been tried, only the calculation of the level positions of the five coupled states have been performed (see the complete matrix 5.22). First, we observed no improvement on the overall description of the observed levels. Second, this surface does not produce shifts of levels of similar magnitudes as the residuals. In fact, this surface causes dynamical changes only to the levels with a significant $c^3\Pi_u$ ($\Omega = 1$) character, which are closed to the asymptote. These changes are very small, compared to the experimental uncertainty. Therefore, we cannot conclude that neither the small trends in the residuals nor the few numbers of larger residuals are caused by the $a^3\Sigma_u^+$ ($\Omega = 1$) state.

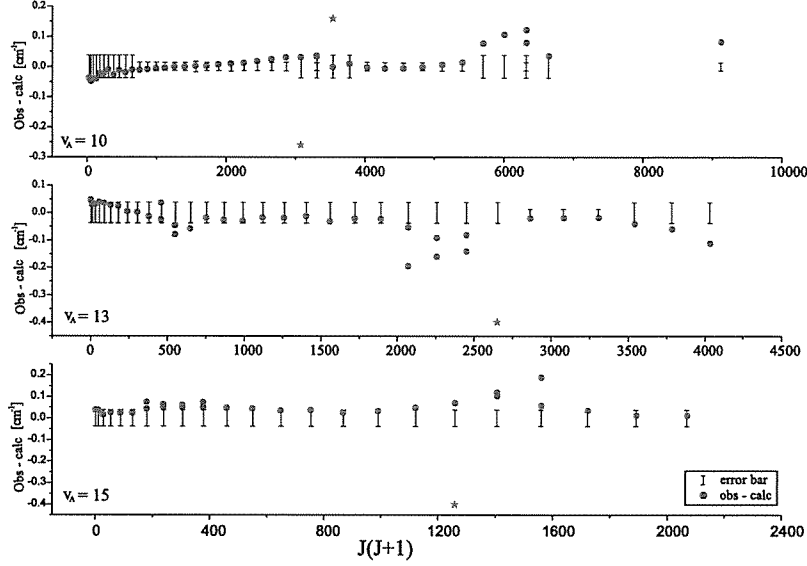


Figure 5.16: Residuals and error bar for the $v_A = 10, 13, 15$. The few residuals, which do not show the same behavior as the other are plotted with a blue star.

5.3.4 Variations of the spin-orbit coupling

We tried different functional forms of $\chi(R)$, which vanish at large R , to get some experience about the influence of the variation of the coupling.

We used:

$$\chi^1(R) = \chi_1 R^{-1} + \chi_3 R^{-3} + \chi_5 R^{-5} + \chi_7 R^{-7} \quad (5.36)$$

and

$$\chi^2(R) = \chi_1 e^{-\epsilon R} + \chi_2 e^{-2\epsilon R} + \chi_3 e^{-3\epsilon R} + \chi_4 e^{-4\epsilon R} \quad (5.37)$$

and

$$\chi^3(R) = [\chi_1(R - R_c) + \chi_2(R - R_c) + \chi_3(R - R_c) + \chi_4(R - R_c)] \times 1 / (1 + e^{\epsilon(R - R_s)}) \quad (5.38)$$

$\epsilon > 0$, R_c is a fixed parameter, R_s is a cutting at large R

The value of the function can become too large at very short distance for the first two functions. Therefore, we have introduced a cutoff at 3 \AA . The results we obtained were not better with the functions $\chi^1(R)$ and $\chi^2(R)$. They are not allowing a better representation compared to a constant coupling. But we observed that each choice of functions gives fitted potentials, which have different shapes, not only in the energy region where the A and c state

potentials overlap, but also in the lower part of the A state. This shows that the coupling and the potentials are strongly correlated. We observed for the lower vibrational levels ($v_A = 2, 3, 4$) systematic trends, figure 5.17 shows examples.

For the $\chi^{1/2}(R)$ types of coupling, the difference between the observed and calculated term energies for the rotational series of $v_A = 2$ and $v_A = 4$ are systematically larger than the experimental error bars. The rotational behavior is not satisfactorily described. We see a slight dependence of the residuals with the J-value. For $v_A = 2$ they decrease and for $v_A = 3$ and 4 they increase with J. The representation with the constant coupling is better. The tendency in function of the J-values differs for $v_A = 2$, and are less pronounced for all considered v_A . The residuals are within the error bars for $v_A = 3$. Therefore, one would keep the representation of the coupling by a constant value since it gives deviations with less systematic trends. These trends in the residuals seems to indicate that a coupling function decreasing slower with R than the function $\chi^{1/2}(R)$ would give some improvement. The last fit performed including the function χ^3 shows a slight decrease of the standard deviation compared to the fit with a constant coupling.

5.4 Discussion

5.4.1 Verification of approximations in the model

We have made several approximations or assumptions in the couple-channel calculations that should be checked.

- We have shifted the data of Hofmann and Harris by -0.037 cm^{-1} (see section 5.1.2). To check whether this could limit the quality of the representation, we have fitted this shift as an additional parameter in our model. The description is slightly better with a shift of -0.029 cm^{-1} instead of -0.037 cm^{-1} . The decrease of the standard deviation is less than a percent. The trends in the residuals remain. Therefore, this correction does not provide a significant improvement. This is understandable since this correction is smaller than the experimental uncertainty we set for the data set of Hofmann and Harris.
- We selected the range of internuclear distances as $[2.38 \text{ \AA} - 10 \text{ \AA}]$ for establishing the grid points for the Fourier grid Hamiltonian. This implies that levels lying at higher energy than the potential energy at these two internuclear distances are included in the model as box states. The position of levels of the c state close to the asymptote are the most

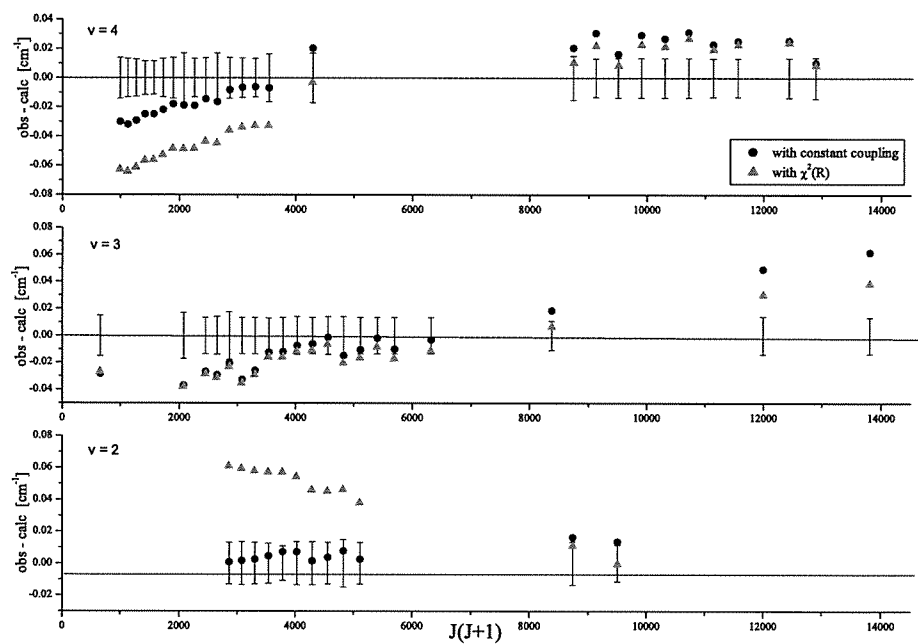


Figure 5.17: Observed minus calculated term energies of the lower v_A depending on the choice of coupling functions, constant or exponentially decreasing $\chi^2(R)$ functions. Experimental error bars are plotted to be able to identified acceptable and non-acceptable deviations.

affected ones by this approximation, as well as the continuum levels. The exact position of the continuum states is not of importance, since they are separated to the highest observed levels by an energy at least equal to the magnitude of the spin-orbit coupling. Therefore they are weakly coupled to the A state levels. But we should check whether the increase of the density of states by enlarging the range of internuclear distance may have a non-negligible influence by a cumulative effect. The increase of the range by a factor two, allowing a better description of the highest bound levels of the c state and an increase of the density of its continuum states by a factor of roughly 4, does not show any significant change in the quality of the representation of the observed set of data.

The assignment of the vibrational numbering of the A state have been checked by calculating the Franck-Condon factors with the determined potential energy curve and compared with intensity pattern of observed fluorescence spectra. The agreement is still good and even better than obtain previously in figure 5.6.

5.4.2 Comparison with the previous study

Hofmann and Harris have carried out a local deperturbation analysis, representing the energy positions of the rovibrational levels of the $A^1\Sigma_u^+$ and $c^3\Pi(0_u^+)$ states by Dunham expansions and a coupling parameter for each local perturbations. They included several perturbing levels above and below each A state vibrational level (in average 6 vibrational levels). The coupling to each of these perturbing levels necessitated three additional adjustable parameters. It resulted to this approach that a large number of parameters was necessary to reproduce their observed data (81 parameters). They achieved a quality of the representation of $\sigma = 0.13 \text{ cm}^{-1}$. They have included the effect of a $c^3\Pi(1_u)$ level for two instances in their fits.

In the present, we have used a global deperturbation analysis via the coupled-channel calculations. We have achieved a quality of the description $\sigma = 0.055 \text{ cm}^{-1}$ for an average experimental uncertainty of 0.03 cm^{-1} , with a number of parameters lower than Hofmann and Harris (44 parameters), and for a larger data set (6 vibrational levels more).

5.4.3 Predictions

Bondybey and English have presented in their publication [Bondybey V. E. and English J.H., 1984] an excitation spectrum of low resolution of the

region 14470 cm^{-1} to 15200 cm^{-1} obtained by time-resolved laser induced fluorescence in a pulsed supersonic jet. A copy of the spectrum is presented in figure 5.18. They have identified progression bands $v_A \leftarrow v''=0$ and $v_A \leftarrow v''=1$. These bands are labeled as v_A and v_{A1} with black numbers in the figure. The numbering have been corrected due to the new assignment achieved in the present study. Several bands observed in this spectrum have not been identified by Bondybey and English. Applying our results from the deperturbation analysis, we can now assign these bands. They are excita-

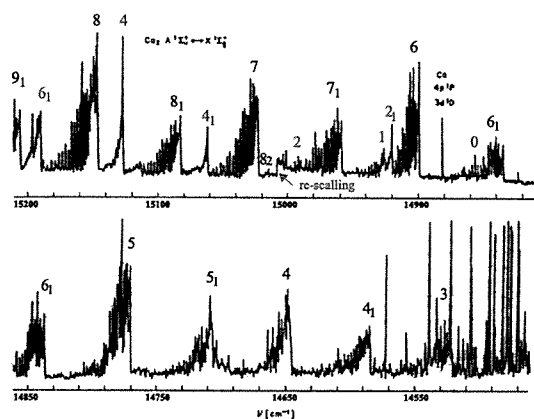


Figure 5.18: Overall scan of the $\text{Ca}_2\text{ A}^1\Sigma_u^+ - \text{X}^1\Sigma_g^+$ excitation spectra obtained by Bondybey and English. Bands are labeled with the v' values and with the v'' value as subscript when $v'' \geq 1$. A rescaling of the spectrum below 15100 cm^{-1} have probably be carried out, although it is not mentioned in the publication of Bondybey and English.

tions of the $c^3\Pi_u (\Omega = 0) - \text{X}^1\Sigma_g^+$ transitions. We have marked them by red numbers in the spectrum. The $c^3\Pi_u$ state being metastable, the levels, which can be efficiently excited, have significant mixing with the $\text{A}^1\Sigma_u^+$ state. The graphs in figure 5.19 display the percentage of A state character in the vibrational functions of the c state levels for $J' = 1, 25, 45$. We consider these low J , since in a supersonic jet only the low rotational levels are ther-

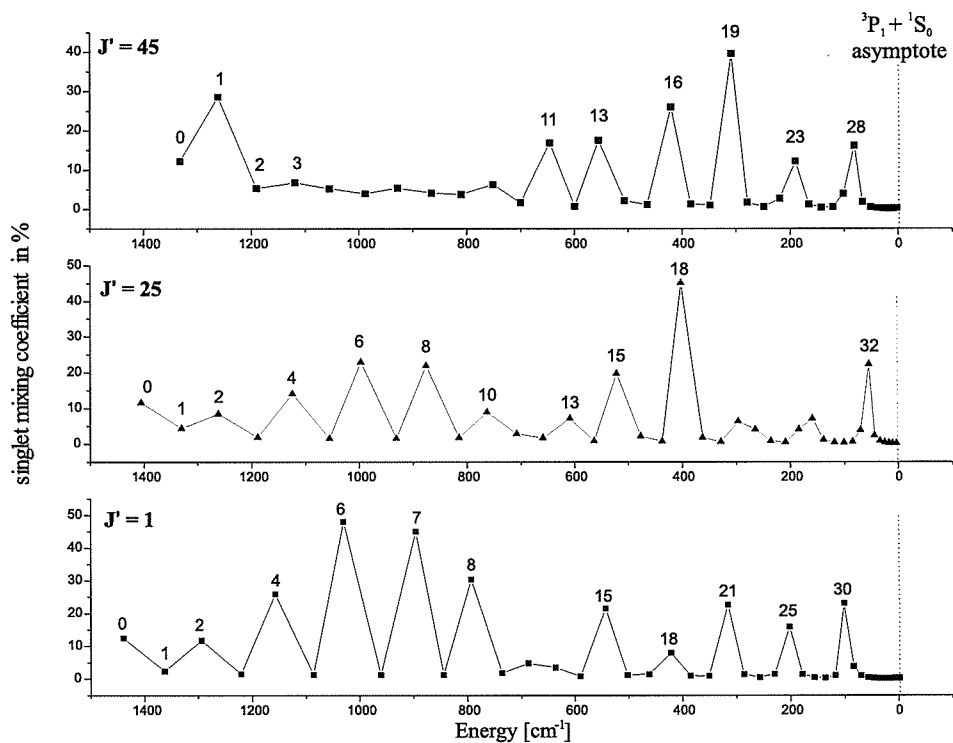


Figure 5.19: A state character of the c state levels as function of the binding energy. By convention we attribute a level to the c state when the percentage of c state character is higher than 50%.

mally populated. With the temperature Bondybey reported (40 K - 70 K) the maximum of population occurs around $J'' = 18 - 24$. We see that the A state character is important for the low vibrational levels with an even numbering. This is why in the spectra, we observe the band heads of $v_c = 2, 4$ and 6 . The mixing of A state decreases for these levels as the J' -value increases. This dependence on J' and the fact that the rotational constant of the c state is similar to the one of the ground state, explain why the bands appear very sharp. We see in figure 5.19 that the percentage of A state for the low vibrational levels with an odd number increases significantly only for $v_c = 1$. The bands with $v_c = 1$ are thus present in the spectra. Bands from higher v_c can also be observed.

5.5 Conclusion

We have treated the coupled $A^1\Sigma_u^+$ and $c^3\Pi_u$ electronic states applying the Fourier grid Hamiltonian method combined with a fitting procedure. This global approach has allowed a satisfactory deperturbation of the coupled system providing diabatic potential energy curves and spin-orbit interactions. The observed perturbations in the spectra of the $A^1\Sigma_u^+ - X^1\Sigma_g^+$ system are well described. Small trends between observed and calculated levels compared to their observed splittings remain. We have included in the description all the states, which have a significant contribution to the representation. We have shown that the few approximations we made are justified. Therefore, we consider that the model we used is complete. We believe that the representation can be further improved having a better model for the variation of the spin-orbit coupling with internuclear separation. Tables of parameters for the potentials and the coupling can be found in appendix A. Using these parameters give a standard deviation of $\bar{\sigma} = 1.83$.

To further improve the potential energy curves and to obtain more precise coupling functions, it is necessary to collect more data on the lower levels of the A state, which are less perturbed. The observation of the vibrational levels $v_A = 0$ and 1 will fix the minimum position of the A state. Significant improvement of the triplet surfaces would be reached by observing directly transitions involving c state levels with higher triplet character. The fact that bands belonging to the $c^3\Pi_u (\Omega = 0) - X^1\Sigma_g^+$ have been observed by Bondybey and English (see figure 5.18) is a good indication that the observation of the c state levels with a relatively low A state character can be observed in a molecular beam with high resolution laser spectroscopy. To collect more precise data on the $A^1\Sigma_u^+$ and $c^3\Pi_u$ states will help to reduce the correlations between the parameters of the potentials and of the spin-orbit coupling for the deperturbation analysis.

The observation of the last bound levels of the $c^3\Pi_u (0_u^+)$ state in a beam is more difficult due to the fast decreasing of the A state character as shown in figure 5.20. A larger time of observation than possible with the fast molecules in beam is necessary. In this respect, photoassociation spectroscopy on trap Ca atoms on the $^3P_1 - ^1S_0$ transition will give better results (see the case of Sr by [Katori H.,]). The asymptotic levels of the $a^3\Sigma_u^+ (1_u)$ can be observed in the photoassociation spectra. The combination of the data from the beam and from the photoassociation experiment will then allow a precise description of the dynamics of the cold collisions at the triplet asymptote.

Only one example of a global deperturbation analysis exists on a similar system. It concerns the $A^1\Sigma_u^+$ and $b^3\Pi_u$ coupled states of the K_2 molecule

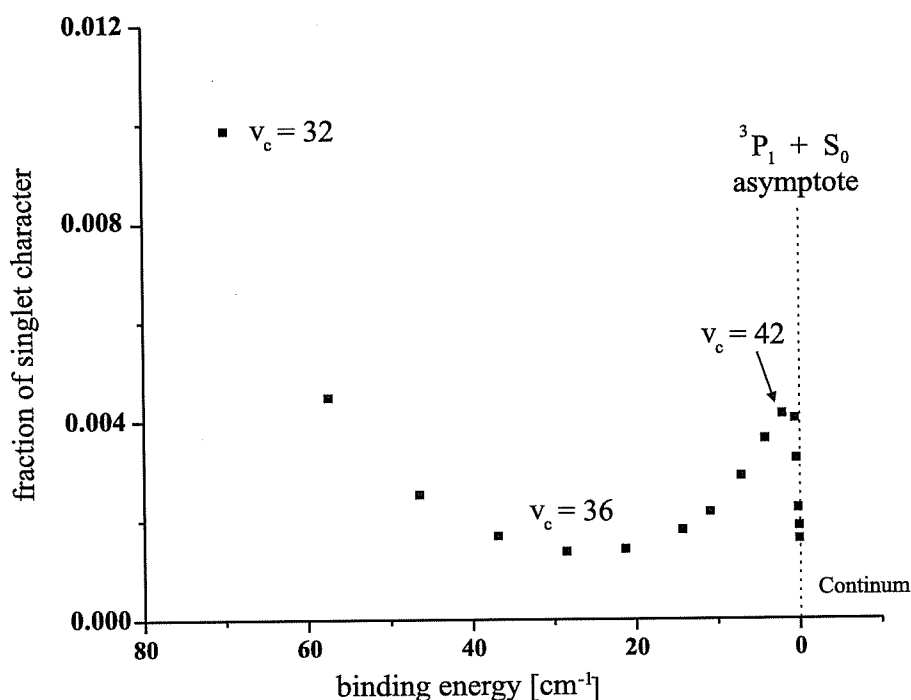


Figure 5.20: Fraction of A state character of the levels of the $c^3\Pi_u$ near the triplet asymptote as function of the binding energy.

[Lisdat Ch. et al., 2001] and [Manaa M.R. et al., 2002]. Lisdat *et al.* showed that the widely used local deperturbation analysis, which takes account of couplings within a limited set of neighboring vibrational levels does not allow a satisfactory representation with a reasonable number of parameters (they obtained $\bar{\sigma} = 4$). There is no obvious criterion, which may help to restrict the number of neighbor levels to consider. They demonstrated that one consequence is that the shifts induced by the coupling between both states on the lower levels of the $^3\Pi_u$ lying below the potential-curve crossing are not well described. The Fourier grid Hamiltonian method allow a global analysis, therefore the cumulative effect of all vibrational levels of the $A^1\Sigma_u^+$ on the $b^3\Pi_u$ on each vibrational level within each subspace of J , is properly included. The number of parameters is then limited to those of the potentials and those of the coupling functions. The global deperturbation permitted to reach $\bar{\sigma} = 1.2$. The present work is then a second example of a global approach. The spin-orbit coupling is 2 times larger for Ca_2 compared to K_2 and the $c^3\Pi_u$ state is 5 times shallower than the $b^3\Pi_u$ state. Therefore, the

cumulative effects are more important for Ca_2 , and a local deperturbation would have clearly failed. A more complete model for the coupled-states compared to Lisdat *et al.* was needed. We have considered the long-range behavior of the $c^3\Pi_u$ potential, and take into account the influence of the $a^3\Sigma_u$ state. This is due to the particularity of the $c^3\Pi_u$ potential to be quite shallow.

The analysis of [Manaa M.R. et al., 2002] use also a global approach. The levels positions are first described with a series of Dunham parameters for both states. Then, from these coefficients RKR potentials are calculated, and used in a coupled-channel treatment for the calculation of the energy levels. These levels are compared to the observed ones, and the initial representation by the Dunham coefficients is improved. The procedure is repeated iteratively to obtain a good representation of the observed data. The derived "deperturbed" Dunham expansions should be used with the RKR potentials, the spin-orbit couplings, and its dependence with the internuclear distance in order to reproduce desired observed levels. Therefore, to use this representation is not straightforward and the physical meaning of the intermediate RKR potentials is not clear. Furthermore, problem of convergence of the Dunham expansion for the levels near the asymptotes limit the use of the method. The Fourier grid Hamiltonian method with analytical potentials, which take properly into account the long-range part of the potential allow a complete treatment of a coupled-states system.

Chapter 6

Conclusion

I have explained in the introduction of this thesis that the available knowledge about the calcium dimer states was limited and sometimes questionable. The potential energy curves of the ground state $X^1\Sigma_g^+$ and the $B^1\Sigma_u^+$ have been obtained by Vidal in 1980. We found that the shape of this ground state potential presents a non-physical behavior for its repulsive part. Unfortunately, the original spectroscopic data have been lost since 1980, preventing the correction of the derived potential curve. Several spectroscopic studies of the $A^1\Sigma_u^+ - c^3\Pi_u$ coupled states have been realized by Bondybey and English and by Hofmann and Harris. Rovibrational constants and local coupling parameters have been derived, but no definite answers about the vibrational assignments have been reached for both states. An accurate determination of the long range part of the $B^1\Sigma_u^+$ state potential have been obtained by photoassociation spectroscopy at the $^1P + ^1S$ asymptote reported in [Zinner G. et al., 2000].

In this thesis work we have re-investigated the ground state of the $^{40}\text{Ca}_2$ molecule using a highly accurate Fourier transform spectroscopy on the laser induced fluorescence of the $B^1\Sigma_u^+ - X^1\Sigma_g^+$ system. We have collected a large and dense body of data, and determined a potential energy curve by two full-quantal approaches involving different representation of the potential. We have used an analytical representation, parameters of which are determined with a non-linear fitting routine, and a point-wise representation, potential-points of which are adjusted with an iterative linear procedure. The two approaches allowed us to investigate the internuclear region where the potential does not depend on the choice of representation [$3 \text{ \AA} - 10 \text{ \AA}$], and thus is uniquely determined. We demonstrated that it is not the interval of classical turning points of the observed levels, which define the range of reliability of a potential. Therefore, a physical long-range model, extrapolating the potential outside this range will not give a reliable long-range part of the

potential. We have enriched our data by observing levels near the asymptotic limit by the filtered laser excitation technique. The highest observed level lies only 0.2 cm^{-1} below the dissociation threshold and have a classical turning point at 20 \AA . The range of reliability is not significantly increased by the newly collected levels. We discovered that the data can be precisely described with a pure dispersion potential starting at relatively short internuclear separation inside the range of reliability at 9.5 \AA allowing in this way a good determination of the potential up to large internuclear distances. The derived potential describes 99.98% of the well depth of the ground state. The dispersion coefficients C_6 , C_8 , C_{10} , and the dissociation energy have been directly adjusted on the observed data. The ground state potential curve have been greatly improved compared to the potential achieved by Vidal, and we showed that the derived dissociation energy differs by 7 cm^{-1} compared to the previous value lying far outside the given error limit by Vidal.

The motivation of our investigation is to derive an interaction potential, which can be used for the description and the prediction of cold-collisions dynamics. Therefore, the accuracy of the long-range potential should be estimated. To transfer the information of the experimental accuracy of the observed data to the uncertainty of the long-range coefficients, we have adapted a Monte-Carlo simulation. We have obtained confidence intervals for the dispersion coefficients and the dissociation energy. The precision on the C_6 coefficient of the leading van der Waals force is in the order of few percent. This uncertainty interval contains the values of the most recent ab-initio calculation of the C_6 value. It was then straightforward to obtain the values and the uncertainty of molecular and atomic properties like the position of the last bound level, and the s-wave scattering length. We have demonstrated that the scattering length is positive showing that a Bose-Einstein condensate with calcium atoms will be stable.

The characterization of the ground state potential have already set the basis for the understanding of the observation of photoassociation spectra achieved recently and published in [Degenhardt C. et al., 2003]. It allowed to perform a full simulation of rotational line profiles and thermal line shifts observed in a the trap loss experiment with an ensemble of calcium atoms at 3 mK .

A molecular calcium supersonic beam is under construction in our group. Using a stimulated Raman adiabatic passage scheme to perform the spectroscopy of the last bound levels of the ground state, where the main contribution to the experimental uncertainty will be caused by the Doppler broadening of the lines due to the slight divergence of the beam. It will allow to improve the accuracy of the long-range coefficients by a factor higher than 10 and to obtain a better description of the exchange energy contribution to the long-range behavior of the interaction potential.

The collected data from the spectroscopic study of the $B^1\Sigma_u^+ - X^1\Sigma_g^+$ system allowed us to determine a $B^1\Sigma_u^+$ state potential using the analytical representation, which describes the observed data with a standard deviation slightly larger than the experimental uncertainty. Our analysis shows that more data are necessary in order to fix the shape of the potential. We have confirmed that no local perturbation larger than the experimental accuracy are present for the levels lower than $v_B = 23$. High precision data can be obtained by spectroscopy in the molecular beam in order to fill the gap between the photoassociation data and the data observed during the present work. Then the complete potential of the B state can be determined. Due to the lack of hyperfine structure the description of cold collision is facilitate. The calcium element as the other alkaline-earth atoms can serve as testing ground for the theoretical models. One can compare the quality of description of the long-range levels from the observed photoassociation spectra, for the accumulated phase method [Moerdijk A.J. et al., 1995] and for the full potential approach always used in the present thesis.

We have investigated the $A^1\Sigma_u^+ - c^3\Pi_u$ coupled states. Energy levels having mainly a singlet character have been observed by laser induced fluorescence combined with Fourier transform spectroscopy. We have included in the data set the observation by Hofmann and Harris from 1986, and we have considered the complete Hamiltonian for the subspace of states $A^1\Sigma_u^+ - c^3\Pi_u - a^3\Sigma_u^+$ in order to describe the observed perturbed levels. The calculation of level positions have been obtained with the Fourier grid Hamiltonian method combined with a fitting routine for the adjustment of the parameters of the potential curves and the spin-orbit coupling functions. We have reached a satisfactory description of the coupled system. The standard deviation is close to the experimental accuracy. Trends in the observed-minus-calculated levels are still present. Since our model is complete in the considered subspace, we believe that improvement of the representation of the data can be reached having a better coupling functions for the spin-orbit interaction from new ab-initio calculations (in progress [Bussery-Honvault B. et al.,]).

In order to get more precise potential curves, especially for the $c^3\Pi_u$ and to reduce the correlation between all the parameters entering the description of the coupled-states, a spectroscopic study of the c state is needed. We have seen from our revised interpretation of the observation of Bondybey and English that the observation of levels with high triplet character can be achieved in a supersonic jet. This gives a promising ground for the beam experiment under development in our group. An improved description of the coupled system including data from envisaged photoassociation at the $^3P_1 + ^1S_0$ asymptote can allow the calculation of decay rate of levels of the coupled-states near the triplet asymptote to the vibrational levels of electronic ground

state. The efficiency of formation of cold molecules in the ground state via photoassociation to the $^3P_1 + ^1S$ asymptote by a selective excitation of levels with a significant singlet character can be estimated.

The energy shift induced by the binary collisions between calcium atoms during the laser interrogation of the intercombination transition in the frequency standard experiment have been recently estimated to be lower than (-20 ± 55) mHz for a density of 10^{15} m^{-3} at the temperature of $20 \text{ } \mu\text{K}$, giving a relative shift lower than $(-0.4 \pm 1.2) \times 10^{-16}$ [C. Degenhardt, 2004]. For a relative instability of 10^{-15} for a time of observation lower than one second the shift is not the main limiting factor of precision. The developments of the calcium optical frequency standard are very promising. In the prospect that the quantum projection noise limited instability of 4×10^{-17} in only 1 s be reached, the collisional shift could become the main limiting contribution to the uncertainty budget. Therefore the estimation of the frequency shift is of importance for the next generation frequency standard.

The calculation of the collisional frequency shift at finite temperature is rather complicate in the case of the alkalis, and in particular for ^{133}Cs , which is the used element for the present atomic clocks, due to the large number of collisional channels [Leo P.J. et al., 2001]. The lack of hyperfine structure and the information already collected about the dynamics of cold collisions between calcium atoms provide arguments to test the theoretical models with this element. The complete potentials of the $X^1\Sigma_g^+$ state and the $c^3\Pi_u - A^1\Sigma_u^+$ coupled states can provide precise descriptions of the collisional processes, and comparison with experiment on the Ca frequency standard can be very valuable for the understanding of the interactions between light and an ensemble of atoms. These considerations give grounds for the continuation of the study I have undertaken during my thesis.

Appendix A

Tables of parameters of the $X^1\Sigma_g^+$, $B^1\Sigma_u^+$, $A^1\Sigma_u^+$, and $c^3\Pi_u$ potentials

The parameters of the analytic potential are listed in table A.1. The $\{a_i\}$ are the coefficients of the expansion equation 2.8 and 2.9, the A and B are used to extrapolate the expansion at $R \leq R_{inn}$ using the expression 2.10 page 35. The parameters (grid of points) of the point-wise representation of the potential are listed in table A.2. A natural spline should be used to interpolate the given points. For both representations the analytic long-range model equation 2.11 is used beyond R_{out} . No errors are attached to the parameters corresponding to the intermediate region of the potential since they have no individual physical meaning. Only the eigenvalues calculated from the complete potential will obtain a predictive uncertainty read off from the standard deviations of the fit. For the potential of the B state the extrapolation 4.1 is to be used. For the potentials of the A state and the c state the extrapolations 5.32 and 5.33 should be used.

Table A.1: Parameters of the analytic representation of the $X^1\Sigma_g^+$ state potential energy curve in $^{40}\text{Ca}_2$. The minimum energy of the potential is at zero.

$R \leq 3.66 \text{ \AA}$	
R_{inn}	3.66 \AA
A	$-2.9714 \times 10^2 \text{ cm}^{-1}$
B	$7.209 \times 10^9 \text{ cm}^{-1} \text{\AA}^{12}$
$3.66 \text{ \AA} < R < 9.5 \text{ \AA}$	
b	-0.5929
R_{m}	4.277277 \AA
a_0	0.00043 cm^{-1}
a_1	$-2.57153863528197002 \text{ cm}^{-1}$
a_2	$3.79611687289805877 \times 10^3 \text{ cm}^{-1}$
a_3	$3.82947943867555637 \times 10^2 \text{ cm}^{-1}$
a_4	$-2.74470356912936631 \times 10^3 \text{ cm}^{-1}$
a_5	$-3.23378807398046092 \times 10^3 \text{ cm}^{-1}$
a_6	$3.70205119299758223 \times 10^2 \text{ cm}^{-1}$
a_7	$6.35318559107446436 \times 10^3 \text{ cm}^{-1}$
a_8	$-7.39783474312859562 \times 10^3 \text{ cm}^{-1}$
a_9	$-1.90759867971015337 \times 10^4 \text{ cm}^{-1}$
a_{10}	$5.41779135173975228 \times 10^4 \text{ cm}^{-1}$
a_{11}	$4.40527349765557083 \times 10^4 \text{ cm}^{-1}$
a_{12}	$-1.55406021572582802 \times 10^5 \text{ cm}^{-1}$
a_{13}	$-8.35826911941128783 \times 10^4 \text{ cm}^{-1}$
a_{14}	$2.13873243831604603 \times 10^5 \text{ cm}^{-1}$
a_{15}	$1.56022970979522303 \times 10^5 \text{ cm}^{-1}$
a_{16}	$-1.56329579530082468 \times 10^5 \text{ cm}^{-1}$
a_{17}	$-1.46822446075956163 \times 10^5 \text{ cm}^{-1}$
a_{18}	$2.74480910039127666 \times 10^4 \text{ cm}^{-1}$
a_{19}	$7.11882274192053592 \times 10^4 \text{ cm}^{-1}$
a_{20}	$-7.63044568335207146 \times 10^2 \text{ cm}^{-1}$
$R \geq 9.5 \text{ \AA}$	
R_{out}	9.5 \AA
D_e	1102.074 cm^{-1}
C_6	$1.0030 \times 10^7 \text{ cm}^{-1} \text{\AA}^6$
C_8	$3.87 \times 10^8 \text{ cm}^{-1} \text{\AA}^8$
C_{10}	$4.41 \times 10^9 \text{ cm}^{-1} \text{\AA}^{10}$
Additional parameter	
$D_0 = 1069.870(9) \text{ cm}^{-1}$	

Table A.2: Parameters of the numeric representation of the $X^1\Sigma_g^+$ state potential energy curve in $^{40}\text{Ca}_2$.

R [Å]	V [cm^{-1}]	R [Å]	V [cm^{-1}]
3.096980	9246.6895	5.678571	636.3741
3.188725	6566.7325	5.809524	684.9589
3.280470	4525.7282	5.940476	728.9235
3.372215	3090.9557	6.071429	768.5976
3.463960	2134.2175	6.202381	804.2551
3.555705	1475.2425	6.333333	836.2419
3.647450	1004.5043	6.464286	864.8746
3.739195	661.4123	6.595238	890.4666
3.830940	410.6117	6.726191	913.2923
3.922685	234.0001	6.857143	933.6417
4.014430	116.0996	6.988095	951.7718
4.106174	44.5437	7.119048	967.8632
4.197920	8.6885	7.250000	982.2159
4.289664	0.1760	7.500000	1005.2497
4.381409	11.9571	7.750000	1023.6698
4.500000	48.5948	8.000000	1038.3262
4.630952	106.9081	8.358974	1054.3861
4.761905	175.7311	8.717949	1066.0579
4.892857	248.8199	9.076923	1074.5969
5.023809	322.3873	9.435897	1080.8961
5.154762	393.7222	9.794872	1085.5974
5.285714	461.4555	10.303419	1090.2990
5.416667	524.6311	10.811966	1093.5160
5.547619	582.9870	11.611111	1096.6870
<hr/>			
$D_e = 1102.060 \text{ cm}^{-1}$			
$R_{\text{out}} = 9.44 \text{ Å}$		$C_8 = 3.808 \times 10^8 \text{ cm}^{-1} \text{ Å}^8$	
$C_6 = 1.0023 \times 10^7 \text{ cm}^{-1} \text{ Å}^6$		$C_{10} = 5.06 \cdot 10^9 \text{ cm}^{-1} \text{ Å}^{10}$	
<hr/>			
informal parameter			
$D_0 = 1069.868 \text{ cm}^{-1}$			
<hr/>			

Table A.3: Parameters of the analytic representation of the $B^1\Sigma_u^+$ state potential energy curve in $^{40}\text{Ca}_2$. The reference point is the minimum of the ground state potential chosen to be at zero energy.

$R \leq R_{\text{inn}} = 3.22 \text{ \AA}$	
A^*	$0.185778005 \times 10^5 \text{ cm}^{-1}$
B^*	$0.416879830 \times 10^{10} \text{ cm}^{-1} \text{ \AA}^{12}$
$3.22 \text{ \AA} < R < R_{\text{out}} = 5.10 \text{ \AA}$	
b	0.20
R_{m}	3.80850 \text{ \AA}
a_0	$18964.02790000 \text{ cm}^{-1}$
a_1	$0.134084003805927061 \times 10^2 \text{ cm}^{-1}$
a_2	$0.115261464616408630 \times 10^6 \text{ cm}^{-1}$
a_3	$-0.175521794513471046 \times 10^6 \text{ cm}^{-1}$
a_4	$-0.389222772580998542 \times 10^6 \text{ cm}^{-1}$
a_5	$-0.177855712188965688 \times 10^7 \text{ cm}^{-1}$
a_6	$0.873202562191374972 \times 10^7 \text{ cm}^{-1}$
a_7	$0.895182228732362986 \times 10^8 \text{ cm}^{-1}$
a_8	$-0.617220569199902654 \times 10^9 \text{ cm}^{-1}$
a_9	$-0.9132733099611920129 \times 10^9 \text{ cm}^{-1}$
a_{10}	$0.158286938284422684 \times 10^{11} \text{ cm}^{-1}$
a_{11}	$-0.333319651215654411 \times 10^{11} \text{ cm}^{-1}$
a_{12}	$0.242006639487103224 \times 10^{10} \text{ cm}^{-1}$
$R_{\text{out}} \leq R$	
$D_e^{\text{B}*}$	$5790.4(5) \text{ cm}^{-1}$
C_3^*	$0.37544747 \times 10^6 \text{ cm}^{-1} \text{ \AA}^3$
C_6^*	$0.91057144 \times 10^6 \text{ cm}^{-1} \text{ \AA}^6$
Additional constants:	
equilibrium distance:	$R_e^{\text{B}} = 3.808(1) \text{ \AA}$
electronic term difference:	$T_e^{\text{B}} = 18963.972272 \text{ cm}^{-1}$

* for boundary conditions (see text)

Table A.4: Parameters of the analytic representation of the $A^1\Sigma_u^+$ state potential energy curve in $^{40}\text{Ca}_2$. The energy reference is the minimum of the ground state potential chosen to be at zero energy.

$R \leq R_{\text{inn}} = 3.08 \text{ \AA}$	
A^*	$0.131405404 \times 10^5 \text{ cm}^{-1}$
B^*	$0.23709888 \times 10^9 \text{ cm}^{-1} \text{ \AA}^{10}$
$3.08 \text{ \AA} < R < R_{\text{out}} = 4.511 \text{ \AA}$	
b	-0.57
R_m	3.59402020 \AA
a_0	$14106.96734957 \text{ cm}^{-1}$
a_1	$-0.2257756991559098 \times 10^2 \text{ cm}^{-1}$
a_2	$0.1220361055570128 \times 10^5 \text{ cm}^{-1}$
a_3	$0.6769308221686881 \times 10^4 \text{ cm}^{-1}$
a_4	$-0.4634816798413386 \times 10^4 \text{ cm}^{-1}$
a_5	$0.1690127577627890 \times 10^5 \text{ cm}^{-1}$
a_6	$0.9381164005690928 \times 10^5 \text{ cm}^{-1}$
a_7	$-0.4559579065456276 \times 10^5 \text{ cm}^{-1}$
a_8	$-0.6353781758173143 \times 10^6 \text{ cm}^{-1}$
a_9	$-0.6751424160995947 \times 10^6 \text{ cm}^{-1}$
a_{10}	$0.1209687968209198 \times 10^7 \text{ cm}^{-1}$
a_{11}	$0.3799595228169478 \times 10^7 \text{ cm}^{-1}$
a_{12}	$0.3064094811331930 \times 10^7 \text{ cm}^{-1}$
$R_{\text{out}} \leq R$	
D_e^A	$8844.751(9) \text{ cm}^{-1}$
C_5^*	$0.1184628 \times 10^9 \text{ cm}^{-1} \text{ \AA}^5$
C_6^*	$-0.6358778 \times 10^9 \text{ cm}^{-1} \text{ \AA}^6$
C_8^*	$0.3218361 \times 10^8 \text{ cm}^{-1} \text{ \AA}^8$
Additional constants:	
equilibrium distance:	$R_e^A = 3.594(1) \text{ \AA}$
electronic term difference:	$T_e^A = 14106.957(9) \text{ cm}^{-1}$

* for boundary conditions (see text)

Table A.5: Parameters of the analytic representation of the $c^3\Pi_u$ state potential energy curve in $^{40}\text{Ca}_2$. The energy reference is the minimum of the ground state potential chosen to be at zero energy.

$R \leq R_{\text{inn}} = 3.369 \text{ \AA}$	
A^*	$0.131405404 \times 10^5 \text{ cm}^{-1}$
B^*	$0.23709888 \times 10^9 \text{ cm}^{-1} \text{ \AA}^{10}$
$3.369 \text{ \AA} < R < R_{\text{out}} = 7.350 \text{ \AA}$	
b	-0.20
R_m	4.06654583 \AA
a_0	$14841.95353351 \text{ cm}^{-1}$
a_1	$-0.3036332121763454 \times 10^1 \text{ cm}^{-1}$
a_2	$0.1767842659743363 \times 10^5 \text{ cm}^{-1}$
a_3	$-0.1852820967921904 \times 10^5 \text{ cm}^{-1}$
a_4	$0.3934518027564040 \times 10^5 \text{ cm}^{-1}$
a_5	$-0.4426362334350374 \times 10^6 \text{ cm}^{-1}$
a_6	$-0.3168777573729329 \times 10^7 \text{ cm}^{-1}$
a_7	$0.2451491313546689 \times 10^8 \text{ cm}^{-1}$
a_8	$0.2452052452711268 \times 10^8 \text{ cm}^{-1}$
a_9	$-0.4412763936304449 \times 10^9 \text{ cm}^{-1}$
a_{10}	$0.4469452325764918 \times 10^9 \text{ cm}^{-1}$
a_{11}	$0.3155234326261032 \times 10^{10} \text{ cm}^{-1}$
a_{12}	$-0.7818086347467031 \times 10^{10} \text{ cm}^{-1}$
a_{13}	$-0.3064990751325005 \times 10^{10} \text{ cm}^{-1}$
a_{14}	$0.3115018184529581 \times 10^{11} \text{ cm}^{-1}$
a_{15}	$-0.3988067473686848 \times 10^{11} \text{ cm}^{-1}$
a_{16}	$0.1679365847361850 \times 10^{11} \text{ cm}^{-1}$
$R_{\text{out}} \leq R$	
D_e^{c*}	$1470.184(9) \text{ cm}^{-1}$
C_6^{c*}	$0.1855883 \times 10^8 \text{ cm}^{-1} \text{ \AA}^6$
C_8^{c*}	$0.5410024 \times 10^6 \text{ cm}^{-1} \text{ \AA}^8$
Additional constants:	
equilibrium distance:	$R_e^c = 4.067(1) \text{ \AA}$
electronic term difference:	$T_e^A = 14106.957(9) \text{ cm}^{-1}$

* for boundary conditions (see text)

Parameters of the diagonal spin-orbit coupling $A(R)$:

$$\begin{aligned}A_0 &= 0.4802 \times 10^2 \text{ cm}^{-1} \\A_6 &= -0.1504 \times 10^4 \text{ cm}^{-1} \text{ \AA}^6 \\A_{12} &= -0.9718 \times 10^5 \text{ cm}^{-1} \text{ \AA}^{12}\end{aligned}$$

Non-diagonal spin-orbit coupling between the $A^1\Sigma_u^+$ (0) and the $c^3\Pi_u$ (0):

$$\chi = 0.36507 \times 10^2 \text{ cm}^{-1}$$

Appendix B

Distributions of the C_6, C_8, C_{10} coefficients

The projections of the total distribution of parameters on the C_6 and C_8 plan, on the C_6 and C_{10} and on the C_8 and C_{10} plane are presented on this page and the next one.

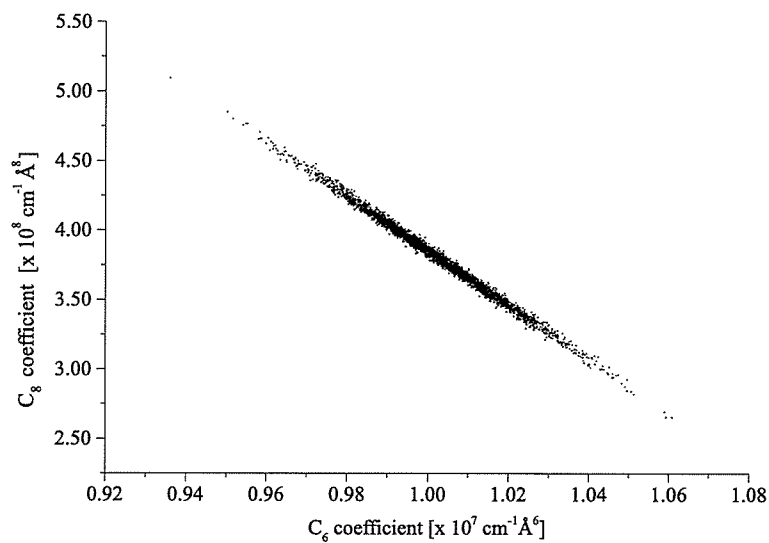
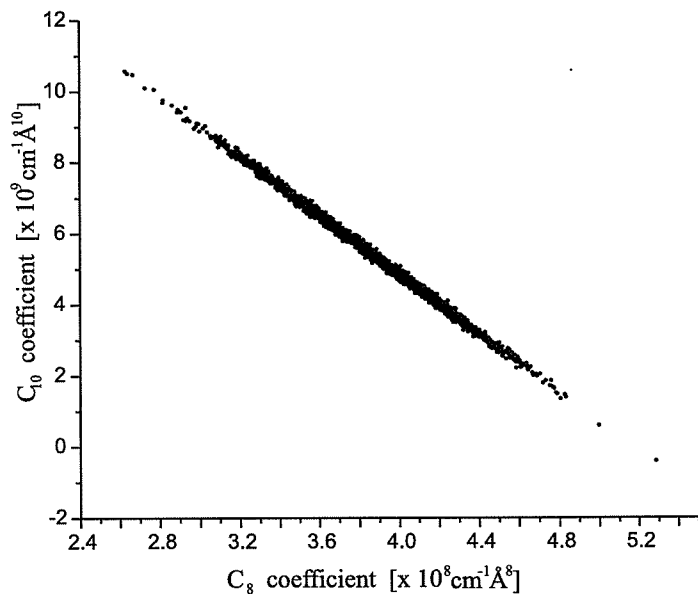
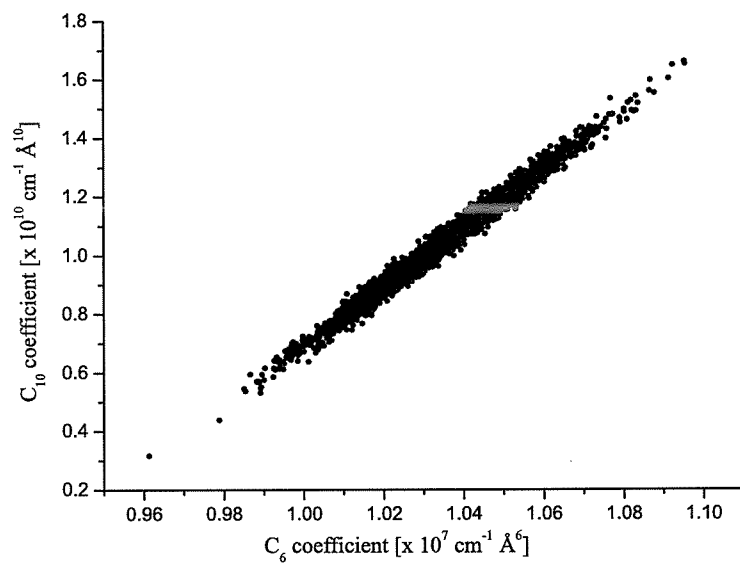


Figure B.1: Projection on the long-range (C_6, C_8) plane.

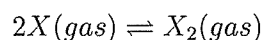
Figure B.2: Projection on the long-range (C_8, C_{10}) plane.Figure B.3: Projection on the long-range (C_6, C_{10}) plane.

Appendix C

Concentration of Ca and Ca₂ in the oven.

Let's consider an oven filled at room temperature with a certain amount of "pure" element X . The oven is then heated up to a temperature T . Inside this oven there is a certain amount of the element in the vapor phase characterized by its saturated vapor pressure p^{sat} which is only determined by T . The oven is in the canonical situation since we can consider that it is in contact with a thermostat at the temperature T (heating system).

At this temperature there is a non zero probability that the elements associate together to form dimers. These dimers have also a certain probability to dissociate depending on their dissociation energy. There is then equilibrium characterized by this equation:



Supposing that both X and X_2 elements behave like ideal gases let's calculate their respective amount in the gas phase inside the oven. We know from text book of statistical thermodynamics that the equilibrium constant of a chemical reaction equal:

$$K_p = \prod_J \left(\frac{p_J}{p^\circ} \right)^{\nu_J}$$

where J takes for X or X_2 and $p^\circ = 10^5$ Pa. And ν_J are the fraction of X and X_2 formed in the reaction: $0 = \nu(X)X(gas) + \nu(X_2)X_2(gas)$ Since the forward reaction is $0 = 2X(gas) - X_2(gas)$ then $\nu(X) = 2$ and $\nu(X_2) = -1$. Then

$$K_p = \frac{p(X)^2}{p(X_2)p^\circ}$$

We can write again the equilibrium constant in terms of the concentrations using $[X] = p(J)/RT$ and the molar volume $V_m^e = RT/p^e$:

$$K_p = \frac{[X]^2 V_m^e}{[X_2]}$$

Using the Gibbs function G for independent particles we can write K_p as:

$$K_p = \prod_J \left(\frac{q_J^e}{N_A} \right)^{\nu_J} \times e^{-\Delta E_0/RT}$$

q_J^e is the partition function respective to the J element and ΔE_0 is the molar dissociation energy of the molecule at $T = 0$.

The atomic molar partition function is related, only to their translational motion and the electronic degeneracy, as:

$$q^e(X) = \frac{g(X) V_m^e}{\Lambda(X)^3} \quad \Lambda(X) = \left(\frac{\hbar^2 k_B T}{2\pi m_{Ca}} \right)^{1/2}$$

The energy of the molecule can be written in the Born-Oppenheimer approximation as a sum of the contribution of the different degrees of freedom:

$$\epsilon_j^{tot} = \epsilon_j^{Trans} + \epsilon_j^{Elec} + \epsilon_j^{Vib, Rot}$$

The vibrational and rotational are not decoupled. We can thus approximate the molecular molar partition function as the product of the molar partition function of each precedent modes of motion:

$$q^e(X_2) = q^{Trans} \times q^{Elec} \times q^{Vib, Rot}$$

The diatomic molar partition function is then:

$$q^e(X) = \frac{g(X_2) V_m^e q^{Vib, Rot}}{\Lambda(X_2)^3} \quad \Lambda(X_2) = \left(\frac{\hbar^2 k_B T}{2\pi m_{Ca_2}} \right)^{1/2}$$

Then it follows that the equilibrium constant is

$$K_p = \frac{g(X)^2}{g(X_2)} \times \frac{\Lambda(X_2)^3 V_m^e}{\Lambda(X)^6 N_A} \times \frac{1}{q^{Vib, Rot}(X_2)} \times e^{-\Delta E_0/RT}$$

In the Handbooks of Chemistry or Physics we find the dependence of the vapor pressure for atoms with respect to the temperature.

Then

$$[X] = \frac{p^{sat}(X)}{RT} \quad [X_2] = \frac{[X]^2 V_m^e}{K_p}$$

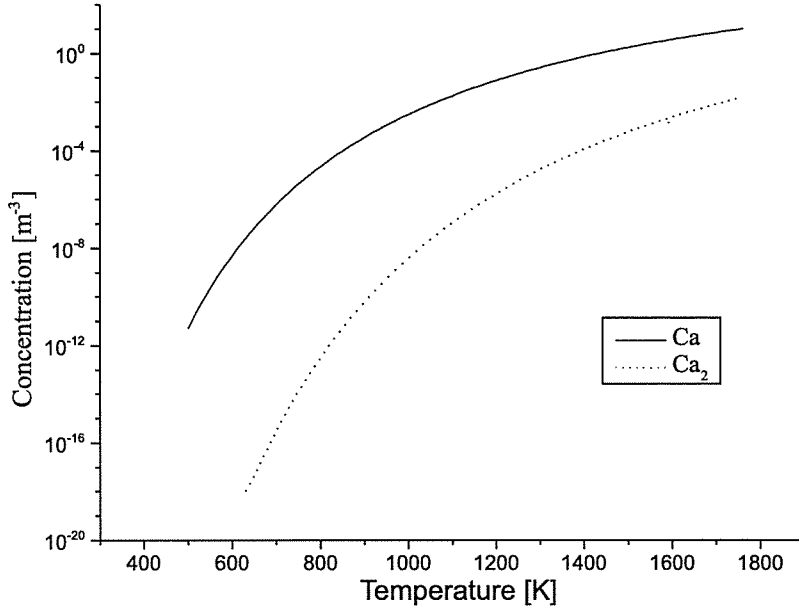


Figure C.1: molar concentration of Ca and Ca₂ in function of the temperature of the oven.

We can now calculate for the case of calcium the amount of atoms and dimers in the oven in function of the temperature. The partition function $q^{Vib, Rot}$ has been computed having the knowledge of the ground state potential curve which allowed the determination of the energies $E_{v,J}$ and the relation:

$$q^{Vib, Rot} = \sum_{v,J} (2J + 1) e^{-E_{v,J}/k_B T}$$

The ground state of Ca is a 1S_0 state with no hyperfine degeneracy so we have $g(X_2) = 1$. The single ground state of Ca₂ has the $^1\Sigma_g^+$ symmetry so $g(X_2)=1$. The molar dissociation energy is the energy necessary to dissociate one mole of dimers in their ground rovibrational level ($v = 0, J = 0$). $E_0 = 1069.87 \text{ cm}^{-1}$ so $\Delta E_0 = 12795.60 \text{ J mol}^{-1}$.

We can now plot the dependence of the concentration in function of the Temperature:

The typical temperature used during the experiments is 1220 K. Therefore, the calculated concentration of Ca₂ at this temperature is 2×10^{-12} mole cm^{-3} i.e. $\sim 1.2 \times 10^{12}$ calcium dimers per cm^{-3} . The dynamics in a heat pipe oven is different than in a conventional oven therefore these concentrations are only indication of the amount of calcium in our pipe. This number give probably a better estimation of the concentrations in the oven used in a beam

experiment in the case where the aperture for the expansion of the vapor of calcium is not too large.

Bibliography

- [Amiot C. et al., 1999] Amiot C., Dulieu O., and Vergs (1999). Resolution of the apparent disorder of the Rb_2 $A^1\Sigma_u^+(0_u^+)$ and $b^3\Pi_u(0_u^+)$ spectra: A case of fully coupled electronic state). *Phys. Rev. Lett.*, 83(12):2316.
- [Balfour W.J. and Whitlock R.F., 1975] Balfour W.J. and Whitlock R.F. (1975). The visible absorption spectrum of Ca_2 . *Can. J. Phys.*, 53:472.
- [Bartenstein M. et al., 2004] Bartenstein M., Altemeyer A., Riedl S., Jochim S., Chin C., Hecker Denschlag J., and Grimm R. (2004). Crossover from a molecular bose-einstein condensate to a degenerate fermi gas. *Phys. Rev. Lett.*, 92:120401.
- [Bell R. J., 1974] Bell R. J. (1974). *Introductory Fourier transform spectroscopy*. academic press New York and London.
- [Binnewies T. et al., 2001] Binnewies T., Whilpers G., Sterr U., Riehle F., Helmcke J., Mehlstäubler, Rasel E.M., and Ertmer W. (2001). *Phys. Rev. Lett.*, 87:123002.
- [Bondybey V. E. and English J.H., 1984] Bondybey V. E. and English J.H. (1984). Laser-induced fluorescence of the calcium dimer in supersonic jet: The red spectrum of Ca_2 . *Chem. Phys. Lett*, 111(3):195.
- [Brown J.M. et al., 1975] Brown J.M., Hougen J.T., Huber K.-P, Johns J.W.C., Kopp I., Lefebvre-Brion H., Merker A.J., Merer A.J., Ramsay D.A. and Rostas J., and Zare R.N. (1975). The labeling of parity doublet levels in linear molecules. *J. Mol. spectrosc.*, 55:500.
- [Bussery-Honvault B. et al.,] Bussery-Honvault B., Launay J.-M., and Moszynski R. Private communication.
- [Bussery-Honvault B. et al., 2003] Bussery-Honvault B., Launay J.-M., and Moszynski R. (2003). Cold collision of ground state calcium atoms in a laser field: A theoretical study. *Phys. Rev. A*, 68(032718).

- [C. Degenhardt, 2004] C. Degenhardt (2004). *Freie und gespeicherte Calcium-Atome für ein optisches Frequenznormal*. PhD thesis, Universität Hannover.
- [Cornish S. L. et al., 2000] Cornish S. L., Claussen N.R., Roberts J. L., Cornell E. A., and Wieman C.E. (2000). Stable ^{85}Rb Bose-Einstein Condensates with Widely Tunable Interactions. *Phys. Rev. Lett.*, 85:1795.
- [Czuchaj E. et al., 2003] Czuchaj E., Krosnicki, and Stoll H. (2003). Valence ab-initio calculation of the potential-energy curves of the Ca_2 dimer. *Theoretical chemistry accounts*, 110:28.
- [Dalibard J. and Cohen-Tannoudji., 1985] Dalibard J. and Cohen-Tannoudji. (1985). Dressed-atom approach to atomic motion in laser light: the dipole force revisited. *J. Opt. Soc. Am. B*, 2:1707.
- [Degenhardt C. et al., 2003] Degenhardt C., Binnewies T., Wilpers G., Sterr U., Riehle F., Lisdat C., and Tiemann E. (2003). Photoassociation spectroscopy of cold calcium atoms. *Phys. Rev. A.*, 67(043408).
- [Demtröder W.,] Demtröder W. *Laser Spectroscopy. Basic concepts and instrumentation*, volume 29 of *Springer series in chemical physics*. Springer-Verlag, corrected third printing 1988 edition.
- [Dulieu O. and Julienne P.S., 1995] Dulieu O. and Julienne P.S. (1995). Coupled channel bound states calculations for alkali dimers using the Fourier grid method. *J. Chem. Phys.*, 103:60.
- [Dunham J. L., 1932] Dunham J. L. (1932). The energy of a rotating vibrator. *Phys. Rev.*, 41:721.
- [Dyall K.G. and Mclean A.D., 1992] Dyall K.G. and Mclean A.D. (1992). The potential energy curves of the $X^1\Sigma_g^+$ ground state of Mg_2 and Ca_2 using the interaction correlated fragments model. *Phys. Rev. B*, 97(11):8424.
- [Falke St.,] Falke St. private communication.
- [Hansen D.P. et al., 2003] Hansen D.P., Mohr J.R., and Hemmerich A. (2003). Magnetic trapping of metastable calcium atoms. *Phys. Rev. A*, 67:021401.
- [Herzberg G.,] Herzberg G. *Molecular spectra and molecular structure. I. Spectra of diatomic molecules*. Van nostrand reinhold company, second edition.

- [Hofmann R. T. and Harris D. O., 1984] Hofmann R. T. and Harris D. O. (1984). *J. Chem. Phys.*, 81(2):1047.
- [Hofmann R. T. and Harris D. O., 1986] Hofmann R. T. and Harris D. O. (1986). Laser spectroscopy, rotational assignment, and perturbation analysis of the $A^1\Sigma_u^+ - X^1\Sigma_g^+$ Ca_2 red system. *J. Chem. Phys.*, 85(7):3749.
- [Huang Y., 2001] Huang Y. (2001). *Determining analytical potential energy functions of diatomic molecules by direct fitting*. University of Waterloo, Ontario, Canada.
- [IodineSpec,] IodineSpec. IodineSpec can be found on the web site www.toptica.com.
- [Jones K.M. et al., 1996] Jones K.M., Maleki S., Bize S., Lett P.D., Williams C.J., Richling H., Knockel H., Tiemann E., Wang H., Gould P.L., and Stwalley W.C. (1996). Direct measurement of the ground-state dissociation energy of Na_2 . *Phys. Rev. A*, 54.
- [Jones R., 1979] Jones R. (1979). Molecular bounding in group II-a dimers $\text{Be}_2 - \text{Ba}_2$. *J.chem. Phys.*, 71:1300.
- [Katori H.,] Katori H. Private communication of preliminary results on photoassociation spectra at the $^3P_1 - ^1S_0$ asymptote of Sr_2 .
- [Katori H. et al., 1999] Katori H., Ido T., Isoya Y., and Kuwata-Gonokami M. (1999). *Phys. Rev. Lett.*, 82(6):1116.
- [Kleinekathofer A., 1995] Kleinekathofer A. (1995). *J. Chem. Phys.*, 103:6617.
- [Kleinekathofer U. et al., 1995] Kleinekathofer U., Tang K.T., Toennis J.P., and Yiu C.L. (1995). Angular coupling in the exchange energy of multi-electron systems. *J. Chem. Phys.*, 103(15):6617.
- [Kokoouline V. et al., 1999] Kokoouline V., Dulieu O., Kosloff R., and Masnou-Seeuws F. (1999). Mapped Fourier methods for long-range molecules: Application to perturbations in $\text{Rb}_2(0_u^+)$ photoassociation spectrum. *J. Chem. Phys.*, 110(20):9865.
- [Kosloff R., 1988] Kosloff R. (1988). *J. Phys. Chem.*, 92.
- [Kuwamoto T. et al., 1999] Kuwamoto T., Honda K., Takahashi Y., and Yabuzaki T. (1999). Magneto-optical trapping of Yb atoms using an intercombination transition. *Phys. Rev. A*, 60:745.

- [Lefebvre-Brion H. and Field R.W., 1986] Lefebvre-Brion H. and Field R.W. (1986). *Perturbation in the spectra of diatomic molecules*. Harcourt Brace Jovanovich.
- [Leo P.J. et al., 2001] Leo P.J., Julienne P.S., Mies F.H., and Williams C.J. (2001). Collisional frequency shifts in ^{133}Cs fountain clocks. *Phys. Rev. Lett.*, 86(17):3743.
- [Linton C., 1978] Linton C. (1978). Photoluminescence of the $A^2\Pi - X^2\Sigma^+$ System of the Yttrium Oxide molecule. *J. Mol. Spectrosc.*, 69:351.
- [Lisdat Ch. et al., 2001] Lisdat Ch., Dulieu O., Knöckel H., and Tiemann E. (2001). Inversion analysis of K_2 coupled electronic states with the Fourier grid method. *Eur. Phys. J. D*, 17:319.
- [Maeder F. and Kutzelnigg, 1979] Maeder F. and Kutzelnigg (1979). *Chem. Phys. Lett.*, 42:95.
- [Manaa M.R. et al., 2002] Manaa M.R., Ross A.J., Martin F., Crozet P., Lyyra A.M., Li Li, Amiot C., and Bergman T. (2002). Spin-orbit interactions, new spectral data, and deperturbation of the coupled $b^3\Pi_u$ and $A^1\Sigma_u^+$ states of K_2 . *J. Chem. Phys.*, 117(24):11208.
- [Mérawa M. et al., 2001] Mérawa M., Tendero C., and Rérat M. (2001). Excited states dipole polarizabilities of calcium atom and long-range dispersion coefficients for the low-lying electronic states of Ca_2 and CaMg . *Chem. Phys. Lett.*, 343:397.
- [MINUIT web page,] MINUIT web page. Function minimization and error analysis from F.James: wwwasdoc.web.cern.ch/minuit/minmain.html. *CERN program library long Wrtiteup D506*.
- [Mitroy J. and Bromley, 2003] Mitroy J. and Bromley (2003). Semiempirical calculation of van der Waals coefficients for alkali-metal and alkaline-earth-metal atoms. *Phys. Rev. A*, 68:052714.
- [Moerdijk A.J. et al., 1995] Moerdijk A.J., Verhaar B.J., and Axelsson A. (1995). *Phys. Rev. A*, 51(6):4852.
- [Monnerville M. and Robbe J.M., 1994] Monnerville M. and Robbe J.M. (1994). *J. Chem. Phys.*, 101:7580.
- [Moszynski R. et al., 2003] Moszynski R., Lach G., Jaszuński M., and Bussery-Honvault B. (2003). Long-range interactions in the Cowan-Griffin

- approximation and their QED retardation: Application to helium, calcium, and cadmium dimers. *Phys. Rev. A*, 68:052706.
- [NIST-databases, 2004] NIST-databases (2004). National institut of standard and technology: www.physics.nist.gov/physrefdata/pes/refdata/ca.html.
- [NIST1,] NIST1. National institut of standard and technology: www.physics.nist.gov/physrefdata/compositions/index.html.
- [NIST2,] NIST2. National institut of standard and technology: www.physics.nist.gov/cuu/constants/index.html.
- [Ortiz G. and Ballone P., 1991] Ortiz G. and Ballone P. (1991). Pseudopotentials for non-local-density functionals. *Phys. Rev. B*, 43(8):6376.
- [Pacchioni G. and Koutecky, 1982] Pacchioni G. and Koutecky (1982). The bond nature of alkine-earth homonuclear metal clusters investigated with pseudopotential CI method. *Chem. Phys.*, 71:181.
- [Pashov A., 2000] Pashov A. (2000). *Doctoral dissertation: Laser spectroscopy of selected excited electronic states of alkali metal diatomic molecules*. PhD thesis, Warsaw University, Poland.
- [Pashov A. et al., 2000a] Pashov A., Jastrzebski W., and Kowalczyk P. (2000a). An improved description of the double minimum $6^1\Sigma^+$ state of NaK by an IPA potential energy curve. *J. Phys. B: Atomic, molecular and optical Physics*, 33(17):611.
- [Pashov A. et al., 2000b] Pashov A., Jastrzebski W., and Kowalczyk P. (2000b). Construction of potential curves for diatomic molecular states by the IPA method. *Comput. Phys. Commun.*, 128:622.
- [Phillips W.D et al., 1985] Phillips W.D, Prodan J.V., and Metcalf H.J. (1985). Laser cooling and electromagnetic trapping of neutral atoms. *J. Opt. Soc. Am. B*, page 1751.
- [Porsev S. G. and Derevianko A., 2002] Porsev S. G. and Derevianko A. (2002). High-accuracy relativistic many-body calculations of van der Waals coefficients, C_6 , for alkaline-earth atoms. *Phys. Rev. A*, 65(020701).
- [Press W.H. et al., 1985] Press W.H., Flannery B.P., Teukolsky S.A., and Vetterling W.T. (1985). *Numerical Recipes: The Art of Scientific Computing*. Cambridge.

- [Radzig A.A. and Smirnov P.M., 1985] Radzig A.A. and Smirnov P.M. (1985). *Reference data on atoms, molecules and ions*. Springer, Berlin.
- [Regal C.A. et al., 2004] Regal C.A., Greiner M., and J D.S. (2004). Observation of resonance condensation of fermionic atom pairs. *Phys. Rev. Lett.*, 92:040403.
- [Richter H. et al., 1991] Richter H., Knöckel H., and Tiemann E. (1991). *Chemical Physics*, 157(1):217.
- [S. Bashkin and J.O. Stoner, 1978] S. Bashkin and J.O. Stoner (1978). *Atomic Energy-Levels and Grotrian Diagrams*, volume 2. North-Holland, Amsterdam.
- [Samuelis C., 2002] Samuelis C. (2002). *Spektroskopie und optische Manipulation kalter Stösse in einem Natrium-molekülstrahl*. PhD thesis, Hannover University, Germany.
- [Samuelis C. et al., 2000] Samuelis C., Tiesinga E., Laue T., Elbs M., Knöckel H., and Tiemann E. (2000). Cold atomic collisions studied by molecular spectroscopy. *Phys. Rev. A*, 63:012710.
- [Seto J.Y. et al., 2000] Seto J.Y., Le Roy R.J., Vergès, and Amiot C. (2000). Direct potential fit analysis of the $X^1\Sigma_g^+$ state of Rb_2 : Nothing else will do! *J. Chem. Phys.*, 113(8):3067.
- [Standard J.M. and Certain P.R., 1985] Standard J.M. and Certain P.R. (1985). *J. Chem. Phys.*, 83:3002.
- [Stanton J.F., 1985] Stanton J.F. (1985). *Phys. Rev. A*, 49:1698.
- [Takasu Y. et al., 2003] Takasu Y., Maki M., Komori K., Takano T., Honda K., Kumakura M., Yabuzaki T., and Takahashi Y. (2003). Spin-Singlet Bose-Einstein Condensation of Two-Electron Atoms. *Phys. Rev. Lett.*, 91:040404.
- [Vidal C. R., 1980] Vidal C. R. (1980). *J. Chem. Phys.*, 72:1864.
- [Vidal C. R., 1996] Vidal C. R. (1996). *Experimental methods in the physical science*, volume 29. Academic press, Inc.
- [Vidal C. R. and Cooper J., 1969] Vidal C. R. and Cooper J. (1969). Heat pipe Oven: A new, well-define metal vapor device for spectroscopic measurements. *J. Appl. Phys.*, 40(8):3370.

- [Vidal C. R. and Scheingraber H., 1977] Vidal C. R. and Scheingraber H. (1977). Determination of diatomic molecular constants using an inverted perturbation approach. *J. Mol. Spectrosc.*, 65:93.
- [Williams C.J. et al., 1999] Williams C.J., Tiesinga E., Julienne P.S., Wang H., Stwalley W.C., and Gould P.L. (1999). Determination of the scattering lengths of ^{39}K from 1_u photoassociation line shapes. *Phys. Rev. A*, 60(6):4427.
- [Wilpers G. et al., 2002] Wilpers G., Binnewies G., Dengenhardt C., Sterr U., Helmcke J., and Riehle F. (2002). Optical clock with ultracold neutral atoms. *Phys. Rev. Lett.*, 89:230801.
- [Zinner G. et al., 2000] Zinner G., Binnewies T., Riehle F., and Tiemann E. (2000). *Phys. Rev. Lett.*, 85(11):2292.

Corrections from 26.11.2004

Page 22 in section 2.2.2 replace "In addition, for bosonic atoms in diatomic molecules,..." by "In addition, for bosonic atoms with nuclear spin zero in diatomic molecules,..."

Page 42 in the caption of table 2.2 comparisons with the most recent data from literature are given in table 3.3.5 page 42

Page 87 replace $D_e^B + T_e^B = \Delta(\dots$ by $D^B = D_e^B + T_e^B = \Delta(\dots$

Page 108 after equation 5.6 the following information is missing: The effect of the operator \hat{L}^2 is included as an effective contribution in the potential curves.

Page 117 the value of the improved representation is about 60 and not 110.

Page 125 the equation 5.36 should be replaced by:

$$\begin{aligned} \chi^3(R) &= [\chi_1(R - R_c) + \chi_2(R - R_c)^2 + \chi_3(R - R_c)^3 + \chi_4(R - R_c)^4] \\ &\quad \times 1 / (1 + e^{\epsilon(R - R_s)}) \\ \epsilon &> 0, \quad R_c \text{ is a fixed parameter, } R_s \text{ is a cutting at large } R \end{aligned}$$

Page 144 in table A.5 replace $T_e^A = 14106.957(9) \text{ cm}^{-1}$ by $T_e^c = 14850.953(9) \text{ cm}^{-1}$

Olivier Allard

Date of birth: 23/10/1972
place of birth: Clichy-la-Garenne, France
Nationality: French
familial situation: single

Education and employment

- 2003 - 2004 Scientific coworker in Institut für Quantenoptik
- 2001 - 2003 Scholarship holder in the European Graduate College at the Institut für Quantenoptik
- 1999 - 2000 One year and half as Master of physical science in the Pierre de Ronsart middle school in Paris.
- 1998 - 1999 D.E.A "Lasers and Matter" of the University Paris VI, Pierre et Marie Curie.
- 1997 - 1998 Master's degree on fundamental Physics at the University Paris VII Denis Diderot (distinction).
- 1996 - 1997 Military Service (town service) at Edouard Vaillant middle school.
- 1995 - 1996 Degree on fundamental physics at the University Paris VII Denis Diderot.
- 1992 - 1995 DEUG A "Science and structure of matter" at the University Paris VII Denis Diderot (distinction).

Acknowledgments

My first words will be for Prof. Dr. E. Tiemann who welcomes me during almost four years in his research group. I sincerely thank him for his constant support, his thought always positive, and especially for having shared with me his scientific erudition.

I would like to thank Dr. A.E. Pashov, for his patience, which has been often put to the test. I am glad we learnt to be friend.

I wish to thank Dr. O. Dulieu, my French supervisor and friend. I thank him for his support, for our fruitful exchanges, and his constructive remarks for my thesis manuscript. I hope he will always keep his humor!

I am grateful towards Dr. H. Knöckel for his help, and his ability to find clever ideas for our unsolved laboratory problems.

I would like to thank Matthias, Kirsten, Christian and Tanja for their help and examples. Sebastian, Vania, and Stephan (Whazupdude), I will remember our discussions and laughs.

Christian, meeting you outside the Institute for sport and parties have always been a pleasure for me. I am sure you will send me next summer a picture of you smiling after you did lead a French 7+.

I would like to thanks Cyril, and Norbert for the evening we shared. I have a special thought for those who are abroad like me, Philippe, Frédéric, and Kai.

Enfin, je veux remercier mes parents, qui m'ont apporté un soutien affectif de chaque jour même en étant au loin. Je vous aime.

